SPIN AND LATTICE DYNAMICS IN THIN FILMS: FROM FEMTOSECONDS TO NANOSECONDS

by

Vladimir Alexandru Stoica

A dissertation submitted in partial fulfillment
of the requirements for the degree of
Doctor of Philosophy
(Applied Physics)
in The University of Michigan
2010

Doctoral Committee:

Professor Roy Clarke, Chair
Professor Bradford G. Orr
Professor Ctirad Uher
Associate Professor Lingjie Jay Guo
Associate Professor David A. Reis, Stanford University

DEDICATION

To my wife, Dana, for being my loving source of inspiration;

To my baby-girl, Ada, for being so beautiful;

To my entire family just for being there

ACKNOWLEDGMENTS

I am grateful for the existence of divine harmony that kept me close to my wife, Dana, to my daughter Ada, to my parents, and to my whole family. Even though many years and days have slowly passed, and I was away from home, stubbornly checking again and again the results in the lab, the unconditional support, which always surrounded me, was the reason for the present work to happen. And, sure, it was a place, the University of Michigan, and the people inside, which became my extended family.

I address my special thanks to *Professor Roy Clarke, Professor David Reis, Professor Roberto Merlin, and Professor Ctirad Uher* for offering all possible technical and spiritual resources for my scientific and professional growth. The incredible confidence and tremendous help to promote the present project shown by my Professor and mentor, Roy Clarke, is going to deeply mark my future understanding of science and scientists.

I am expressing my gratitude to all my colleagues and collaborators for our fruitful discussions and work together: John Nees, Codrin Cionca, Ale Lukaszew, Lynn Endicott, Brandon McNaughton, Chris Schlepuetz, Hailing Cheng, Yu-Miin Sheu, Divine Kumah, Khuram Shahid, Haiping Sun, Ibrahim.Oraiqat, Naji Husseini, Yuwei Li, Peter Diehr, Guoyu Wang, Shambhu Ghimire, Mariano Trigo, Andrea Bianchini, Huarui Sun, Jingjing Li, Ilya Vugmeyster, and Jared Wahlstrand, to only name a few. I'm sure there are many other people that touched my life at University, and I apologize to those that are not included above. I thank to everyone for inspiring conversations about the research results, for helping with lab work, for lending equipment, and all in all, for sharing your enthusiasm and interest for the work that I have performed.

I am grateful to Phillip Kubina and Michael Mei from Menlo Systems, who helped from overseas with discussions, and provided a customized design of the dual-fiber-laser system. To the scientific staff from the Advanced Photon Source at Argonne National Laboratory, Dr. Donald Walko, Dr. Eric Dufresne, Dr. Eric Landahl, Dr. Yuelin Li, Dr. Dohn Arms, and Dr. Bernhard Adams, I wish to thank you all for your great dedication and kind help, covering many days and nights next to the beamline.

This is also an opportunity for me to thank the staff of the Applied Physics Program at the University of Michigan, especially to Cyndi McNabb and Charles Sutton, for their consistent help on an everyday basis.

And last, but not least, I would like to express my special thanks and appreciation for the financial support from the NSF Frontiers in Physics FOCUS Center and the Materials Research Program of the Department of Energy, Basic Energy Sciences Division.

TABLE OF CONTENTS

LIST OF FIGURES

Figure

ABSTRACT

In this dissertation we set out to quantitatively investigate the dynamics of magnetic thin films. Specifically, we studied the spin dynamics in epitaxial metallic ferromagnets and the coupling to other degrees of freedom, such as electron and phonon excitations. Key aspects of the spin dynamics were found to occur across a wide range of temporal scales, from femtoseconds to nanoseconds. Accordingly, new instrumental and experimental tools were developed in order to address the complex behavior of the magnetization under strongly non-equilibrium conditions. A new pump-probe fiber-laser-based magnetometer was built and used to access the time-dependence of the magnetic behavior during spin wave excitation and relaxation. The performance of this instrument offers significant advantages over existing methods, including: an unusually large temporal dynamic range (150 fs-10 ns), high frequency bandwidth (~5 THz), high detection sensitivity that corresponds to a signal to noise ratio of better than 10^7, and fast data acquisition at kilohertz scanning rates. These instrumental capabilities allowed us to perform unprecedented studies of coherent spin waves propagating through epitaxial Fe films. The femtosecond laser pulse induces coherent magnetization dynamics indirectly via thermal excitation, resulting in magnon-electron and magneto-elastic coupling. The spin wave propagation speeds and attenuation lengths were determined during spin wave

propagation and reflection at the film boundaries. Coherent spin waves with frequency less than 24 GHz, propagate at velocities < 1.3 km/s, consistent with their dispersion relation. A not well understood behavior occurs for spin waves with wavevector k~0, which are transmitted super-sonically through films of about one classical skin depth thick (1.5 μm). A major step in this work was to establish all-optical techniques for manipulation and coherent control of the magnetization vector. An optically-induced spin reorientation transition of first-order is observed for the first time, which provides a new route to ultrafast coherent magnetization switching. The switching is found to be a three-step temporal process: a *coherent reorientation* (~ 100 ps) is followed by a *spin precession* in a newly created metastable state (~ 300 ps), which evolves into a *dual domain state* that undergoes relaxation within ~ 2 - 4 ns.

CHAPTER 1

INTRODUCTION

Magnetism is one of the most fundamental properties of condensed matter, known since ancient times. The basic entity in classical magnetism is the magnetic dipole, while in the modern quantum magnetism it is the spin, which represents an intrinsic degree of freedom of the particle constituents [1.1]. In the last two decades, a great deal of attention has been aimed at the study of the fundamentals and applications of the spin of electrons, which is nowadays referred to as Spintronics [1.2-1.6].

One major goal of Spintronics is to exploit the *spin* of the electron, as distinct from its charge properties, in micro- and nano-electronics technology applications. Another important goal is to learn about the physics of the spin in the condensed matter environment. Many experimental techniques can be used to address the measurement and manipulation of the electron spin, and one way for accomplishing this is to use optical methods, which are exploited in this thesis. The innovative aspect of this research is in demonstrating *simultaneous characterization and control of the spin dynamics within the development of an all-optical experimental approach.*

There are two main approaches in the field of Spintronics applications regarding its basis in magnetic materials. The first one is the case of semiconducting magnetic materials that, in principle, are capable of integration with existing electronics technology [1.5]. In practice, this route is difficult to walk since a robust demonstration of room-temperature functionality of these materials is still lacking at the present time. Second, there is the case of metallic magnetic materials, which usually provide the needed functionality at the ambient temperature. On the other hand, the integration of metallic magnetic materials with the mainstream semiconductor electronics seems more difficult and is currently under investigation [1.6]. Nevertheless, hard-drive information storage

technology, has seen a very fast pace of development during the last decades, as has magnetic random access memory [1.6].

While both semiconductor and metallic-based materials for Spintronics continue to be improved, significant advancements are simultaneously being made regarding the capabilities of the experimental techniques for research in this area. One example is the advent of the ultrafast lasers studies of the ferromagnetic materials, which has motivated this dissertation work. For this type of study, it is proper to consider the elemental ferromagnetic transition metals: Fe, Co and Ni. Although these materials were already investigated for several centuries in bulk form, the intricate physics that they exhibit when deposited as a thin film on a substrate is still intensely researched at the present. The case of *epitaxial* thin films, where the magnetic material forms in coherent registry with the underlying substrate, is particularly interesting. This is due to the ability of the epitaxy to strongly influence the magnetic behavior, especially the anisotropy, as well as, their potential for metal-based Spintronics applications [1.7, 1.8].

Ultrafast lasers provide optical pulses with femtosecond time duration at a given repetition rate, which makes them useful for observing the spin dynamics in solids with unprecedented time resolution. Moreover, because the number of photons per unit time in a single optical pulse is very large (10^{21}-10^{28} s^{-1}), these pulses can interact with condensed matter very strongly. In fact, this enhanced interaction generates a new paradigm. The new instrument developed for our research, an optical magnetometer, is not only effective in the characterization of magnetic material properties, but also can modify and manipulates these properties in a significant way either reversibly or irreversibly. Since these methods involve the use of a femtosecond optical pulse, one major importance of this approach is to provide insight about the ultrafast processes in magnetic materials. Moreover, the use of femtosecond optical excitation opens the possibility to resolve important details of the spin dynamics. The relevant topic of interest is to elucidate the spin dynamics interaction with the other degrees of freedom of the magnetic material, including the electron and phonon degrees of freedom.

One early example of ultrafast optical studies of ferromagnetic transition metals was provided, more than a decade ago, in the pioneering work of Beaurepaire and co-

workers [1.9]. In these studies, an ultrafast demagnetization (UD) effect was discovered to occur in Ni on the femtosecond timescale, before the spins reach thermal equilibrium with the phonons. The relevance of this discovery stems from the poor understanding of the spin-dependent relaxation mechanisms in elemental ferromagnetic materials. This situation is vividly illustrated by noting the ongoing controversy, which still surrounds the interpretation of the UD observations [1.10, 1.11].

In other examples, which look at different aspects of the laser-induced excitations in Ni, the intense femtosecond optical irradiation of materials was used for producing transient thermoelastic strains to study the lattice dynamics in thin films [1.12]. It has also been employed in studies of coherent spin dynamics in films and nanostructures [1.13]. A detailed connection between these different experiments is still missing at the present, although some correlations can be made based on the magnetostriction effect, for example. Magnetostriction establishes the relationship between mechanical deformation and the orientation of spins in magnetic materials and was discovered by Joule long ago [1.14]. For the case of an oxide compound ferromagnetic material, the magnetostriction was already seen to be important on the ultrafast timescale, whereas for transition metal ferromagnets its contribution to ultrafast spin dynamics is still an important unresolved problem, one that motivates the current studies. Moreover, a presently outstanding question that still searches for a clear answer is to elucidate the timescales of spin-lattice interaction and relaxation [1.1].

Another experimental approach looks at the ultrafast laser-induced modification of the magnetic anisotropy of Co through studies of the coherent spin precession [1.15]. An interesting question arises regarding the speed of this process. In particular, can this process be pursued optically using the coupling of light to magnetization? The optical modulation of magnetic anisotropy was actually observed in ferrimagnetic materials such as garnets [1.16], but is less clear for the ferromagnetic transition metals. For instance, the optical manipulation of magnetization via the ultrafast change of the magnetic anisotropy is the main topic of several recent publications, which highlighted its importance. In one case, a transient all-electric-field-induced magnetic anisotropy was observed [1.17], followed by arguments that such an effect can induce magnetization reversal. Along with supporting theoretical findings [1.18, 1.19], another experiment

[1.10] pursues the fs separation of a transient polarization and magnetization built up by the laser pulse, which is attributed to the coherent interaction between photons and magnetization. Yet another recent theoretical model proposes the use of an inverse magneto-optical Faraday effect for inducing the magnetic switching [1.20]. All these experiments or theoretical predictions emphasize the role of optical excitation as opposed to the thermal mechanisms in influencing the magnetization dynamics. This fact is motivating the further experimental exploration presented in this thesis.

The Chapters of this thesis are organized as in the following: Chapter 2 provides an examination of the *basic theoretical approaches* necessary to describe the phenomenology of thermal, acoustic, and magnetic excitations induced by ultrafast pulsed lasers, with emphasis on magnetic and magneto-elastic anisotropy of epitaxial ferromagnetic films. Chapter 3 describes *a new method and experimental arrangement*, based on asynchronous optical sampling *(ASOPS),* able to ensure pump-probe optical data acquisition spanning over 5 temporal orders of magnitude (from 100 fs to 10 ns). The capability of this method is illustrated by presenting the results on fast heat transport, acoustic phonon generation and propagation, and magnetization dynamics in epitaxial Fe films. Additional time-resolved X-ray scattering studies of thermal transport in Fe films with variable thickness are also described in Chapter 3. Chapter 4 provides the results of an in-depth study of *coherent spin waves* generated by the ultrafast laser pump. This study aims to address some fundamental questions in optically excited magnetization dynamics in thin films: mechanism of generation, magnetic anisotropy, exchange interaction, spin wave propagation and attenuation. Chapter 5 reports *first experimental evidence of a coherent and reversible first-order spin-reorientation transition* triggered by a laser-induced change of magnetic anisotropy. A model is provided to explain the observed single-domain magnetic precessional switching and to predict further applications of this technique. Chapter 6 summarizes the findings and discusses some ideas for future studies.

REFERENCES FOR CHAPTER 1

1.1 J. Stöhr and H.C. Siegmann, Magnetism: From Fundamentals to Nanoscale Dynamics, Springer Series in Solid-State Physics, Vol. 152. Berlin: Springer, 2006.

1.2 G. A. Prinz, Science 282, 1660 (1998).

1.3 S. A. Wolf, D. D. Awschalom, R. A. Buhrman, J. M. Daughton, S. von Molnár, M. L. Roukes, A. Y. Chtchelkanova, and D. M. Treger, Science 294, 1488 (2001).

1.4 I. Žutic, J. Fabian, and S. D. Sarma, Rev. Mod. Phys. 76, 323 (2004).

1.5 D. Awschalom and M. Flatte, Nature Phys. 3, 153 (2007).

1.6 C. Chappert, A. Fert, and F. N. V. Dau, Nature Mater. 6, 813 (2007).

1.7 S. S. P. Parkin, C. Kaiser, A. Panchula, P. M. Rice, B. Hughes, M. Samant, and S. H. Yang, Nature Mater. 3, 862 (2004).

1.8 S. Yuasa, T. Nagahama, A. Fukushima, Y. Suzuki, and K. Ando, Nature Mater. 3, 868 (2004).

1.9 E. Beaurepaire, J. C. Merle, A. Daunois, and J. Y. Bigot, Phys. Rev. Lett. 76, 4250 (1996).

1.10 J.-Y. Bigot, M. Vomir, and E. Beaurepaire, Nat. Phys. 5, 515 (2009).

1.11 B. Koopmans, G. Malinowski, F. Dalla Longa, D. Steiauf, M. Fähnle, T. Roth, M. Cinchetti, and M. Aeschlimann, Nature Mater. 9, 259 (2010).

1.12 C. Thomsen, H. T. Grahn, H. J. Maris, and J. Tauc, "Surface generation and detection of phonons by picosecond light-pulses", Phys. Rev. B 34, 4129 (1986).

1.13 M. van Kampen, C. Jozsa, J. T. Kohlhepp, P. LeClair, L. Lagae, W. J. M.de Jonge, and B. Koopmans, "All-optical probe of coherent spin waves," Phys. Rev. Lett. 88, 227201 (2002).

1.14 J.P. Joule, Sturgeons Annals of Electricity, 8, 219 (1842).

1.15 M. Vomir, L. H. F. Andrade, L. Guidoni, E. Beaurepaire, and J. Y. Bigot, "Real Space Trajectory of the Ultrafast Magnetization Dynamics in Ferromagnetic Metals," Phys. Rev. Lett. 94, 237601 (2005).

1.16 F. Hansteen, A. Kimel, A. Kirilyuk, and T. Rasing, Phys. Rev. Lett. 95, 047402 (2005).

1.17 S.J. Gamble et al., Phys. Rev. Lett. 102, 217201 (2009).

1.18 G. P. Zhang and W. Hübner, Phys. Rev. Lett. 85, 3025 (2000).

1.19 G. P. Zhang, W. Hübner, G. Lefkidis, Y. Bai, and T. F. George, Nat. Phys. 5, 499 (2009).

1.20 M. I. Kurkin, N. B. Bakulina, and R. V. Pisarev, Phys. Rev. B 78, 134430 (2008).

CHAPTER 2

THEORETICAL BACKGROUND

This chapter is concerned with laying the theoretical basis for laser-driven excitations in metallic thin films that are optically opaque. Particular emphasis is placed on laser excitation of coherent lattice and spin dynamics. Their dynamical interplay in the case of ferromagnetic transition metals is studied using ultrafast-laser pump-probe techniques.

A multitude of laser based (or all-optical) pump-probe techniques have been designed for investigating the interaction process of an intense laser pulse with optically opaque materials, as well as measuring some specific material properties related to ultrafast transient behavior [2.1-2.5]. The material's response to the light excitation has been explained as a chain of coupled phenomena starting with the creation of a non-equilibrium electron distribution due to the initial energetic transfer between photons and electrons [2.6]. In the vast majority of cases, this first step of interaction has been treated as an incoherent process despite the coherent nature of the laser light excitation. Additionally, many non-equilibrium coherent phenomena have been observed after the femtosecond optical excitation [2.7-2.10], but their detailed origin is still uncertain. It follows that a unified approach for understanding laser excitations in optically opaque materials is difficult to establish, and different classes of materials need to be treated separately. In this situation, the modeling of the experiments has to ensure that the relevant theoretical concepts are employed in order to accurately describe the physics of individual materials.

The following sections summarize the main theoretical concepts and mathematical approaches used in the interpretation of the experimental observations included in this thesis. We start with a description of the incoherent excitation, which results in a thermal excitation-relaxation process extended on a nanosecond scale. Coherent phonon generation is the subject of the second section, where the detection mechanism of long-lived acoustic waves is described. The theoretical basics concerning

magnetic anisotropy in thin films and their spin dynamics are summarized in the last two sections.

2.1 Time-Domain Thermo-Reflectance

The photon-electron interaction perturbs the normal thermal equilibrium in the electron distribution. The optically induced intra-band transitions, most common in metals, require that the phonon absorption occurs simultaneously with a collision event (electron-electron or electron-phonon), to ensure the conservation of energy and momentum (Drude model [2.11]). The electrons are driven to excited states of higher energy inside the conduction band, resulting in a non-equilibrium distribution which cannot be described by a single value for the system temperature. There are two mechanisms competing to restore the equilibrium: electron-electron collisions and electron-phonon collisions. The first mechanism is much stronger and results in an internal thermalization to an electron temperature far in excess to the lattice temperature ($T_e > T_0$). Measurements of the wavelength dependence of the transient reflectivity of a thin film of gold deposited on sapphire, performed by Schoenlein *et al*. [2.12], show that the thermal electronic equilibrium is already reached after 200 fs, while a slower cooling follows in pico-seconds. Based on experimental observations and theoretical predictions of Anisimov *et al*. [2.13] the further time evolution of electron and lattice temperatures can be described by the two-temperature, or parabolic two-step (PTS), model [2.14]. Following this model, the electron and lattice temperatures are related by a set of non-linear differential equations:

$$\begin{aligned} C_e(T_e)\frac{\partial T_e}{\partial t} &= \kappa_e \nabla^2 T_e - g(T_e - T_l) + P(\vec{r}, t) \\ C_l \frac{\partial T_l}{\partial t} &= \kappa_l \nabla^2 T_l + g(T_e - T_l) \end{aligned} \tag{2.1}$$

The electronic heat capacity is proportional to the electron temperature: $C_e = \gamma T_e$, whereas the other parameters, i.e., the lattice heat capacity, C_l, the electron-lattice energy exchange coefficient, g, and the thermal conductivities, κ_e and κ_l, can be considered as

constants. The source term, P, accounts for the optical pulse heating. As the electron thermal diffusivity, κ_e/C_e , is much larger than the lattice thermal diffusivity, κ_l/C_l , the diffusion ($\nabla^2 T_l$) term in the second equation can be neglected. For thin enough films (thickness, d, less or equal to the energy deposition length, δ) the diffusion term in the first equation can be also neglected and the electron and lattice temperature can then be considered constant over the whole thickness of the film. In this approximation, the equations (2.1) reduce to:

$$\begin{aligned} \gamma T_e \frac{dT_e}{dt} &= -g\left(T_e - T_l\right) \\ C_l \frac{dT_l}{dt} &= g\left(T_e - T_l\right) \end{aligned} \tag{2.2}$$

with the initial conditions: $T_e(0) = T_{ex}$ and $T_l(0) = T_0$. Combining the two equations from (3.2), a single differential equation for the electron temperature can be deduced (first introduced by Brorson *et al*. [2.15]):

$$T_e \frac{d^2 T_e}{dt^2} + \left[\frac{dT_e}{dt}\right]^2 + \frac{g}{\gamma}\left(1 + \frac{\gamma}{C_l}\right)\frac{dT_e}{dt} = 0 \tag{2.3}$$

A rough approximation of the solution of (2.3) results in an exponential decay

$$T_e(t) - T_l(t) = \left[T_{ex} - T_0\right]\exp\left(-\frac{t}{\tau_{e-ph}}\right);\ \tau_{e-ph} \approx \frac{\gamma T_0}{g} \tag{2.4}$$

This decay corresponds to a constant relaxation rate, meaning a constant relative rate of energy transfer from electrons to lattice. The relaxation rate, g/γ, as has been shown by Allen [2.16] to scale with the electron-lattice coupling constant, λ, and the second moment of the phonon spectrum, $\langle\omega^2\rangle$:

$$\frac{g}{\gamma} = \frac{3\hbar}{\pi k_B} \times \lambda \times \left\langle \omega^2 \right\rangle \tag{2.5}$$

The electron temperature relaxation can be probed by measuring the transient change of the optical reflectivity in the femtosecond to picosecond range. The change of optical reflectivity, measured with a delayed probe laser pulse, correlates to both electron and lattice temperature changes:

$$\Delta R = a\ \Delta T_e + b\ \Delta T_l \tag{2.6}$$

The optical signal relaxation on a fast time scale (< 10 ps) follows the electronic relaxation alone, as the change in lattice temperature is highly diminished due to the heat capacity imbalance ($C_l >> C_e$). The experimental results reported by Brorson et al. [2.15] confirmed the predictions of Allen [2.16] and demonstrated that, for most of the metallic films, the conduction electrons reach thermal equilibrium with the lattice at a time delay below 2 ps. After this process is exhausted, the optical reflectance scales with the thermal transients and the pump-probe method has to be considered a technique of measuring the transient thermo-reflectance (TTR), as named by Paddock and Eesley [2.17], or time-domain thermo-reflectance (TDTR), differentiating these methods from the frequency-domain approach (see Cahill [2.18]).

The heat transfer in thin film structures under a laser excitation is usually considered a one-dimensional diffusion-like problem, because the diameter of the light beam is considerably larger than the thin film thickness. However, the usual solutions of the diffusion equation in a semi-infinite medium cannot be employed directly due to the presence of thin film interfaces, which introduce sharp discontinuities in temperature. The concept of *thermal boundary resistance* (TBR) or *thermal boundary conductance* (TBC) was therefore introduced to describe this feature [2.19], following the approach of Kapitza. In the case of a single thin film on a substrate, the time-dependent heat conduction equations are the following [2.20]:

$$\begin{aligned} C_f \frac{\partial T_f}{\partial t} &= k_f \frac{\partial^2 T_f}{\partial z^2} \\ C_s \frac{\partial T_s}{\partial t} &= k_s \frac{\partial^2 T_s}{\partial z^2} . \end{aligned} \tag{2.7}$$

where T_f and T_s are the temperature in the film and substrate, respectively; C_f and C_s are the corresponding thermal capacitances, and k_f and k_s are the thermal conductivities. The initial conditions are:

$$T_f(0,z) = \frac{F(1\text{-}R)}{C_f \delta} exp\left(-\frac{z}{\delta}\right) \tag{2.8a}$$

$$T_s(0,z) = 0 \tag{2.8b}$$

F is the laser pulse integrated energy, R is the pump pulse reflectance, and δ is the energy deposition depth. Eq. (2.8b) neglects the initial heating in the substrate. This assumption

holds when the film thickness, d, surpasses δ and/or the substrate has a small optical absorption coefficient. The boundary conditions equate the heat flux as proportional to the temperature jump with (TBC), with σ as a coefficient:

$$-k_f \frac{\partial T_f}{\partial z}(t,d) = \sigma\left(T_f - T_s\right); -k_s \frac{\partial T_s}{\partial z}(t,d) = \sigma\left(T_f - T_s\right) \tag{2.9}$$

The influence of TBC will be clearly visible when the heat diffusion in the film exceeds the effects of interface cooling. As the time constant for diffusion across the film is given by $C_f d^2/k_f$ and the interface time constant for a highly conductive substrate is $C_f d/\sigma$, the condition of TBC satisfies: $d\sigma < k_f$. This means that by measuring the film surface cooling curve in the ns range, for a film thickness of 10-100 nm, interfaces having a ~10^8 W/m^2/K TBC can be characterized by TDTR [2.20].

Many authors reported analytical solutions for the heat transport equations based on the Laplace transformation in various approximations [2.21-2.24]. Others use the frequency domain solutions to compute numerically the time domain solutions [2.25-2.26]. Here, we use a numerical approach based on finite difference formulation, similar to those used in [2.17] and [2.20].

2.2 Coherent Acoustic Phonons Exited with Laser Pulses

The picoseconds-range reflectivity oscillations in pump-probe experiments on thin films were first reported by Thomsen et al. [2.27]. These features have been attributed to inhomogeneous lattice strain induced by the pump pulse and this intuitive explanation has been later confirmed by direct ultra-fast time-resolved X-ray diffraction [2.28]. This approach assumes that a strain pulse, considered as a coherent acoustic phonon (CAP) pulse, is generated at the sample surface during the laser pulse absorption. As was described in the previous section, the energy is transferred through a succession of incoherent processes: photon-electron scattering followed by electron-lattice relaxation. Thomsen et al. considered the stress induced by a sudden increase of lattice temperature only:

$$\sigma_{33}(z,t) = C_{33}\varepsilon_{33}(z,t) - 3B\beta\,\Delta T(z,t) \tag{2.10}$$

In this equation the spatial temperature dependence was reduced to one dimension, z, perpendicular to the film surface, as in the previous section. The *"33"* tensor index stands for z-axis (or 3rd axis) components. In Eq. (2.10), σ and ε, are the stress and strain tensors, reduced to one component in our case; $C_{33} = 3B(1-\nu)/(1+\nu)$ is the elastic modulus in the z direction, B is the bulk modulus, ν is the Poisson ratio, and β represents the linear expansion coefficient. The equations of elasticity in one dimension can be represented as:

$$\rho \frac{\partial^2 u_z}{\partial t^2} = \frac{\partial \sigma_{33}}{\partial z}$$
$$\varepsilon_{33} = \frac{\partial u_z}{\partial z} \tag{2.11}$$

or, in a reduced form, as a wave equation:

$$\frac{\partial^2 \varepsilon_{33}}{\partial t^2} - V_S{}^2 \frac{\partial^2 \varepsilon_{33}}{\partial z^2} = \frac{1}{\rho} \frac{\partial \sigma_{33}^{th}}{\partial z}$$
$$\sigma_{33}^{th} = -\gamma C \, \Delta T(z,t) \tag{2.12}$$

The initial condition requires zero strain for all z values, whereas the surface strain behavior follows from the condition that the stress must be zero at the surface ($z = 0$) at all times:

$$\varepsilon_{33}(z,0) = 0$$
$$\varepsilon_{33}(0,t) = \frac{\gamma C}{\rho V_S{}^2} \Delta T(0,t) \tag{2.13}$$

The following notations are used: u_z is the displacement in the z-direction, ρ is the density, $V_S = (C_{33}/\rho)^{1/2}$ is the speed of sound, C is the specific heat and $\gamma = 3B\beta/C$ is the Grüneisen parameter [2.29]. It is clear that CAP are generated due to the high time and space localization of the thermal shock; therefore the Thomsen et al. [2.27] approach will work well for semi-infinite media for relatively thick films (d>δ). In the semi-infinite case, the heat diffusion with a thermal diffusivity, D, defined as a ratio between the thermal conductivity, k, and the heat capacity, C, enforces a time-dependence of the temperature represented by the equation:

$$\Delta T(z,t) = \frac{1}{\sqrt{4\pi D t}} \int_0^\infty \left[\exp\left[-\frac{(z-z')^2}{4Dt} \right] + \exp\left[-\frac{(z+z')^2}{4Dt} \right] \right] \Delta T(z',0) \, dz' \tag{2.14}$$

The spatial distribution of the initial temperature corresponds to (2.8) with an energy deposition depth, δ, if we neglect the laser pulse time dependence. This approximation is justified when the light pulse duration, τ_0, does not exceed the time needed for the strain pulse to leave the excitation zone: $\tau_0 << \delta/V_S \sim 2$ ps. The equation (2.12) can be integrated as follows [2.29]:

$$\varepsilon_{33}(z,t) = -\frac{\gamma C}{2\rho V_S{}^2} \int_{-\infty}^{\infty} \mathrm{sgn}\left[z - V_S(t-t')\right] \left.\frac{\partial T}{\partial t}\right|_{(|z-V_S(t-t')|,t')} dt' \tag{2.15}$$

with the point t′ = 0 excluded from the integral. This bipolar pulse, propagating in the forward direction, has a shape which is entirely determined by the dimensionless parameter: $D/V_S\delta$. The acoustic attenuation was not taken into account. As it is frequency dependent, this attenuation can distort the acoustic pulse shape during its propagation. Neglecting the thermal diffusion effect, equation (2.15) reduces to a simple analytic form:

$$\varepsilon_{33}(z,t) = -\frac{\gamma C}{2\rho V_S{}^2} \mathrm{sgn}\left[z - V_S t\right] \exp\left[-\frac{|z - V_S t|}{\delta_{pump}}\right] \tag{2.16}$$

For an absorbing film grown on a transparent substrate, the CAP generated inside the film, close to its surface, will be reflected by the film-substrate interface with a reflection coefficient related to the mismatch of their corresponding acoustic impedances Z_f and Z_s [2.30]:

$$r_{fs} = \frac{Z_s - Z_f}{Z_s + Z_f} \tag{2.17}$$

Note that the acoustic impedance is equal to the product of density and sound velocity. In a reflecting geometry, at the film surface, a sequence of echoes could be observed, with a delay period of:

$$T_{CAP} = \frac{2d}{V_S} \tag{2.18}$$

Such echoes have been observed in metallic films, with a film thickness ranging from 100 to 500 nm), as in Au and Ag [2.29], Ni and Cr [2.27, 2.31], or Al [2.32].

The propagation of CAP into the material induces a spatiotemporal change of the dielectric function, $\chi = (n+\mathrm{i}\kappa)^2$, where n and κ are the real and imaginary part of the index

of refraction for the probe light. Note that the absorption length is related to the imaginary part of the index of refraction by relation: $\delta_{probe} = \lambda/(4\pi\kappa)$. The local change of χ caused by strain can be approximated by:

$$\Delta\chi(z,t) = 2\,(n+i\kappa)\left(\frac{dn}{d\varepsilon_{33}} + i\frac{d\kappa}{d\varepsilon_{33}}\right)\varepsilon_{33}(z,t) \tag{2.19}$$

Considering the interference of all infinitesimal waves reflected by strain induced fluctuations in the dielectric constant, and including the wave reflected at the surface, the following reflection coefficient is obtained:

$$r = r_0 + i\frac{k_0^2}{2k}t_0\tilde{t}_0\int_0^\infty \exp[2ikz']\,\Delta\varepsilon(z',t)\,dz' \tag{2.20}$$

where k_0 and k are the wave vectors in vacuum and in the medium, respectively; r_0 is the surface reflection coefficient; t_0 and $\tilde{t}_0$ are the transmission coefficients through the surface discontinuity crossing from vacuum into the film and vice versa, respectively. All these constants are defined by the following relations:

$$k = k_0\,(n+i\kappa);\; r_0 = \frac{k_0-k}{k_0+k};\; t_0 = \frac{2k_0}{k_0+k};\; \tilde{t}_0 = \frac{2k}{k_0+k}. \tag{2.20a}$$

Combining the equations (2.19) and (2.20) the change in reflectivity can be expressed as a spatial average of the strain weighted with a sensitivity function, $f(z)$, first defined by Thomsen et al. [2.27]:

$$\Delta R(t) = |r|^2 - |r_0|^2 = \int_0^\infty f(z)\,\varepsilon_{33}(z,t)\,dz \tag{2.21}$$

where:

$$f(z) = f_0\sqrt{\left(\frac{dn}{d\varepsilon_{33}}\right)^2 + \left(\frac{d\kappa}{d\varepsilon_{33}}\right)^2}\,\sin\left(\frac{4\pi nz}{\lambda} - \phi\right)\exp\left(-\frac{z}{\delta_{probe}}\right);$$

$$f_0 = 8k_0\,\frac{\sqrt{n^2\left(n^2+\kappa^2-1\right)^2 + \kappa^2\left(n^2+\kappa^2+1\right)^2}}{\left[(n+1)^2+\kappa^2\right]^2}; \tag{2.21a}$$

$$\phi = \tan^{-1}\left(\frac{\kappa\left(n^2+\kappa^2+1\right)}{n\left(n^2+\kappa^2-1\right)}\right) + \tan^{-1}\left(\frac{dn/d\varepsilon_{33}}{d\kappa/d\varepsilon_{33}}\right).$$

If $\delta_{probe} >> \delta_{pump}$, which corresponds to the use of different pump and probe wavelengths (in Section 3.3 we underline this feature as a significant advantage as provided by our innovative dual wavelength pump-probe approach), we adopt the approximation (2.16) where the relative change in reflectivity becomes a simple sinusoidal function (see [2.33]):

$$\frac{\Delta R}{R} \sim \sin\left(\frac{4\pi n V_S t}{\lambda} - \phi\right) \exp\left(-\frac{V_S t}{\delta_{probe}}\right) \tag{2.22}$$

This means that the frequency of this signal should be proportional, and the damping time inversely proportional, to the speed of sound, $f_{CAP} = 2nV_S/\lambda$ and $\tau_{probe} = \delta_{probe}/V_S$, respectively. The phase, ϕ, should be constant; however, the steady decrease of the surface temperature can induce a slow variation of phase equivalent to a frequency chirp. The CAP propagation equations, as (2.15) or (2.16), neglect the real damping. It can be taken into account by an additional exponential decay in equation (2.22).

When δ_{probe} is small, the CAP signal will quickly disappear after a period of τ_{probe}. However, in layered structures, the CAP reflected by interfaces will be detected as soon as they come close to the surface. In this case, the reflectivity oscillation frequency is derived from equation (2.18) and the signal shape is not purely sinusoidal. The optical probe reflectivity retains salient features corresponding to the original stress pulse, as well as to the frequency-dependent sound attenuation [2.27]. Beside thermal stresses the generation of CAP includes the contribution of hot electrons, which can be accounted for by using the two-temperature model [2.29, 2.31], or a non-thermal relaxation model [2.32]. The electronic contribution resides not only in changing the shape of the reflectivity signal, but also in generating a new sequence of echoes due to the fast electron diffusion. This generates a secondary CAP at the interface between the film and substrate, if the film thickness $d_f < \frac{\pi \kappa_e}{C_e V_s} \sim 100$ nm [2.32].

Reducing the film thickness to 20 nm or less results in promoting a homogeneous electronic and lattice heating by the laser pump pulse, which excites the fundamental resonant acoustic (breathing) mode, similar to those excited in metallic nanoparticles [2.34]. The homogeneity of CAP was proved by femtosecond electron diffraction [2.35].

Both all-optical and diffraction observations can be described by a damped harmonic oscillator equation [2.34, 2.36]:

$$\frac{d^2Q}{dt^2} + \frac{2}{\tau_0}\frac{dQ}{dt} + \omega_0{}^2 Q = S(t) \tag{2.23}$$

The following notations are used: Q – the displacement of the CAP; τ_0 – the effective damping time; $\omega_0 = \pi V_S/d_f$ – the breathing mode angular frequency; S(t) – the source term accounting for thermal expansion induced stress and the hot electron enforced pressure. The source term reveals two time-scale features, a smeared Heavyside step-function, h(t), with a characteristic time determined by the pump pulse breath (< 100 fs), followed by a slower increase toward saturation with a characteristic time of about 1 ps:

$$S(t) \sim \gamma_e h(t) + (\gamma_l - \gamma_e)\left[1 - \exp\left(-\frac{t}{\tau_{e-ph}}\right)\right] \tag{2.24}$$

This numerical approach was successfully applied to explain CAP features such as the initial phase and damping [2.34, 2.36], or to study material properties such as the film elastic stiffness [2.37].

2.3 Magnetic Anisotropy in Thin Films

Now we consider the case where the film has magnetic character. The present study will pay special attention to ferromagnetic epitaxial films, i.e., the thin epitaxial layer has a well defined crystallographic relationship with the supporting substrate. The aim of this section is to describe the magnetic interactions in epitaxial films, their angular dependence both in-plane and out-of-plane, which are necessary to derive the magnetization dynamics. The main sources used in the following are: Farle's review on ferromagnetic resonance [2.38] and Sander's review on magnetic anisotropy [2.39].

The magnetic free energy, F_m, in a single domain thin ferromagnetic film can be expressed as a sum of several contributions:

$$F_m = F_c + F_d + F_z + F_{me} + F_u \tag{2.25}$$

where F_c is the magneto-crystalline energy, F_d is the demagnetization field contribution, F_z is a Zeeman energy corresponding to the interaction of the magnetization with an

external magnetic field, F_{me} represents the contribution due to the magneto-elastic effect, and F_u is a phenomenological uniaxial thin film contribution.

1. *F_c – magneto-crystalline energy*, takes into account the anisotropy of the lattice. For cubic lattices, F_c can be expressed as a function of the direction cosines α_1, α_2, α_3 of the magnetization vector $\vec{M}$ relative to the cubic axes through a polynomial series expansion. The polynomial expansion includes the cubic symmetry by using two cubic invariants:

$$\begin{aligned} s &= \alpha_1^2\alpha_2^2 + \alpha_2^2\alpha_3^2 + \alpha_3^2\alpha_1^2 \\ p &= \alpha_1^2\alpha_2^2\alpha_3^2 \end{aligned} \tag{2.26a}$$

as follows:

$$F_c = K_0 + K_1 s + K_2 p + K_3 s^2 + K_4 sp + \ldots \tag{2.26b}$$

Only the first two terms are usually considered. As the directional cosines α_1, α_2, α_3 are defined in the crystal reference system, in the sample (thin layer) coordinates, the magneto-crystalline energy takes different forms depending of the thin-layer orientation:

Case (a)

$$\begin{aligned} &x \equiv \langle 100 \rangle, \quad y \equiv \langle 010 \rangle, \quad z \equiv \langle 001 \rangle \\ &\alpha_1 = \sin\theta\cos\theta, \quad \alpha_2 = \sin\theta\sin\phi, \quad \alpha_3 = \cos\theta \\ &F_c = K_0 + \frac{K_1}{4}\left(\sin^4\theta\sin^2 2\phi + \sin^2 2\theta\right) + \frac{K_2}{16}\sin^2\theta\sin^2 2\theta\sin^2 2\phi \end{aligned} \tag{2.27}$$

Case (b)

$$\begin{aligned} &x \equiv \langle 001 \rangle, \quad y \equiv \langle 0\bar{1}1 \rangle, \quad z \equiv \langle 011 \rangle \\ &\alpha_1 = \frac{1}{\sqrt{2}}\left(\cos\theta + \sin\theta\sin\phi\right), \quad \alpha_2 = \frac{1}{\sqrt{2}}\left(\cos\theta - \sin\theta\sin\phi\right), \quad \alpha_3 = \sin\theta\cos\phi \\ &F_c = K_0 + \frac{K_1}{4}\left[\cos^4\theta + \sin^4\theta\sin^2\phi\left(4 - 3\sin_2\phi\right) + \sin^2 2\theta\left(1 - \frac{3}{2}\sin^2\phi\right)\right] \end{aligned} \tag{2.28}$$

Thus, the in-plane anisotropy for the (100) plane of the single-crystal layer will be reduced to:

$$F_c^{100}\left(\theta=\frac{\pi}{2}\right)=K_0+\frac{K_1}{4}\sin^2 2\phi \tag{2.29}$$

with easy axes at 0^0, 90^0, 180^0, and 270^0 (four fold symmetry). For the (110) plane, the in-plane anisotropy becomes:

$$F_c^{110}\left(\theta=\frac{\pi}{2}\right)=K_0+\frac{K_1}{4}\sin^2\phi\left(4-3\sin^2\phi\right)=F_c^{100}\left(\theta=\frac{\pi}{2}\right)+\frac{K_1}{4}\sin^4\phi \tag{2.30}$$

The additional uniaxial term moves the in-plane hard axis from 45^0 in the <001> case to 90^0.

2. F_d – *demagnetization field contribution* of shape-anisotropy energy:

$$F_d=2\pi M_{eff}M_0\cos^2\theta \tag{2.31}$$

This term expresses the tendency of the magnetization to stay in plane for thin ferromagnetic layers.

3. F_z – *Zeeman energy* corresponding to the interaction of the magnetization with external magnetic field. The general expression for F_z is:

$$F_z=-HM_0\left[\sin\theta\sin\theta_H\cos\left(\phi-\phi_H\right)+\cos\theta\cos\theta_H\right] \tag{2.32}$$

where θ_H and Φ_H are the spherical coordinates of the external field. When the field is applied in plane, this equation becomes:

$$F_z=-HM_0\sin\theta\cos\left(\phi-\phi_H\right) \tag{2.33}$$

4. F_{me} – *magneto-elastic component* results from the coupling of magnetism with the lattice deformation, which can change the exchange energy and the spin-orbit coupling. The phenomenological model for F_{me} defines the magneto-elastic coefficients and we have the following equation for energy:

$$\begin{aligned}E_{me}=\;& B_1\left(\alpha_1^2e_{11}+\alpha_2^2e_{22}+\alpha_3^2e_{33}\right)+\\ &+2B_2\left(\alpha_1\alpha_2e_{12}+\alpha_2\alpha_3e_{23}+\alpha_3\alpha_1e_{31}\right)+\\ &+\;C_1\left(\alpha_1^4e_{11}+\alpha_2^4e_{22}+\alpha_3^4e_{33}\right)+\\ &+\;C_2\left(\alpha_2^2\alpha_3^2e_{11}+\alpha_3^2\alpha_1^2e_{22}+\alpha_1^2\alpha_2^2e_{33}\right)+\\ &+2C_3\left(\alpha_3^2\alpha_1\alpha_2e_{12}+\alpha_1^2\alpha_2\alpha_3e_{23}+\alpha_2^2\alpha_3\alpha_1e_{31}\right)\end{aligned} \tag{2.34}$$

where e_{ij} are the components of the strain tensor. The elastic-strain tensor results from minimization of the elastic energy:

$$F_{el} = \frac{1}{2} C_{11} \left(e_{11}^2 + e_{22}^2 + e_{33}^2 \right) + 2C_{44} \left(e_{12}^2 + e_{23}^2 + e_{31}^2 \right) + \\ + C_{12} \left(e_{11} e_{22} + e_{22} e_{33} + e_{33} e_{11} \right) \tag{2.35}$$

where C_{ij} are the elastic stiffness coefficients for a cubic lattice.

Due to the existence of coupling coefficients, in a magnetic material the strained state of the crystal depends on the magnetic interaction. Consequently, the elastic and magnetic energy have to be solved simultaneously. In practice, the influence of the magnetism on elasticity can be usually neglected, but the reverse influence is significant.

The thermal deformation of a single-crystal layer can be approximated by considering that the in-plane interplanar distances are not modified in the process, and the normal component of the stress is always zero. This means that both components of the in-plane strain correspond to the thermal expansion value with reverse sign:

$$\varepsilon_x = \varepsilon_y = -\varepsilon_T = -\alpha_T \Delta T \tag{2.36}$$

The second condition requires that the first derivative of F_{el} relative to ε_z vanishes:

$$\frac{\partial F_{el}}{\partial \varepsilon_z} = 0 \tag{2.37}$$

a. For the (100) plane parallel with the sample surface:

$$\begin{aligned} &e_{11} = e_{22} = \varepsilon_x = \varepsilon_y = -\varepsilon_T \\ &e_{33} = \varepsilon_2 \\ &e_{12} = e_{23} = e_{31} = 0 \end{aligned} \tag{2.38}$$

Therefore,

$$F_{el}^{(100)} = \left(C_{11} + C_{12} \right) \varepsilon_T^2 + \frac{1}{2} C_{11} \varepsilon_2^2 - 2C_{12} \varepsilon_T \varepsilon_2 \tag{2.39}$$

The condition $\frac{\partial F_{el}}{\partial \varepsilon_z} = 0$ results in:

$$\varepsilon_z = \frac{2C_{12}}{C_{11}} \varepsilon_T = \mathrm{K}^{(100)} \varepsilon_T \tag{2.40}$$

Retaining only two terms for F_{em}, it can be deduced that:

$$F_{em}^{(100)} = B_1 \varepsilon_T \left[\left(1 + \mathrm{K}^{(100)}\right) \cos^2 \theta - 1 \right] \tag{2.41}$$

b. For the (110) plane parallel with the sample surface:

$$\begin{aligned} e_{11} &= e_{22} = \frac{1}{2}\left(\varepsilon_x + \varepsilon_z\right) \\ e_{33} &= \varepsilon_y = \varepsilon_x = -\varepsilon_T \\ e_{12} &= \frac{1}{2}\left(\varepsilon_z - \varepsilon_x\right) \\ e_{23} &= e_{31} = 0 \end{aligned} \tag{2.42}$$

and

$$\begin{aligned} F_{el}^{(110)} = \frac{1}{4}\left(3C_{11} + 5C_{12} + 2C_{44}\right)\varepsilon_T^2 - \frac{1}{2}\left(C_{11} + 3C_{12} - 2C_{44}\right)\varepsilon_T \varepsilon_z + \\ + \frac{1}{4}\left(C_{11} + C_{12} + 2C_{44}\right)\varepsilon_Z^2 \end{aligned} \tag{2.43}$$

From $\frac{\partial F_{el}}{\partial \varepsilon_z} = 0$ we get:

$$\varepsilon_z = \frac{C_{11} + 3C_{12} - 2C_{44}}{C_{11} + C_{12} + 2C_{44}} \varepsilon_T = \mathrm{K}^{(110)} \varepsilon_T \tag{2.44}$$

In spherical coordinates, the magneto-elastic energy for (110)-type layers will be:

$$\begin{aligned} F_{em}^{(110)} = B_1 \varepsilon_T \left[\frac{\mathrm{K}^{(110)} - 1}{2}\left(\sin^2\theta \sin^2\phi + \cos^2\theta\right) - \sin^2\theta \cos^2\phi \right] - \\ - B_2 \varepsilon_T \frac{\mathrm{K}^{(110)} + 1}{2}\left(\sin^2\theta \sin^2\phi - \cos^2\theta\right) \end{aligned} \tag{2.45}$$

5. <u>F_u – *additional in-plane uniaxial contribution*</u> introduced to explain the experimental results in magnetic films (resulting from steps and other surface inhomogeneities):

$$F_u = K_u \sin\theta \cos^2\phi \tag{2.46}$$

2.4 Laser-Induced Spin Dynamics

By analogy with the spin equation of motion, the magnetization equation of motion in the macrospin approximation reads (Landau-Lifshitz equation):

$$\frac{d\vec{M}}{dt} = -\frac{\gamma_0}{1+\alpha^2}\vec{M}\times\vec{H}_{eff} - \frac{\gamma_0\alpha}{M_s\left(1+\alpha^2\right)}\vec{M}\times\left(\vec{M}\times H_{eff}\right) \tag{2.47}$$

A damping term was added with the macroscopic damping parameter, α. The effective magnetic field, $\vec{H}_{eff}$, is determined by the magnetic energy, F_m. Using spherical coordinates, θ and ϕ, the magnetization vector, $\vec{M}$, and the effective field vector, $\vec{H}_{eff}$, are defined as:

$$\vec{M} = M_S\vec{e}_r \tag{2.48a}$$

$$\vec{\boldsymbol{H}}_{eff} = -\frac{1}{M_s}\left(\frac{\partial F_m}{\partial r}\vec{\boldsymbol{e}}_r + \frac{\partial F_m}{\partial\theta}\vec{\boldsymbol{e}}_\theta + \frac{1}{sin\theta}\frac{\partial F_m}{\partial\phi}\vec{\boldsymbol{e}}_\phi\right) \tag{2.48b}$$

The following equations result:

$$\vec{M}\times\vec{H}_{eff} = \begin{vmatrix} \vec{e}_r & \vec{e}_\theta & \vec{e}_\phi \\ M_s & 0 & 0 \\ -\frac{1}{M_s}\frac{\partial F_m}{\partial r} & -\frac{1}{M_s}\frac{\partial F_m}{\partial\theta} & -\frac{1}{M_s\sin\theta}\frac{\partial F_m}{\partial\phi} \end{vmatrix} = \frac{1}{\sin\theta}\frac{\partial F_m}{\partial\phi}\vec{e}_\theta - \frac{\partial F_m}{\partial\theta}\vec{e}_\phi \tag{2.49a}$$

$$\vec{M}\times\left(\vec{M}\times\vec{H}_{eff}\right) = \begin{vmatrix} \vec{e}_r & \vec{e}_\theta & \vec{e}_\phi \\ M_s & 0 & 0 \\ 0 & \frac{1}{\sin\theta}\frac{\partial F_m}{\partial\phi} & -\frac{\partial F_m}{\partial\theta} \end{vmatrix} = M_s\frac{\partial F_m}{\partial\theta}\vec{e}_\theta + \frac{M_s}{\sin\theta}\frac{\partial F_m}{\partial\phi}\vec{e}_\phi \tag{2.49b}$$

$$\frac{d\vec{M}}{dt} = M_s\frac{d\theta}{dt}\vec{e}_\theta + M_s\sin\theta\frac{d\phi}{dt}\vec{e}_\phi \tag{2.49c}$$

Thus, the Landau-Lifshitz equations in spherical coordinates can be expressed as:

$$\frac{d\theta}{dt} = -\frac{\gamma_0}{\left(1+\alpha^2\right)M_s\sin\theta}\frac{\partial F_m}{\partial\phi} - \frac{\gamma_0\alpha}{\left(1+\alpha^2\right)M_s}\frac{\partial F_m}{\partial\theta} \tag{2.50a}$$

$$\frac{d\phi}{dt} = \frac{\gamma_0}{\left(1+\alpha^2\right)M_s\sin\theta}\frac{\partial F_m}{\partial\theta} - \frac{\gamma_0\alpha}{\left(1+\alpha^2\right)M_s\sin^2\theta}\frac{\partial F_m}{\partial\phi} \tag{2.50b}$$

The two derivatives of the magnetic energy depend on the crystallographic orientation of the layer:

a. For the (100) plane, the two components of the H_{eff} are given by:

$$\frac{\partial F_m}{\partial \theta} = -HM_0\left[\cos\theta\sin\theta_H\cos\left(\phi-\phi_\mu\right)-\sin\theta\cos\theta_H\right]+K_u\cos\theta\cos^2\phi- \\ -\left[2\pi M_{eff}M_0-\frac{K_1}{2}\sin^2\theta\sin^2 2\phi-K_1\cos 2\theta+B_1\left(1+\mathrm{K}^{(100)}\right)\varepsilon_T\right]\sin 2\theta \tag{2.51}$$

and

$$\frac{\partial F_m}{\partial \phi} = HM_0\sin\theta\sin\theta_H\sin\left(\phi-\phi_H\right)+\left(K_1\sin^4\theta\cos 2\phi-K_u\sin\theta\right)\sin 2\phi \tag{2.52}$$

b. For the (110) plane, the two components of the H_{eff} are given by:

$$\frac{\partial F_m}{\partial \theta} = -HM_0\left[\cos\theta\sin\theta_H\cos\left(\phi-\phi_\mu\right)-\sin\theta\cos\theta_H\right]+K_u\cos\theta\cos^2\phi- \\ -\begin{bmatrix}2\pi M_{eff}M_0-K_1\left(1-\frac{1}{2}\cos^2\theta\left(1+3\sin^2\phi\right)\right)- \\ -\left(B_1-B_2\right)\frac{1+\mathrm{K}^{(110)}}{2}\varepsilon_T\cos^2\phi-B_2\left(1+\mathrm{K}^{(110)}\right)\varepsilon_T\end{bmatrix}\sin 2\theta \tag{2.53}$$

and

$$\frac{\partial F_m}{\partial \phi} = HM_0\sin\theta\sin\theta_H\sin\left(\phi-\phi_H\right)+ \\ +\begin{bmatrix}K_1\sin^4\theta\left(1-\frac{3}{2}\sin^2\phi\right)-\frac{3}{8}K_1\sin^2 2\theta \\ -K_u\sin\theta+\left(B_1-B_2\right)\frac{1+\mathrm{K}^{(110)}}{2}\varepsilon_T\sin^2\theta\end{bmatrix}\sin 2\phi \tag{2.54}$$

Equilibrium is reached when both derivatives are canceled. Then, the magnetization direction coincides with the $\vec{H}_{eff}$ direction. As the shape-anisotropy energy is much higher than other contributions, and when the external field is in-plane ($\theta_H \approx \pi/2$), then $\theta \approx \pi/2$. In this approximation, the in-plane equilibrium position of the magnetization is given for the two orientations as follows:

a. for the (100) plane:

$$HM_0\sin\left(\phi-\phi_H\right)+\left(K_1\cos 2\phi-K_u\right)\sin 2\phi = 0 \tag{2.55}$$

b. for the (110) plane:

$$HM_0 \sin\left(\phi - \phi_H\right) + \left[K_1 \left(1 - \frac{3}{2} \sin^2 \phi \right) - K_u + \left(B_1 - B_2 \right) \frac{1 + \mathrm{K}^{(110)}}{2} \varepsilon_T \right] \sin 2\phi = 0 \tag{2.56}$$

If the magnetization precession involves only small variations around the equilibrium position, the magnetization energy can be approximated as parabolic around the energy minimum:

$$F_m = F_0 + \frac{1}{2} \left(\theta^2 \frac{\partial^2 F_m}{\partial \theta^2} + 2\theta\phi \frac{\partial^2 F_m}{\partial \theta \partial \phi} + \phi^2 \frac{\partial^2 F_m}{\partial \phi^2} \right) \tag{2.57}$$

The precession frequency will be described by:

$$\omega = \frac{\gamma_0}{M_s \sin\theta} \sqrt{ \left. \frac{\partial^2 F_m}{\partial \theta^2} \right|_{\theta=\frac{\pi}{2}} \left. \frac{\partial^2 F_m}{\partial \phi^2} \right|_{\theta=\frac{\pi}{2}} - \left(\left. \frac{\partial^2 F_m}{\partial \theta \partial \phi} \right|_{\theta=\frac{\pi}{2}} \right) } \tag{2.58}$$

a. for the (100) plane:

$$\left. \frac{\partial^2 F_m}{\partial \theta^2} \right|_{\theta=\frac{\pi}{2}} = 4\pi M_{eff} M_0 + K_1 \left(1 + \cos^2 2\phi \right) + 2B_1 \left(1 + \mathrm{K}^{(100)} \right) \varepsilon_T + \\ + HM_0 \cos\left(\phi - \phi_H\right) - K_u \cos^2 \phi \tag{2.59a}$$

$$\left. \frac{\partial^2 F_m}{\partial \phi^2} \right|_{\theta=\frac{\pi}{2}} = 2K_1 \cos 4\phi - 2K_u \cos 2\phi + HM_0 \cos\left(\phi - \phi_H\right) \tag{2.59b}$$

$$\left. \frac{\partial^2 F_m}{\partial \theta \partial \phi} \right|_{\theta=\frac{\pi}{2}} = 0 \tag{2.59c}$$

b. for (110), the expressions will be:

$$\left. \frac{\partial^2 F_m}{\partial \theta^2} \right|_{\theta=\frac{\pi}{2}} = 4\pi M_{eff} M_0 + K_1 \left(2 - 7\sin^2 \phi + 3\sin^4 \phi \right) - B_2 \left(1 + \mathrm{K}^{(110)} \right) \varepsilon_T + \\ + HM_0 \cos\left(\phi - \phi_H\right) - \left[K_u + \left(B_1 - B_2 \right) \left(1 + \mathrm{K}^{(110)} \right) \varepsilon_T \right] \cos^2 \phi \tag{2.60a}$$

$$\left. \frac{\partial^2 F_m}{\partial \phi^2} \right|_{\theta=\frac{\pi}{2}} = K_1 \left(2 - 13\sin^2 \phi + 12\sin^4 \phi \right) \\ - \left[2K_u - \left(B_1 - B_2 \right) \left(1 + \mathrm{K}^{(110)} \right) \varepsilon_T \right] \cos 2\phi \\ + HM_0 \cos\left(\phi - \phi_H\right) \tag{2.60b}$$

$$\left.\frac{\partial^2 F_m}{\partial\theta\,\partial\phi}\right|_{\theta=\frac{\pi}{2}} = 0 \tag{2.60c}$$

In this way we can describe the equilibrium position of the magnetization vector and its precession dynamics in the experimentally important crystallographic cases relevant to (100) and (110) epitaxial films of magnetic transition metals. The Eq. (2.58) can be expressed in simple manner:

$$\omega_0 = \gamma_0\sqrt{H_1 \times H_2} \tag{2.61}$$

The two characteristic magnetic fields $\boldsymbol{H}_1$ and $\boldsymbol{H}_2$ can be decomposed as follows:

$$\begin{aligned}\boldsymbol{H}_1 &= 4\pi\boldsymbol{M}_{\boldsymbol{eff}} + \boldsymbol{H} + \boldsymbol{H}_{1\boldsymbol{a}}\\ \boldsymbol{H}_2 &= \boldsymbol{H} + \boldsymbol{H}_{2\boldsymbol{a}}\end{aligned} \tag{2.62}$$

with $\boldsymbol{H}$ as the external applied field, and $\boldsymbol{H}_{1a}$ and $\boldsymbol{H}_{2a}$ the contributions of the magnetic anisotropy. All components can be identified using equations (2.59 a, b) or (2.60 a, b). In practice, it is considered that $H_1 \sim 4\pi M_{\text{eff}}$ since the other two contributions are usually orders of magnitude smaller. It is interesting to examine the difference between easy-axis and hard-axis for the two film orientations. Let's consider the applied magnetic field along one of these two directions of symmetry. Relations (2.55) or (2.56) results in the equilibrium magnetization lying along the applied field direction (neglecting the uniaxial K_u contribution as compared to the four fold K_1 contribution in the (100) case). For a (100) film orientation, the easy axis is assigned to the <010> or <001> direction and the contribution of the anisotropy reduces to:

$$M_0\, H_{1a}^{(100)easy} = 2K_1 \tag{2.63a}$$

The field at hard axis, assigned to the <011> direction, imposes a reverse anisotropy contribution:

$$M_0\, H_{1a}^{(100)hard} = -2K_1 \tag{2.63b}$$

A different effect is observed in (110) films. The symmetry is uniaxial with easy axis at <001> and hard axis at <-110>. The corresponding anisotropy contributions are:

$$M_0\, H_{1a}^{(110)easy} = \frac{3}{2}K_1 + \left[\frac{1}{2}K_1 + \left(B_1 - B_2\right)\left(1+\kappa^{(110)}\right)\varepsilon_T - 2K_u\right] \tag{2.64a}$$

$$M_0\, H_{1a}^{(110)hard} = \frac{3}{2}K_1 - \left[\frac{1}{2}K_1 + \left(B_1 - B_2\right)\left(1+\kappa^{(110)}\right)\varepsilon_T - 2K_u\right] \tag{2.64b}$$

To summarize, the magneto-crystalline anisotropy is expected to influence the precession frequency for (100) films, whereas the contribution of thermal stresses, or other uniaxial influences specific to thin-films, will become more prominent in (110)-oriented films.

The precession frequency defined by Eq. (2.58) refers to the homogeneous magnetization mode (the Kittel mode). It implies that the ensemble of spins behaves as a single macrospin. Besides the Kittel mode, the laser-induced dynamic excitation of spins includes spin-wave modes with non-zero propagation wavevectors. In this case, the precession of individual spins is not the same at different sample locations. To take into account the magnetization inhomogeneity we need to include in the magnetic free energy the exchange interaction term, F_{ex}:

$$F_{ex} = \frac{A}{M_s^2}\nabla^2 \vec{M} \tag{2.65}$$

A is the exchange stiffness constant, which may be estimated as:

$$A = S\, J_{ex}\frac{a^2 M_S}{g\mu_B\mu_0} = \frac{2}{Z}k_B T_C\,\frac{a^2 M_S}{g\mu_B\mu_0} \tag{2.66}$$

S is the electron spin (1/2), J_{ex} is the exchange integral, a is the lattice constant, g is Lande factor (~2), μ_B is the Bohr magneton and μ_0 is the permeability of vacuum. After replacing J_{ex} two more notations are used: Z – the number of nearest neighbor spins and T_C – Curie temperature.

Considering that the spin-wave propagates perpendicular to the sample surface and the magnetic field, as well as the equilibrium magnetization direction, lies in the sample surface, the exchange energy can be expressed in spherical coordinates as follows:

$$F_{ex} = A\left[\left(\frac{\partial\theta}{\partial z}\right)^2 + \left(\frac{\partial\phi}{\partial z}\right)^2\right] \tag{2.67}$$

In Eq. (2.67) it was considered that the θ-value oscillates slightly around $\pi/2$ value, and the z-coordinate is aligned across the film. For a spin wave with a wavelength, $\vec{k}$, the exchange energy is simply:

$$F_{ex} = Ak^2\left(\theta^2 + \phi^2\right), \qquad k = \left|\vec{k}\right| \tag{2.68}$$

Since the spherical coordinates of the magnetization, θ and ϕ, are considered small in this approach, the exchange energy will not affect the equilibrium conditions (2.55) and (2.56), but the precession frequency will be affected. In fact both second derivatives of the free energy will increase with the same amount $2Ak^2$ and the equation (2.58) can be used again for calculating the frequency of the spin-wave branches. In thin film geometry, standing spin-waves may be generated [2.40]. In this case, the k-value is completely determined by the spin pinning conditions at the surface and interface. In the following, we will consider that the spins are not pinned at the surface and interface. A simple solution is available for this case:

$$k_n = \frac{n\pi}{d} \tag{2.69}$$

where d is the thickness of the film, and n is the order of the standing wave. The frequencies of the standing waves are given by:

$$\omega_n = \gamma_0 \sqrt{\left(H_1 + Dk_n^2\right)\left(H_2 + Dk_n^2\right)} \;;\; D = \frac{2A}{M_s} \tag{2.70}$$

When the film thickness is large, the equation (2.70) still holds as a quasi-continuous dispersion relationship. Beside the bulk exchange modes, surface precession modes are also possible. The wavevector, k, is contained in the film plane either perpendicular or parallel with the applied field. These waves are named magnetostatic, as their group velocity is very small and the exchange interaction influence is insignificant. With our notations their dispersion relations are respectively:

$$\left(\omega/\gamma_0\right)^2 = H_1 H_2 + \left(2\pi M_s\right)^2 \left(1 - e^{-2kd}\right) \;;\; \vec{k} \perp \vec{H} \tag{2.71a}$$

$$\left(\omega/\gamma_0\right)^2 = H_2 \left(H_1 + 4\pi M_s \frac{1 - kd - e^{-kd}}{kd} \right) \;;\; \vec{k} \parallel \vec{H} \tag{2.71b}$$

Such surface spin waves can be studied with magneto-optical Kerr microscopy [2.41, 2.42].

How the laser pulse is changing the magnetic properties of a thin ferromagnetic layer is still an open question. The fastest process seems to be a demagnetization effect. As the Landau-Lifshitz formalism does not allow a change in the magnetization value, the description of the demagnetization events or the temperature change close to the

Curie limit could be considered by using the Landau-Lifshitz-Bloch equation. To do so, the Eq. (2.47) should be augmented with a longitudinal relaxation term [2.43-2.45]:

$$\frac{d\vec{m}}{dt} = -\gamma_0 \left(\vec{m} \times \vec{H}_{eff}\right) + \frac{\gamma_0 \alpha_{//}}{m^2}\left(\vec{m} \cdot \vec{H}_{eff}\right)\vec{m} - \frac{\gamma_0 \alpha_{\perp}}{m^2}\left[\vec{m} \times \left(\vec{m} \times \vec{H}_{eff}\right)\right] \tag{2.72}$$

In Eq. (2.72) m is the spin polarization normalized to zero temperature value, and the longitudinal and transverse damping parameters, $\alpha_{//}$ and $\alpha_{\perp}$, respectively, are defined as functions of the actual temperature of the layer, T, and the Curie temperature, T_C:

$$\alpha_{//} = \frac{2T}{3T_c}\alpha \qquad and \qquad \alpha_{\perp} = \left(1 - \frac{T}{3T_c}\right)\alpha \tag{2.73}$$

The effective magnetic field, $\vec{H}_{eff}$, has to include an additional longitudinal term:

$$\Delta\vec{H}_{eff} = \frac{1}{2\chi_{//}}\left(1 - \frac{m}{m_{eq}}\right)\vec{m} \tag{2.74}$$

where $\chi_{//}$ is the longitudinal susceptibility, and m_{eq} is the equilibrium magnetization at a given temperature, T. By combining this macrospin approach with the ″two-temperatures″ model (see equation (2.1)), and considering that the spin temperature matches the electron temperature, T_e, it is possible to describe the ultrafast demagnetization /remagnetization dynamics in Ni [2.46]. Alternatively, a microscopic incoherent approach can describe the temperature influence on magnetization leading to the following equation [2.47]:

$$\frac{dm}{dt} = R\frac{T_e}{T_C}\left(1 - m\coth\left(\frac{mT_C}{T_e}\right)\right)m \tag{2.70}$$

where R is a material constant defined as:

$$R = 8a_{sf}g_{ep}V_{at}\frac{\mu_B}{\mu_{at}}\frac{k_B T_C^2}{E_D^2} \tag{2.71}$$

a_{sf} is the electron-phonon spin-flip probability, the g_{ep} is the electron-phonon coupling constant, V_{at} is the atomic volume, μ_{at} is the atomic moment, and E_D is the Debye energy. An analytical solution was observed to provide accurate fits of the demagnetization curves for Ni, where it was found that that the demagnetization/remagnetization dynamics is very fast and occurs on a sub-ps timescale [2.48].

As the present work was mainly focused on studying the spin dynamics in Fe films, showing a rather small demagnetization effect, and because the bulk of the measurements were conducted on the picosecond scale, it is more appropriate to use the original LL macrospin approach for data interpretation.

In deducing the frequency of the fundamental (Kittel) mode (equation 2.61), as well as the frequency of the standing spin wave (equation 2.70), we neglected the damping contribution. This might be a good approximation, as the value of damping constant, α, is usually small, $\alpha << 1$. However, if we need to estimate the slow decay time of precession amplitude, the damping constant is decisive. Let's consider a time dependence of magnetization factorized as: $\exp(-i\omega t)\times\exp(-t/\tau)$. In solving the precession equations (2.50), we need to consider the cancelation of the determinant:

$$\begin{vmatrix} i\omega+\frac{1}{\tau}-\alpha\gamma_0 H_2 & -\gamma_0 H_1 \\ \gamma_0 H_2 & i\omega+\frac{1}{\tau}-\alpha\gamma_0 H_1 \end{vmatrix} = 0 \qquad (2.72)$$

The real part of the determinant cancelation gives the approximate solution for ω (equation 2.58). The value of decay time for the Kittel mode, τ_0, is given by the cancelation condition for the imaginary part of the determinant:

$$\frac{1}{\tau_0} = \alpha\,\gamma_0\,\frac{H_1+H_2}{2} \qquad (2.73)$$

Using a similar approach for stationary spin waves, the following decay time results:

$$\frac{1}{\tau_n} = \frac{1}{\tau_0} + \alpha\,\gamma_0\,Dk_n^2 \qquad (2.74)$$

The decay equations (2.73) and (2.74) refer to the quasi-stationary solutions, when the spin dynamics was excited homogeneously through the whole film thickness. In practice, the laser excitation zone may be significantly smaller than the film thickness. In another extreme, it can be considered that the magnetization precession is excited only at the surface and its amplitude decays exponentially throughout the film thickness as:

$$\delta\vec{m} = \vec{m}_0\, e^{\mathbf{i}(\omega t+kz)}\, e^{-z/\langle z\rangle} \qquad (2.75)$$

where z is the coordinate across the film and $\langle z \rangle$ is the characteristic depth for the propagation of spin waves inside a semi-infinite metal. Canceling again the imaginary part of the determinant of the precession equations (2.58), the following solution results:

$$\frac{1}{\langle z \rangle} = \frac{\alpha\, \omega}{2\, \gamma_0\, Dk} \tag{2.76}$$

In fact the equation (2.76) predicts the depth of propagation for a spin wave with finite wavevector, k, and frequency, ω, inside a semi-infinite ferromagnetic material. The fundamental mode does not propagate (k~0); thus its depth should be determined by the excitation depth rather than the depth of propagation. On the other hand, the spin wave excitation source is not specified in the derivation of (2.76) and may depend strongly on the method used for spin wave excitation. When spin waves are excited with the use of optical pulses, one needs to consider the interplay between optical generation of photoelectrons and the subsequent thermalization of the electrons with themselves and with the lattice. These processes determine the depth of optical and thermal excitation inside the ferromagnet, which can in turn generate the coherent spin wave dynamics. If the excitation processes couple to spin dynamics and evolve on a timescale that is much faster than the spin wave frequency then their excitation can occur coherently. In practice, the coherent spin waves can be studied experimentally and the mechanism of their generation is expected to depend on the sample properties and experimental conditions. When femtosecond optical pulses are used for excitation of Fe samples, it is found that the coherent interaction of light with the dynamics of coherent spin waves is negligible, while it is the depth of thermal excitation that drives their dynamics (see Chapter 4). The depth of the thermal excitation of metallic ferromagnets is determined by the distribution of electronic temperature first, and then by the lattice temperature after the electron-phonon thermalization.

The description of spin wave propagation outlined in equations (2.65-2.71) is not a suitable approach for the case of *conductive* magnetic materials, as this quasi-static approximation completely ignores the electromagnetic nature of wave propagation. As was shown by Ament & Rado [2.49], the Maxwell's equations should be considered to ensure the additional cross correlation between magnetization and magnetic field in a conducting medium. The Maxwell's equations in a conductor may be written as follows:

$$\nabla\times\vec{E} = -\frac{1}{c}\frac{\partial}{\partial t}\left(\vec{H}+4\pi\vec{M}\right)$$
$$\nabla\times\vec{H} = \frac{4\pi}{c}\vec{j} \qquad (2.82)$$
$$\nabla\cdot\left(\vec{H}+4\pi\vec{M}\right) = 0$$

Considering only the conduction term in the electric field:

$$\vec{j} = \sigma\vec{E} \qquad (2.83)$$

σ is the conductivity of the film and c is the speed of light. Thus, the equations (2.82) can be combined to eliminate the electric field (see [2.50]):

$$\nabla\times\nabla\times\vec{H} = -\frac{4\pi\sigma}{c^2}\frac{\partial}{\partial t}\left(\vec{H}+4\pi\vec{M}\right) \qquad (2.84)$$

In the following we consider the x axis oriented along the static magnetization direction, and the applied static magnetic field is oriented in the same direction. The film surface is defined by the x and z directions, whereas the y axis crosses the film perpendicular to its surface. The small deviations of magnetization and magnetic field from equilibrium are described by wave functions of the form $\exp[i(ky-\omega t)]$. Thus the equation (2.84) translates to a one dimensional relationship [2.50]:

$$4\pi\, m_z = -\left(1+i\frac{\delta^2 k^2}{2}\right)h_z \;\; ; \;\; \delta^2 = \frac{c^2}{2\pi\omega\sigma} \qquad (2.85)$$

where δ is the classical skin depth. As opposed to the magnetostatic case, the spin waves in a ferromagnetic material induce an AC electromagnetic signal with the same frequency but a different phase. That can affect the spin wave damping characteristics. Following [2.51], after writing the LL equation in linear approximation and taking into account the relation (2.85), a set of linear homogeneous equations is obtained. A secular equation results by canceling the determinant. Prior work considered the above formalism to explain experimental results obtained with the ferromagnetic resonance technique, where the main goal was to find the solutions of k for a fixed ω and calculate the permeability versus frequency [2.49-2.51]. In our case, the main problem is to find ω as function of k and estimate the resulting damping. When considering the effect of finite conductivity, the dispersion law (2.70) for k>0 changes as follows:

$$\omega = \gamma_0 \sqrt{\left(H_1 + Dk^2\right)\left(H_2 + Dk^2 + 4\pi M_s\left(1 + \frac{\delta^4 k^4}{4}\right)^{-1}\right)} \tag{2.86}$$

Additional theoretical studies will be needed to establish the influence of finite conductivity on the change of the spin wave attenuation length, including its wavevector dependence. The main goal is to derive an alternate expression to the one from (2.74), which includes the effect of σ, while at the present we can already make two important concluding remarks. Firstly, we cannot apply directly the former exchange-conductivity theory of Ament-Rado [2.49], which was developed to connect with FMR experiments. This is because the excitation and probing conditions are substantially different in FMR and in the optical pump-probe experiments. In an attempt to clarify this issue, one important goal of this thesis is to establish the correct experimental phenomenology of spin wave propagation and attenuation. Secondly, it is clear that for the case of thick ferromagnetic films that exceed several tens of nanometers, the effect of finite conduction needs to be included via Maxwell equations for a proper understanding of the spin wave attenuation phenomena, as shown in Eqn. 2.86.

REFERENCES FOR CHAPTER 2

2.1 G. L. Eesley, "Observation of nonequilibrium electron heating in copper," Physical Review Letters 51 (23), 2140-2143 (1983).

2.2 J. G. Fujimoto, J. M. Liu, E. P. Ippen, and N. Bloembergen, "Femtosecond laser interaction with metallic tungsten and nonequilibrium electron and lattice temperatures," Physical Review Letters 53 (19), 1837-1840 (1984).

2.3 T. K. Cheng, S. D. Brorson, A. S. Kazeroonian, J. S. Moodera, G. Dresselhaus, M. S. Dresselhaus, and E. P. Ippen, "Impulsive excitation of coherent phonons observed in reflection in bismuth and antimony," Applied Physics Letters 57, 1004 (1990).

2.4 G. A. Antonelli, B. Perrin, B. C. Daly, and D. G. Cahill, "Mechanical and Thermal Properties Using Ultrafast Optical Metrology," MRS bulletin 31, 607 (2006).

2.5 B. Perrin, "Microscale and Nanoscale Heat Transfer, topics in Applied Physics, " S. Voltz, ed., Springer, Berlin, Vol. 107, pp. 333–359 (2007).

2.6 M. I. Kaganov, I. M. Lifshitz, and L. V. Tanatarov, "The electron-lattice relaxation," Zh. Eksp. Teor. Fiz 31, 232 (1956).

2.7 G. A. Garrett, T. F. Albrecht, J. F. Whitaker, and R. Merlin, "Coherent THz phonons driven by light pulses and the Sb problem: What is the mechanism?" Physical review letters 77 (17), 3661-3664 (1996).

2.8 A. Melnikov, I. Radu, U. Bovensiepen, O. Krupin, K. Starke, E. Matthias, and M. Wolf, "Coherent optical phonons and parametrically coupled magnons induced by femtosecond laser excitation of the Gd (0001) surface," Physical review letters 91 (22), 227403 (2003).

2.9 F. Hansteen, A. Kimel, A. Kirilyuk, and T. Rasing, "Femtosecond photomagnetic switching of spins in ferrimagnetic garnet films," Physical review letters 95 (4), 47402 (2005).

2.10 J. Y. Bigot, M. Vomir, and E. Beaurepaire, "Coherent ultrafast magnetism induced by femtosecond laser pulses," Nature Physics (2009).

2.11 P. Drude, Annalen der Physik 306, 566 (1900); *ibid.* 308, 369 (1900); P. Drude, The theory of optics (Longmans, Green, and Co., 1901).

2.12 R. W. Schoenlein, W. Z. Lin, J. G. Fujimoto, and G. L. Eesley, ″Femtosecond Studies of Nonequilibrium Electronic Processes in Metals,″ Phys. Rev. Lett. 58, 1680-1683 (1987).

2.13 S. I. Anisimov, B. L. Kapeliovich, and T. Z. Perelman, ″xxx,″ Sov. Phys. JETP 39, 375 (1975).

2.14 A. N. Smith, J. L. Hostetler, and P. M. Norris, ″Nonequilibrium Heating in Metal Films: an Analytical and Numerical Analysis,″ Numerical Heat Transfer, Part A, 35, 859-873 (1999).

2.15 S. D. Brorson, A. Kazeroonian, J. S. Moodera, D. W. Face, T. K. Cheng, E. P. Ippen, M. S. Dresselhaus, and G. Dresselhaus, ″Femtosecond Room-Temperature Measurements of the Electron-Phonon Coupling Constant λ in Metallic Superconductors,″ Phys. Rev. Lett. 64, 2172-2175 (1990).

2.16 P. B. Allen, "Theory of thermal relaxation of electrons in metals," Physical Review Letters 59 (13), 1460-1463 (1987).

2.17 C. A. Paddock and G. L. Eesley, ″Transient Thermoreflectance from Thin Metal Films,″ J. Appl. Phys. 60, 285-290 (1986).

2.18 D. G. Cahill, ″Analysis of Heat Flow in Layered Structure for Time-Domain Thermoreflectance,″ Rev. Sci. Instrum. 75, 5119-5122 (2004).

2.19 R. J. Stoner and H. J. Maris, ″Kapitza Conductance and Heat Flow between Solids at Temperatures from 50 to 300 K,″ Phys. Rev. B 48, 16373 (1993).

2.20 R. J. Stevens, A. N. Smith, and P. M. Norris, ″Measurements of Thermal Boundary Conductance of a Series of Metal-Dielectric Interfaces by the Transient Thermoreflectance Technique, ″Journal of Heat Transfer, 127, 315-322 (2005).

2.21 D. L. Balageas, J. C. Krepez, and P. Cielo, ″Pulsed Photothermal Modeling of Layered Materials ,″ J. Appl. Phys. 59, 2, 348-357 (1986).

2.22 B. Bonello, B. Perrin, and C. Rossignol, ″Photothermal Properties of Bulk and Layered Materials by the Picosecond Acoustics Technique,″ J. Appl. Phys. 83, 6, 3081-3088 (1998).

2.23 N. Taketoshi, T. Baba, and A. Ono, ″Development of a Thermal Diffusivity Measurement System for Metal Thin Films using a Picosecond Thermoreflectance Technique,″ Meas. Sci. Technol. 12, 2064-2073 (2001).

2.24 Y. Ezzahri, S. Grauby, S. Dilhaire, J. M. Rampnoux, and W. Claeys, ″Cross-Plan Si/SiGe Superlattice Acoustic and Thermal Properties Measurement by Picosecond Ultrasonics,″ J. Appl. Phys. 101, 013705 (2007).

2.25 W. S. Capinski, H. J. Maris, T. Ruf, M. Cardona, K. Ploog, and D. S. Katzer, ″Thermal-Conductivity Measurements of GaAs/AlAs Superlattice using a Picosecond Optical Pump-and-Probe Technique,″ Phys. Rev. B 59, 12, 8105-8113 (1999).

2.26 R. M. Costescu, M. A. Wall, and D. G. Cahill, ″Thermal Conductance of Epitaxial Interfaces,″ Phy. Rev. B 67, 054302 (2003).

2.27 C. Thomsen, H. T. Grahn, H. J. Maris, and J. Tauc, "Surface Generation and Detection of Phonons by Picosecond Light Pulses," Phys. Rev. B 34, 6, 4129-4138 (1986).

2.28 M. F. DeCamp, D. A. Reis, D. M. Fritz, P. H. Bucksbaum, E. M. Dufresne, and R. Clarke, "X-ray synchrotron studies of ultrafast crystalline dynamics," Journal of synchrotron radiation 12 (2), 177-192 (2005).

2.29 O. B. Wright, "Ultrafast nonequilibrium stress generation in gold and silver," Physical Review B 49 (14), 9985-9988 (1994).

2.30 H. N. Lin, R. J. Stoner, H. J. Maris, and J. Tauc, "Phonon attenuation and velocity measurements in transparent materials by picosecond acoustic interferometry," Journal of applied physics 69, 3816 (1991).

2.31 T. Saito, O. Matsuda, and O. B. Wright, "Picosecond acoustic phonon pulse generation in nickel and chromium," Phys. Rev. B 67, 205421 (2003).

2.32 G. Tas and H. J. Maris, "Electron diffusion in metals studied by picosecond ultrasonics," Phys. Rev. B 49, 21, 15046-15054 (1994).

2.33 S. Wu, P Geiser, J. Jun, J. Karpinski, and R. Sobolewski, "Femtosecond optical generation and detection of coherent acoustic phonons in GaN single crystals," Phys. Rev. B 76, 085210 (2007).

2.34 N. Del Fatti, C. Voisin, D. Christofilos, and F. Vallee, "Acoustic vibration of metal films and nanoparticles," Phys. Chem. A 104, 4321-4326 (2000).

2.35 H. Park, X. Wang, S. Nie, R. Clinite, and J. Cao, "Direct and real-time probing of both coherent and thermal lattice motions," Solid State Com. 136, 559-563 (2005).

2.36 H. Park, X. Wang, S. Nie, R. Clinite, and J. Cao, "Mechanism of coherent acoustic phonon generation under nonequilibrium conditions," Phys. Rev. B 72, 100301 (2005).

2.37 H. Tanei, N. Nakamura, H. Ogi, M. Hirao, R. Ikeda, "Unusual elastic behavior of nanocrystalline diamond thin films," Appl. Phys. Lett. 90, 191906 (2007).

2.38 M. Farle, "Ferromagnetic resonance of ultrathin metallic layers." Reports on Progress in Physics 61: 755 (1998).

2.39 D. Sander, "The correlation between mechanical stress and magnetic anisotropy in ultrathin films." Reports on Progress in Physics 62: 809 (1999).

2.40 M. Jirsa, "Angular Dependence of SSWR in Thin Metallic Films Approximate Analytical Solution." physica status solidi (b) 125(1): 187-196 (1984).

2.41 S. Tamaru, J. A. Bain, et al. "Measurement of magnetostatic mode excitation and relaxation in permalloy films using scanning Kerr imaging." Physical Review B 70(10): 104416 (2004).

2.42 Z. Liu, F. Giesen, et al. "Spin Wave Dynamics and the Determination of Intrinsic Damping in Locally Excited Permalloy Thin Films." Physical review letters 98(8): 87201 (2007).

2.43 D.A. Garanin, "Fokker-Planck and Landau-Lifshitz-Bloch equations for classical ferromagnets." Phys. Review B 55(5): 3050-3057 (1997).

2.44 N. Kazantseva, D. Hinzke, et al. "Linear and elliptical magnetization reversal close to the Curie temperature." EPL (Europhysics Letters) 86: 27006 (2009).

2.45 C. Bunce, J. Wu, et al. "Laser-induced magnetization switching in films with perpendicular anisotropy: A comparison between measurements and a multi-macrospin model." Physical Review B 81(17): 174428 (2010).

2.46 U. Atxitia, O. Chubykalo-Fesenko, et al. "Evidence for thermal mechanisms in laser-induced femtosecond spin dynamics." Physical Review B 81(17): 174401 (2010).

2.47 B. Koopmans, G. Malinowski, et al. "Explaining the paradoxical diversity of ultrafast laser-induced demagnetization." Nature Materials 9(3): 259-265 (2009).

2.48 F. Dalla Longa, J. T. Kohlhepp, et al. "Influence of photon angular momentum on ultrafast demagnetization in nickel." Physical Review B 75(22): 224431 (2007).

2.49 W. S. Ament and G. T. Rado, Phys. Rev. 97 1558 (1955).

2.50 A. Yelon, G. Spronken, et al. "Approximate method for ferromagnetic resonance in metals," Physical Review B 10(3): 1070-1074 (1974).

2.51 A. L. Sukstanskii, and V. Korenivski, "Impedance and surface impedance of ferromagnetic multilayers: the role of exchange interaction," Journal of Physics D: Applied Physics 34: 3337 (2001).

CHAPTER 3

EXPERIMENTAL DEVELOPMENT

Magnetization dynamics occurs by precession following external excitation, process during which the magnetization vector gradually realigns with the sum of external and internal magnetic fields of the ferromagnet. Studies of magnetization dynamics processes are of paramount importance for establishing the technological limits of magnetic device operational speeds as well as their reliability or the reproducible operation. This task needs to be accomplished at both theoretical and experimental level on the timescales where the magnetization relaxation processes occurs by either near-adiabatic conditions (picosecond to nanosecond timescale) or proceeds non-adiabatically (femtosecond to picosecond timescale). Examples of almost adiabatic processes are: the uniform and non-uniform magnetization precession and switching, long wavelength spin waves, and the dynamics of domain walls, while an example of non-adiabatic process is the femtosecond demagnetization induced with optical pulses.

The investigation of the magnetization dynamics in time domain is accomplished mostly with stroboscopic techniques, where a short laser pulse, a magnetic field pulse or an electrical current pulse triggers the process of excitation. To observe coherent phenomena, the excitation pulse duration is usually selected to be shorter than the system's fastest response time (if applicable). This type of measurement is referred as pump-probe technique, and its time resolution is determined by the time delay between the excitation (pump) and the magnetic parameter of interest that is being recorded (probe) at a specific sample location. In our own instrumentation development, which will be shown in this Chapter, we devised a novel optical pulse magnetometer (OPM) based on the pump-probe technique and the use ultrafast fiber lasers, which is compared with traditional pump-probe techniques first, and then tested trough measurements of heat transport, coherent phonon detection, and evaluation of spin wave damping (a measurement of their relaxation).

A brief summary of the sample preparation techniques is provided in Section 3.1, which were essential in obtaining high quality epitaxial films needed for obtaining reproducible behavior of their magnetic properties. The pump-probe method based on asynchronous optical sampling (ASOPS) is described in Section 3.2. We then show how this method can be used to study transient thermoreflectance (Section 3.3), coherent strain waves (Section 3.4) and coherent magnetization oscillations (Section 3.5).

3.1 Metallic Thin Films Growth using Molecular Beam Epitaxy (MBE)

Molecular Beam Epitaxy (MBE) is a technique that assures monolayer (ML) control for producing high quality epitaxial structures in Ultra-High-Vacuum (UHV) environment. Originally developed as a tool for growing high-purity semiconductor films, MBE has demonstrated widespread capability for producing epitaxial layers of metals, insulators and superconductors, at the research and the industrial production level. We use this technique for preparation of high quality epitaxial thin films by taking advantage of the monolayer control and the clean environment during deposition (pressure ~ 10^{-10} Torr) assured by MBE. Regarding the preparation of the one layer or multilayer samples used in this thesis we reported, in a series of publications [3.1-3.4], the procedures for obtaining high quality epitaxial films along with their main structural characteristics. Some specific information will be provided for particular samples in the corresponding sections, including the description of the corresponding pump-probe experiments.

3.2. Asynchronous Optical Sampling Instrument and Measurements

Time-resolved pump-probe optical spectroscopy based on ultrafast lasers is often used to study laser-induced transient-dynamics in solid-state materials. An intense laser-pump pulse induces a fast perturbation of the material properties, the evolution of which can be studied through concomitant changes in the optical properties, as measured by a time-delayed probe pulse. Typically the probe pulse is derived from the pump, and delayed by mechanical means [3.5]. We demonstrate a new approach for performing

dynamic measurements [3.6] over a very large temporal range using a newly developed instrument based on ultrafast fiber lasers and asynchronous optical sampling (ASOPS). The potential of the technique is illustrated by measurements on the thermal, mechanical, and magnetic properties of epitaxial iron thin films and their supporting substrates. Particular emphasis is placed on coherent magnetization oscillations and their relaxation. A key aspect of this is how to separate the spin-wave effects from the non-magnetic contributions to the transient optical response.

Optical pump-probe spectroscopy applications are already well developed for characterizing the transient dynamics of materials. Examples include acoustic wave propagation, thin film thickness and adhesion to the substrate, the evaluation of thermal properties such as thin film thermal conductivity and thermal boundary resistance [3.7], and the generation and detection of coherent optical phonons [3.8]. These measurements are traditionally performed using slow mechanical scanning of an optical retro-reflector to achieve the pump-probe time delay. This limits the speed and efficiency of data acquisition, especially when extended time delays are required. In the present study, based on the ASOPS technique with kilohertz scanning rates, we present a great improvement of the experimental approach able to cover time delays from femtoseconds to several nanoseconds. We emphasize that the scanning over several nanosecond time delays takes full advantage of the ASOPS technique by eliminating the need for mechanical translation over large distances, which usually requires systematic error compensation [3.9].

While the principle of the ASOPS technique was established about three decades ago [3.10-3.11], it was only recently implemented by Bartels et al. [3.12] for the efficient detection of coherent acoustic phonons, based on a dual ultrafast Ti-sapphire laser system operating at gigahertz repetition frequency. While such experimental capabilities are very attractive, the total time span was limited to one nanosecond, imposed by the laser repetition rate. In the present study, the ASOPS technique capabilities are extended over much longer timescales for measuring relatively slow relaxation processes, such as thermal cooling and the detection of long-lived coherent acoustic or magnetic oscillations. The measurements make use of fiber lasers with 100 MHz repetition rates, providing up to 10 ns transit time before the next stroboscopic excitation arrives and

subsequent probing is repeated. Moreover, with the newly developed method described here, measurements at the very short, femtosecond, time scale are also achieved under optimal conditions, with a detection bandwidth of 6 THz, limited primarily by the duration of the probe pulse. We have used the same system to generate and detect the coherent optical phonons in a number of materials, including Sb and Bi.

The experiments reported here are motivated by the need to connect long and short time scales associated with the relevant excitation processes in epitaxial magnetic thin films. These include optically stimulated thermal transport, lattice excitations and spin dynamics. The ultrafast pump-probe system presented here is an ideal instrument to access the disparate time-scales of these coupled processes.

Multicolor (non-degenerate) pump-probe measurements were carried out using a specially designed dual-fiber-laser system from Menlo Systems GmbH [3.13]. A schematic of the experimental arrangement is shown in Figure 3.1, including the dual-laser system, the electronic detection scheme and the optical components. The dual-laser system uses two separate passively mode-locked lasers based on Er-doped fiber, with each laser providing output pulses of 1.5 nJ energy and 80 fs duration at the fundamental wavelength of 1560 nm. The two lasers have slightly different repetition rates, with one laser (the slave) locked to the other (the master) with a fixed offset frequency. The slave laser is frequency doubled through the second harmonic generation (SHG) up to a wavelength of 780 nm, with the pulse duration of 150 fs and the energy of 0. 4 nJ. A residual beam at 520 nm corresponding to a third harmonic generation (THG) is also available at a reduced level of <0.01 nJ. The SHG beam from the slave laser, was used mostly as the probe, while, in some cases, the THG can still be used for optical probing at a secondary wavelength.

Continuous scanning in the time-domain was achieved by stabilizing the repetition rate asynchronism (frequency difference) between the two mode-locked lasers. The individual laser repetition rates are close to 100 MHz while being stabilized [3.13] to a small and constant difference repetition frequency, selectable between 0.2-7 kHz.

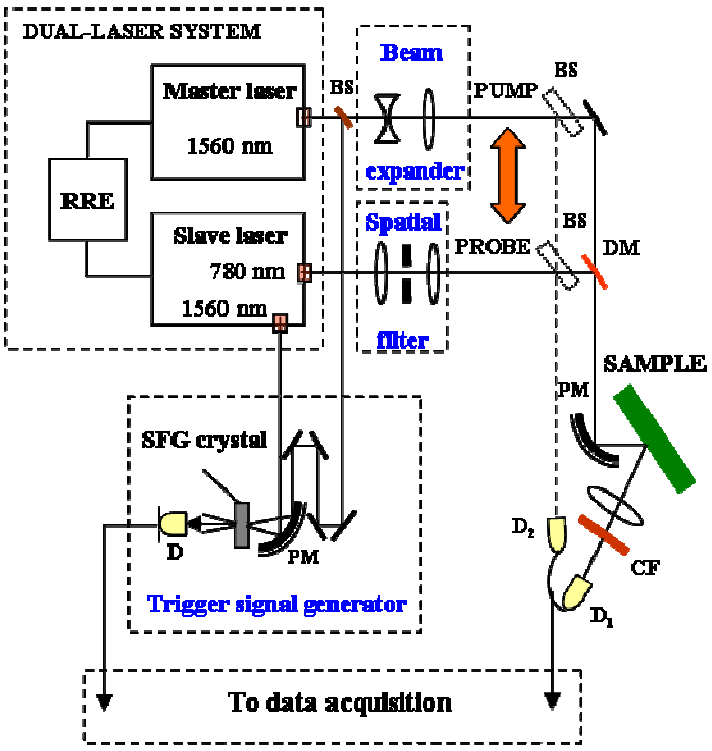

Figure 3.1 Schematic of the experimental setup with collinear pump-probe geometry: RRE - repetition-rate synchronization electronics; BS - beam splitter; DM - dichroic mirror; PM - parabolic mirror; CF - color filter; D, D1, D2 - detectors; SFG – sum-frequency generation.

The fixed rate difference between the pump and probe lasers ensures that a continuous variable time delay is realized [3.6, 3.10-3.14] between the two laser pulses. The maximum temporal scanning interval (τ_s) is the time-interval between pump pulses, which is given by the inverse frequency of the master laser $\left(\tau_s = \frac{1}{f_1}\right)$. The temporal resolution is determined by the most significant of: the limited detector bandwidth, the laser pulse duration and the pulse-to-pulse jitter. The detector bandwidth contribution is taken into account through $\tau_b = \Delta f / f_1 B$ [3.11], where B is the effective bandwidth of the detection and corresponds to 50 MHz in the present studies. A computer-based digital-oscilloscope, with 100 MHz analog bandwidth, is used for data acquisition. The oscilloscope sampling rate corresponds to a 10 ns interval, which coincides with $1/f_1$ to provide direct conversion to τ_s in the experiment. Hence, with our experimental apparatus, the corresponding bandwidth limit to the time resolution varies from 40 fs to

1.4 ps based on the accessible Δf values provided by the dual-laser system. Depending on the particular measurement resolution requirements, a suitable value for Δf was chosen during the experiment for time delay scanning, and the accumulation and averaging of 10^4 - 10^7 temporal traces was used for noise suppression.

To optimize our temporal resolution and accomplish real time triggering during the data acquisition process, we have constructed an *optical cross-correlator* using a beam splitter derived portion from the master laser together with a residual beam at the fundamental wavelength from SHG unit of the slave laser. The two laser beams are focused by a 90^0 off-axis parabolic mirror on a beta barium borate (BBO) crystal to obtain a sum frequency generated (SFG) cross-correlation beam at 780 nm, monitored by an amplified photodiode with 150 MHz analog bandwidth. The mirror-based focusing helped to increase the efficiency of SFG generation compared with lens-based focusing by eliminating chromatic aberrations to provide a better beam overlap inside the BBO crystal. The measured temporal width of the cross correlation signal is 160 fs.

Even with optical triggering, additional time-resolution constraints are imposed by the timing-jitter contribution of the dual-fiber-laser system that accumulates during the course of an experiment. To estimate the timing jitter, we have measured a second cross-correlation after a time delay of 10 ns between successive pump pulses. By comparing the first (160 fs) and the second (300 fs) cross-correlation widths, we determine that the timing jitter accumulates at a rate of ~15 fs for every nanosecond of time delay, following the trigger signal. To minimize the effects of timing jitter at short time delays, we carefully matched the travel distances of the optical beam paths of the pump and probe beams with the corresponding ones inside the cross-correlator. In this way, a maximum bandwidth of 6 THz could be reached, which was important for achieving the detection of coherent optical phonons in Sb and Bi [3.8]. In Figure 3.2 is given an example of the coherent optical phonon detection in an Sb thin film, using a pump laser fluence of 25 $\mu J/cm^2$. Both A_{1g} and E_g modes are detected and their frequencies (4.51 THz and 3.39 THz, respectively) are in excellent agreement with the first-order Raman scattering results [3.15] and prior time-domain data reports [3.16]. Thus, optical phonon frequencies, measured at small pump power excitation levels, provided a successful test for the experimental setup calibration.

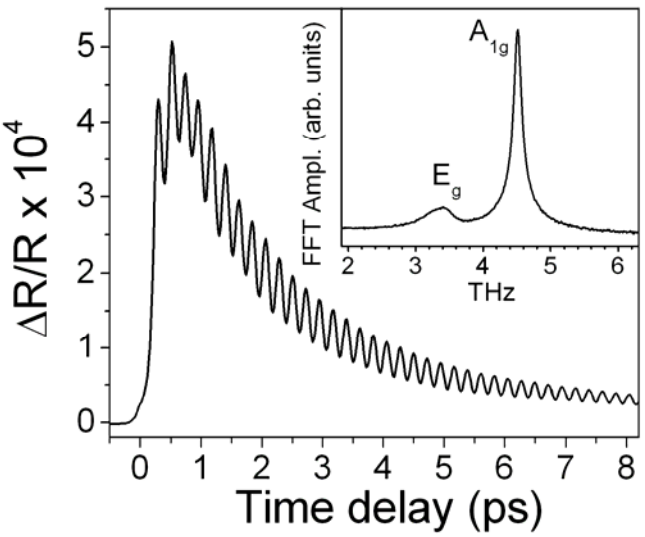

Figure 3.2 Coherent optical phonon reflectivity oscillations detected in an Sb thin film grown on (111) Si substrate. The pump (1560 nm) and probe (789 nm) beams are both s-polarized and collinear. The FFT in the inset corresponds to the oscillatory part of the signal after subtraction of the slowly varying background.

The laser output beams were individually expanded to reduce beam divergence, while a dichroic mirror is used to direct, collinearly, two-color beams toward a parabolic mirror to focus them on the sample at an oblique angle of incidence of 30^0. A 90^0 off-axis parabolic mirror was employed for eliminating the chromatic aberrations and to facilitate precise dual-color focusing overlap; this was necessary for achieving phase matching during the coherent excitation and probing. The pump and probe individual wavelengths could be interchanged by replacing the focusing beam expander lenses to a spot size of about 10 μm or smaller, while maintaining a pump-probe spot size ratio of 2. A half waveplate followed by a polarizer (not shown in Figure 3.1) was placed into the probe optical beam path to adjust the pump-probe intensity ratio to a factor of 10-100. Changes in the time-dependent sample reflectivity were measured with an amplified differential photodetector. The difference between the reflected probe light and a reference derived from the incident probe light in two matched diodes is amplified, and the output is low-pass filtered to a 50 MHz bandwidth to suppress the detection of the laser repetition rate signal at 100 MHz. The use of the fast detector combined with the optical trigger eliminates the need for modulator referencing in conjunction with lock-in amplifier, as is the case in single laser pump-probe techniques [3.5,3.7-3.9,3.17].

The dual-laser ASOPS system, providing a large temporal dynamic range, is extremely advantageous for studies of samples in which several excitations are active over a wide range of time scales. Such is the case for epitaxial thin films of Fe deposited on MgO and Ge substrates. We illustrate the power of this approach through a series of transient reflectivity measurements to detect the thermoreflectance signal and coherent strain wave propagation, while coherent magnetization oscillations were probed with polarization analysis under an external magnetic field. Separation of the magneto-optical Kerr effect (MOKE) from non-magnetic contributions using the probe beam polarization is discussed in the following.

The time-domain version that is used in this thesis, is referred as the time-resolved Magneto-optical Kerr effect (TR-MOKE), a technique that monitor lights polarization changes upon reflection from an opaque ferromagnet during the evolution of the magnetization dynamics when excited out of equilibrium. The TR-MOKE polarization changes are determined by the spin and the orbital degrees of freedom, while their coupling (spin-orbit coupling) determines the relation between the Kerr signal and the magnetization orientation. This technique has "vectorial" capability, meaning that it can be used to determine the three dimensional trajectory of uniform spin precession. For the cases when the magnetization dynamics proceeds nonuniformly, the tree orthogonal magnetization projections, averaged spatially in the probed sample region, can also be measured. Special care needs to be devoted to distinguish between these to different cases.

Magnetization dynamics can be observed by monitoring the oscillation frequency, which is strongly dependent on the field strength. The external magnetic field was applied along the sample surface using a small permanent magnet with its pole axis placed parallel with the sample and perpendicular to the horizontal optical scattering plane. The permanent magnet enabled us to obtain measurements quickly and conveniently; however it should be pointed out that the magnetic field it produces is not spatially uniform and includes both in-plane and out-of-plane components, although it did not vary significantly across the measurement spot size of at most 10 μm. The permanent magnet provided a magnetic field strength of up to 0.25 T and its amplitude could be tuned by varying the magnet-to-sample separation distance.

The detection of the magnetization dynamics was made first in reflectivity measurements (without using an analyzer) at all orientations of the probe beam polarization except for s-polarized light. This observation is consistent with the detection of transversal MOKE and rules out the possibility of second order MOKE effects that would be present for both s and p polarized light [3.18]. In order to detect the MOKE polarization rotation, an analyzer (not shown in Figure 3.1) was inserted in front of the detector at angles larger than 45^0 with respect to the incident beam polarization. When the analyzer is gradually rotated toward extinction, the isotropic reflectivity contribution to the signal is reduced, while the polarization rotation related to polar and longitudinal MOKE is more effectively measured. That is indeed what we observed, with improved sensitivity compared with the transversal MOKE detection. The separation of the longitudinal and polar contributions was done by performing complementary measurements at s and p polarizations of the incident beam and with the analyzer at an angle of 45^0 (see Figure 3.3).

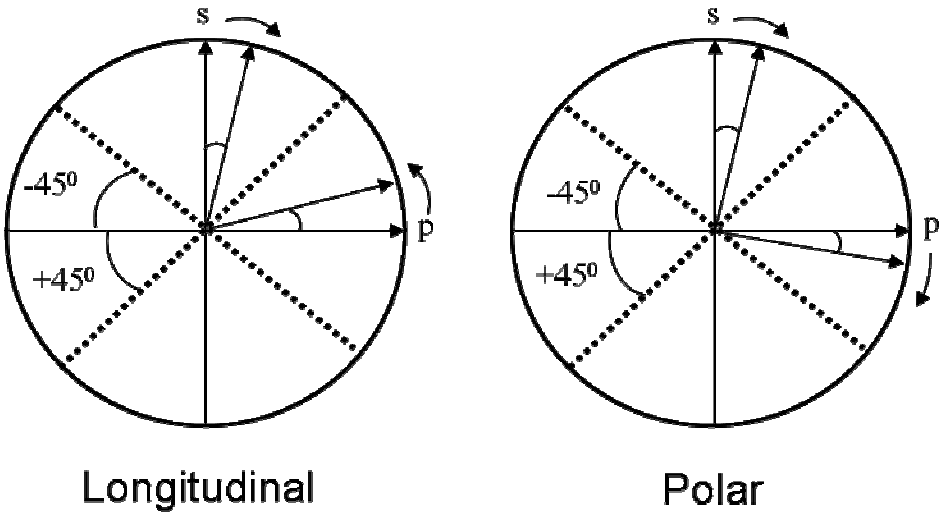

Figure 3.3 Scheme used for the component-resolved MOKE separation described in the text. Vertical (s-polarized) and horizontal (p-polarized) lines represent the incident probe polarization on the sample. Sample-induced MOKE polarization rotation, for longitudinal and polar magnetization components, is sketched using displacement of arrows. Dashed lines at 45^0 represent the orientation axis of the analyzer placed in the probe beam after reflection from the sample.

Taking into account that the polar MOKE does not change sign when changing the polarization of incident beam from s to p, while the longitudinal MOKE does [3.19], we

have added and subtracted the measurements at a 45^0 analyzer angle in order to separate the two contributions. We note here that the optimal MOKE detection can be achieved using orthogonal polarization-balancing, based on polarizing beam splitters to eliminate the non-magnetic reflectivity signal contributions and reduce the measurement noise. However, using such an approach alone could, in some cases, mix the true magnetic polarization rotations with anisotropic reflectivity changes related, for instance, to Raman-type scattering used for the detection of coherent optical phonons [3.20]. It is then necessary to perform an appropriate separation of the measured signal components by selecting the most favorable detection scheme.

Additional experimental details will be presented as we describe the results in the following sections. We emphasize here the efficiency of the ASOPS scanning as compared to mechanical scanning. The former is typically done at kilohertz rates, while fast mechanical delay lines are moving with speeds on the order of 0.5 m/s. Thus, the ASOPS scanning speed is at least four orders of magnitude larger than mechanical scanning for time delays approaching 10 ns.

3.3 Transient Thermoreflectance

The first example we present refers to transient thermoreflectance measurements performed on metallic layers grown on a single crystal substrate. This is where the unprecedented ability of our approach to connect long and short time regimes really comes into play, enabling us to follow the thermal transport from the initial excitation to much later times corresponding to the heat propagation deep into the substrate. Two epitaxial 70 nm thick Fe films were grown by molecular beam epitaxy (MBE) on (110) Ge and MgO substrates, and covered with a 4 nm overlayer of Au to protect the surface from oxidation under ambient exposure. The presence of the thin Au overlayer is assumed to be negligible in the following analysis. The metallic film thickness of Fe was chosen to be much larger than the laser probing depth, thus suppressing any contribution to the measured transient reflectance due to the direct optical excitation of the substrate.

First, at short time delays (ps), the transient reflectance is dominated by the non-equilibrium excitation of hot electron plasma near the thin film surface, which is rapidly

thermalized through electron-phonon relaxation [3.24]. Figure 3.4 compares the thermal cooling curves following the pump pulse excitation at 1560 nm, plotted over the entire range of maximum time delay of 10 ns corresponding to the pump laser repetition rate. The analysis was focused on describing the later stages of cooling from the picosecond to nanosecond time scale, using a simple heat diffusion model proposed by Stevens et al. [3.22,3.23]. A least squares minimization procedure was implemented to adjust the numerical solution of the heat diffusion equation, with appropriate boundary conditions, to the experimental data. In addition to letting the film-substrate boundary conductance (σ_k) and heat penetration depth (δ) vary as free parameters, we also allow the film thermal conductivity (k_f) to be adjustable, while keeping specific heats and substrate thermal conductivity (k_s) at known values corresponding to the bulk material. In addition, we have compensated for heat accumulation effects during repetitive pulse excitation [3.9, 3.17, 3.24] by adding a constant background offset (R_b) to the experimental data before comparing with the solution of the diffusion equation.

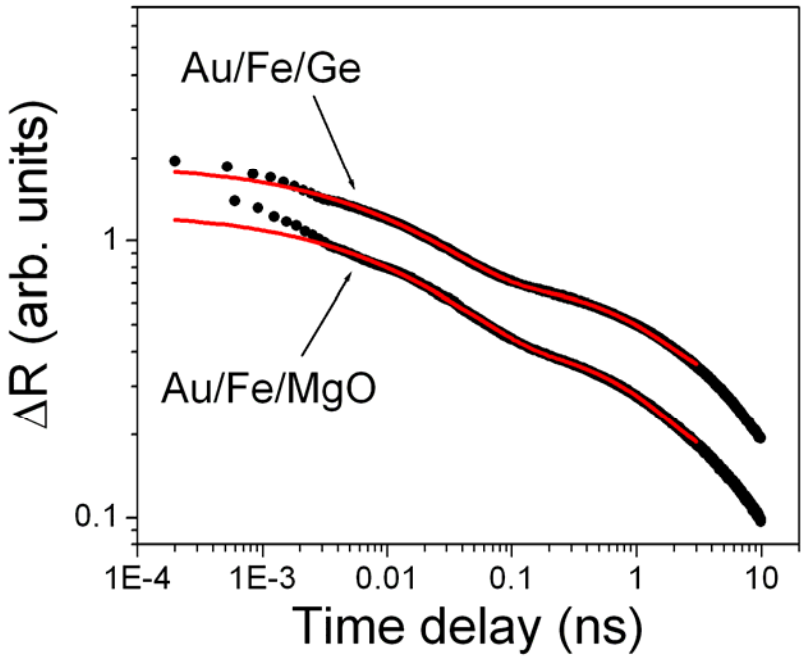

Figure 3.4 The thermoreflectance experimental data (dots) and numerical fit curves from Eqs. 2.7-2.9 (solid lines) for two different multilayer structures: Au/Fe/Ge and Au/Fe/MgO. The curves are rescaled and displaced for clarity.

A very good fit to the experimental data could be obtained for up to 3 ns of time delay for both samples, and the result is plotted in Figure 3.4. A larger σ_k of 2.5×10^8 W/m^2K is obtained for the Fe/MgO interface compared with 2.1×10^8 W/m^2K corresponding to the Fe/Ge interface. This is the reason why the cooling takes place faster on the MgO rather than Ge substrate between 100 ps and 3 ns. The relatively large boundary conductance σ_k reported here and compared with the data from [3.19] obtained for other film/substrate combinations, could be the result of a smaller acoustic mismatch for the case of our samples. The reflection coefficients R_k are calculated in the acoustic mismatch limit [3.20], based on the known bulk values for sound velocity and mass density. R_k values of 2.7% and 6.8% are then calculated for the Fe/MgO (110) and Fe/Ge (110) interfaces, respectively. The smaller acoustic mismatch calculated for the Fe/MgO interface correlates well with the larger σ_k measurement. Additionally, we note that the film/substrate combinations used in the present study have relative sound velocities and Debye temperatures that are reasonably matched within less than a factor of 2, enabling efficient phonon transmission across the interface [3.20]. Accordingly, a relatively large σ_k is expected for our samples in agreement with the experimental results. On the shorter time scale the cooling slopes are similar and given by k_f values of 33 and 46 W/Km, corresponding to the Fe/MgO and Fe/Ge thin films respectively. As expected for thin films [3.25], the values of the thermal conductivity are smaller than the one corresponding to the bulk material. The obtained δ values of 18-22 nm are very close to the optical penetration depth at the 1560 nm wavelength for the bulk iron. Although we have fitted the experimental data starting from 10 ps after the pump pulse excitation, good agreement with the thermal diffusion model was found down to 3 ps of time delay after the initial excitation, indicating that the electrons-phonon relaxation is already completed during the first 3 ps. We estimate the experimental uncertainty by fixing δ = 22 nm at the average value obtained from previous Fe optical constant measurements [3.26,3.27] and varying σ_k around its best fitting value. If allowing the other free parameters to vary, it can be observed a good match with experiment for up to 30% deviations in σ_k. The obtained boundary conductance values are clearly model dependent and are sensitive to the temporal range over which data is available. In particular, we note that two missing ingredients from the adopted thermal model [3.22] are the thermally

accumulated background produced by repetitive excitation, and the lateral heat flow. The former contribution suggests that the small slope of the spatial profile of the accumulated thermal background cannot be neglected when trying to understand the cooling at long time delays. In our experiments, it is observed that the average measured background reflectivity, defined as the pump-induced reflectivity change at the immediate instant prior to the pump excitation, has values of 40-60% relative to the transient thermoreflectance signal, which corresponds to a temperature rise ~ 10^0C (at pump fluence of 2 mJ/cm^2). Consequently, the heat accumulation effects produced by repetitive pulse excitation at 100 MHz are expected to play an appreciable role for the long time delays where the transient thermoreflectance has decreased to low levels. This uncertainty could be reduced if (a) the measurements are done at longer intervals between pulses, (b) the laser repetition frequency is lowered, or (c) using pulse picking techniques. To our knowledge this is the first data of its kind on Fe/Ge and Fe/MgO boundary conductance. However, we can compare our findings with the trends exhibited by other film/substrate combinations having similar Debye temperature ratios [3.22, 3.26]. For our case the film/substrate Debye temperature ratio are 0.62 and 1.25 for Fe/MgO and Fe/Ge, respectively. Inspection of the Figure 5 from [3.22] reveals that our results are close to prior reports within the uncertainty of the experiment.

3.4. Coherent Strain Wave Propagation

Ultrashort laser pulses can also excite coherent uniaxial strain waves propagating perpendicular to the sample surface toward the bulk [3.29]. Such strain waves can be detected via oscillatory contributions of the transient reflectivity with frequency equal to $\frac{2nv\cos(\theta)}{\lambda}$, where v is the speed of sound, n is the index of refraction at the wavelength λ, and θ is the angle of incidence inside the probed material.

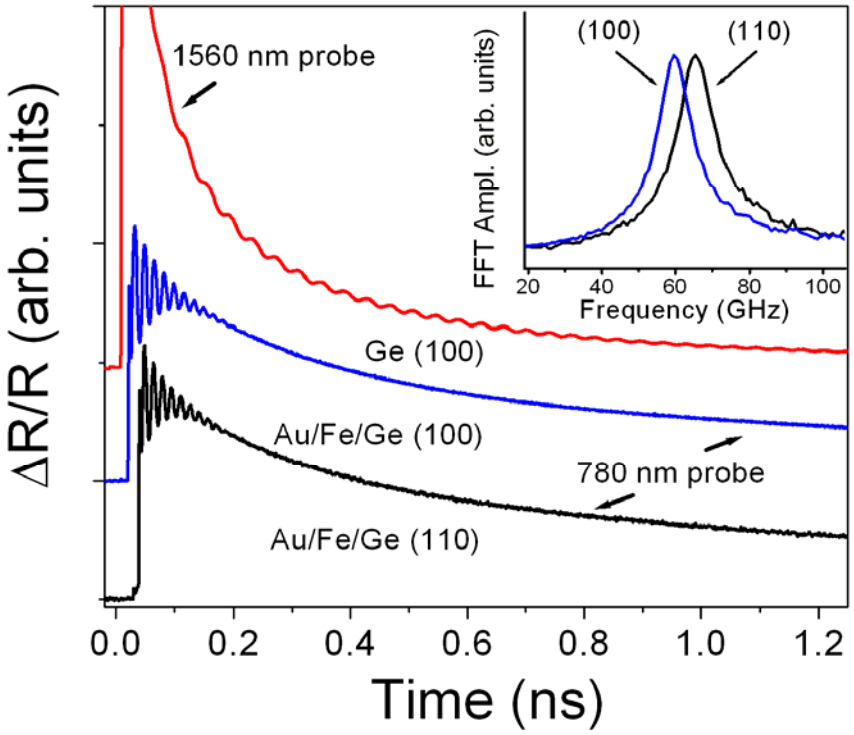

Figure 3.5 The experimental transient reflectivity for two pump-beam wavelengths: 780 nm (the two lower curves) and 1560 nm (the upper curve). The curves are rescaled and displaced for clarity. The FFT in the inset corresponds to the oscillatory part of the signal of the experimental curves for the multilayer structures of Au(4nm)/Fe(10nm)/Ge (100) and Au(4nm)/Fe(16.5nm)/Ge (110).

To probe the bulk strain wave propagation after surface excitation, we have used either bare Ge substrates or 10-15 nm Fe epitaxial films deposited on (100) and (110) Ge substrates and covered with Au overlayers. Systematic investigations were performed by switching the individual pump and probe wavelengths. In Figure 3.5 we compare an experimental curve obtained on a 10 nm Fe film grown on (100) Ge substrate that is probed at 780 nm wavelength, with a measurement on a bare (100) Ge wafer when probing at the complementary wavelength of 1560 nm.

A long oscillation on the nanosecond time scale can be probed with 1560 nm wavelength on the bare (100) Ge. We attribute the detection enhancement of the photoacoustic contribution to a resonant condition for probing at the direct bandgap absorption edge, as was seen previously for the case of GaSb-GaAs heterostructures

[3.30]. In the case of non-resonant probing at 780 nm, the presence of a thin absorptive Fe film at the 1560 nm pump wavelength permitted partial optical transmission of the probe in Ge, facilitating the observation of the bulk strain propagation. In the short lived oscillation curves in Figure 3.5 corresponding to such thin Fe films deposited on Ge substrates**,** we observe that changing the probing wavelength to 780 nm rapidly reduces the amplitude of the signal when the strain wave propagates deep into the substrate. Such behavior could be explained based on the shorter optical penetration depth in Ge at 780 nm compared with the one at 1560 nm. The reflectivity oscillations are still clearly visible up to 250 ps, enabling an accurate speed of sound determination.

An even more drastic increase of the oscillation amplitude decay occurs when probing at a wavelength of 520 nm, consistent with a corresponding large increase of wavelength dependent absorption [3.31]. The inset from Figure 3.5 compares two fast-Fourier-transform (FFT) spectra of the oscillatory part of time resolved spectra, measured with a 780 nm probe on 10 to15 nm thick iron films grown on (100) and (110) Ge substrates. Using the peak frequencies and 4.74 for the index of refraction [3.31], we obtain 4.96 and 5.43 km/s for the longitudinal sound velocity along the [100] and [110] crystallographic directions, respectively, in excellent agreement with the earlier published data for crystalline Ge [3.32].

When measuring at the complementary probe wavelength (520 nm), it is observed that the reflectivity oscillation frequency increased by about 52% when replacing 780 nm with 520 nm for the probe (not shown in Figure 3.5). This result confirms that the corresponding increase of $\frac{2nv\cos(\theta)}{\lambda}$ is in agreement with the above determination of v and the prior index of refraction measurement at 520 nm [3.31]. We note here that the wavelength dependent detection studies could be used to obtain both v and the index of refraction.

3.5 Coherent Magnetization Oscillations

The detection of coherent magnetization oscillations excited by ultrafast optical pulses, based on mechanical time-delay scanning, was previously reported in samples comprising of antiferromagnet-ferromagnet coupled layers [3.33] or single ferromagnetic layers [3.34,3.35]. The measured oscillation frequencies can be related to magnetic anisotropy contributions, saturation magnetization, and exchange interaction. Such studies are usually limited to time delays of around 1 ns, being susceptible to errors related to spot size variations and pointing instabilities present during the mechanical scanning. It is of interest to apply all-optical pump-probe techniques combined with fast ASOPS scanning to the measurements of magnetic damping phenomena extended here to long time delays while reducing the measurement errors.

A simple estimate for the oscillation amplitude decay time can be made using $\tau = 1/2\pi f\alpha$, where τ is the exponential decay time, α is the intrinsic Gilbert damping rate, and f is the resonant frequency. Such an expression is valid when applying large magnetic fields perpendicular to the sample surface. When choosing a resonant frequency of 20 GHz, and considering the value for α reported for high quality Fe and FeCo alloys [3.36], one would expect a relaxation time of around 4 ns. Thus, extending the time delay for accurate measurements of intrinsic Gilbert damping is highly desirable.

An experimental curve of the coherent magnetization oscillations, measured using our approach is shown in Figure 3.6a. The measurement is performed on a 15 nm epitaxial iron film sample (overcoated with 4 nm of Au) grown by UHV evaporation on a (110) Ge substrate. An external magnetic field of about 0.15 T was applied close to the in-plane easy axis, while an analyzer was placed in front of the detector at an angle of 75^0 with respect to the probe beam polarization. Long-lived coherent magnetization oscillations can be resolved for time delays of up to 9 ns, although only the first 2 ns are displayed in the curves shown in Figure 3.6a. After extracting the non-coherent background contribution to the signal, it is observed that the peak-to-peak oscillation period has a small time-delay dependency and does not exhibit a single exponential decay.

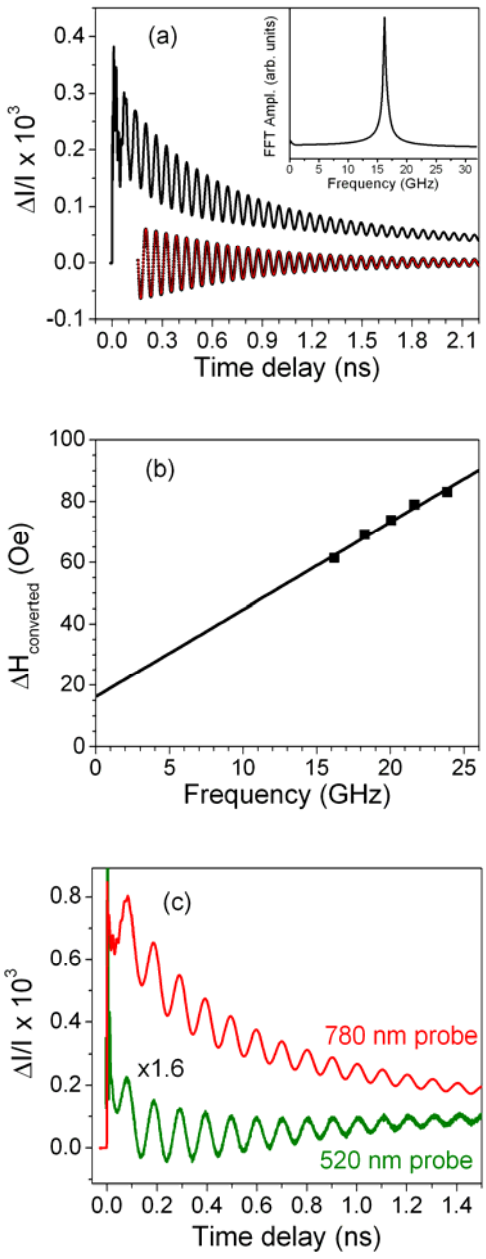

Figure 3.6 The coherent magnetization oscillation measurements for the (110) Fe/Ge sample: (a) The experimental (upper curve) and calculated (lower red line) after background substraction of the oscillatory trace detected at 780 nm probe wavelength and H ≈ 1000 Oe, (b) The equivalent magnetic field linewidth values (squares) and the best linear fit (solid line), and (c) Comparison of the experimental results obtained at 780 nm and 520 nm probe wavelengths, and H ≈ 100 Oe. The ratio, ΔI/I, is the fractional transmission through the analyzer in (a) and (c).

In principle, such an observation may result from the time varying thermal gradients that were specifically measured and presented in Section 3.3, but are not taken into account in the present analysis. We have, rather, employed a simple linear superposition of two exponentially damped cosine modes to model our data. The fitting result included in Figure 3.6a shows complete agreement with experiment. The data from the first 150 ps were excluded from the fit in order to eliminate the portion of the experimental curve that contains the acoustic signal discussed in Section 3.4. The fit, which extends to 6 ns of time delay, reveals a large contribution from a stronger mode decaying with a time constant of about 0.9 ns together with a ~3x weaker contribution from a faster decaying mode with 0.55 ns relaxation time. The relative phase shift between the two modes is found to be $\pi/2$ ±15%, which suggests that the two modes involve dynamics with orthogonal magnetization components. The two modes have slightly different frequencies separated by a 1-2% of relative frequency shift with the faster decaying mode corresponding to the larger frequency. It should be emphasized that the FFT of the data, shown in the inset from Figure 3.6a, cannot easily identify a dual contribution from closely spaced modes, while time-domain data analysis can separate them using their individual phases. For a fixed spot on the sample, we have varied the magnetic field strength to obtain the frequency dependence of individual mode decay times, for oscillation frequencies between 15 and 25 GHz. The larger frequency dependence is observed for the more intense mode, which corresponds to spin precession around the in-plane magnetic field direction. A full description of the weaker mode dynamics was not explored at this time and more studies are needed to elucidate its nature. Suffice it to say that due to the relatively weak frequency dependence of the decay time and the relative phase shift of $\pi/2$, this mode could be related to either the precession around the out-of-plane magnetic field component, which was present in our experiment, or with some particular sample non-uniformities that could enhance the local spin precession damping.

To compare our data with prior experiments using ferromagnetic-resonance (FMR) spectroscopy, the following frequency expression is considered, obtained from the Landau-Lifshitz equation [3.37] (see also 2.61-2.62 with slightly different notations):

$$\left(\frac{2\pi f}{\gamma}\right)^2 = \left[H\cos\left(\phi_M - \phi_H\right) + H_{k1}\right]\left[H\cos\left(\phi_M - \phi_H\right) + H_{k2} + 4\pi M_{eff}\right] \qquad (3.1)$$

where f is the precession frequency, γ is the gyromagnetic ratio, H is the external magnetic field applied parallel to the sample plane, ϕ_M is the magnetization orientation angle, ϕ_H is the angle of the external field orientation, H_{k1} and H_{k2} represent the magnetocrystalline anisotropies that are specific to the sample orientation and include additional anisotropies characteristic of very thin films [3.37], and M_{eff} represents the average magnetization value that can deviate from the bulk value and includes the out-of-plane uniaxial anisotropy. This frequency expression is valid for uniform spin precession around the in-plane magnetic field and neglects exchange interaction contributions related to either the surface anisotropy or to the presence of standing spin-wave modes. The exchange interaction can be considered by adding Dk^2 to both H_{k1} and H_{k2} from equation (1), where D is the spin stiffness and k is the spin-wave wavevector.

A connection between the frequency-swept linewidth and the field-swept linewidth is provided in [3.38] and can be deduced by differentiation of Equation (3.1) with respect to the external field value:

$$\Delta f = \frac{\gamma}{2\pi}\Delta H\sqrt{1+\left(\frac{\gamma M}{f}\right)^2} \tag{3.2}$$

where ΔH takes the following form when a Lorentzian lineshape is assumed in the frequency domain:

$$\Delta H = \Delta H_i + \frac{2}{\sqrt{3}}\frac{2\pi f}{\gamma}\alpha \tag{3.3}$$

ΔH_i includes the contribution from inhomogenous broadening. The connection between the decay time τ and Δf is given by the equation:

$$\Delta f = \frac{1}{\pi\tau}. \tag{3.4}$$

When the precession occurs around the out-of-plane magnetic field, the frequency/field linewidth relationship can be written as:

$$\Delta f_\perp = \frac{\gamma}{2\pi}\Delta H_\perp \tag{3.5}$$

where $\Delta H_\perp$ is the perpendicular linewidth and is frequency independent.

We can now convert the measured decay times into equivalent magnetic field linewidth values that are often used in FMR spectroscopy for determination of intrinsic

damping and inhomogeneous broadening. The result for a few measured frequencies is plotted in Figure 3.6b for the primary mode precession around the effective magnetic field direction. From the linear dependence of the converted ΔH values versus frequency and equation (3), we obtain ΔH_i=16 Oe and a linear slope of 2.85 Oe/GHz. We find reasonable agreement (16 % smaller linear slope and 2x larger ΔH_i) between our results and prior data [3.39] obtained using FMR and a Fe/GaAs (110) sample with 20 nm thickness.

The short optical penetration depths in metals can be used to reveal the presence of spin-wave modes dominated by exchange interaction by performing wavelength dependent studies with the three-color capabilities of the apparatus described here. The optical penetration depth ξ is wavelength dependent and is calculated using $\xi = \lambda/4\pi k$, where λ is the optical wavelength and k is the known imaginary part of the index of refraction [3.26,3.27]. At the probing wavelengths of 780 and 520 nm and according to [3.26], the corresponding ξ are 19 and 14 nm, respectively. The small optical penetration depth sensitivity to surface dominated spin dynamics is already well known from Brillouin light scattering (BLS) studies [3.40] of Damon-Eshbach (DE) dipolar surface modes [3.41]. To test the possibility of DE mode detection in our experiment, we compare 780 nm with 520 nm probing in Figure 3.6(c) keeping all the other experimental conditions unchanged. It is observed that the oscillation frequency and phase remain the same when probing at both wavelengths. This shows that the observed dynamics is not associated with propagating dipolar surface modes of Damon-Eshbach (DE) type, which is accompanied by frequency shift observations related to the incident photon wavevector changes in BLS measurements [3.42]. Moreover, insensitivity to DE modes is not unexpected considering that BLS detection of such modes is made in backscattering geometry [3.40] with enough transit time for the spin waves to propagate in and out of the probing region, while both conditions are not being met in our experiment. For our experiments, it is rather expected that detection of non-propagating spin-wave modes is a possibility. These are dominated by the exchange interaction in the presence of surface anisotropy [3.43]. Non-homogenous spin dynamics with a spatially dependent profile perpendicular to the sample surface is characteristic for such modes. When using the ASOPS system, the relative mode intensities measured at the 780 and 520 nm

wavelengths could be employed to test the model assumptions about the spin-wave mode spatial profile and identify strong surface contributions. For instance, we would expect that a confined surface mode can be more easily identified when comparing 780 nm with 520 nm probing, due to the different depth sensitivity. A full MOKE spectrum covering both wavelengths is not available for our particular sample, although we have normalized the data to the relative MOKE strength for bulk Fe [3.44]. After the normalization, it is observed (see Figure 3.6(c)) that the oscillation amplitude is very similar for both probing wavelengths, i.e., a uniform spin precession takes place with Eq. (3.1) being satisfied.

The detection techniques presently described can be extended to the measurement of the standing spin-wave modes that we observed in thicker Fe films using ASOPS time-delay scanning [3.34], or to new studies of nanostructured magnetic samples [3.45], as well as, the interlayer exchange coupling in multilayered magnetic thin films [3.46].

3.6 Pump-Probe on Opposite Sides of the Film

Additional ASOPS studies were performed to complement the experimental approach described Sections 3.3-3.5. By using a transparent substrate of MgO (100), we are able to modify the geometry of the experiment so that the pump beam can be focused and overlapped with the probe on the opposite sides of the epitaxial Fe films. In these experiments, we keep the probe beam focused through the MgO substrate and incident on the Fe/MgO interface.

Figure 3.7 shows the short timescales of the TTR signal recorded on the Fe films with variable thickness when the pump excitation is applied either on the same (Figure 3.7 a)) or on the opposite side of the film (Figure 3.7 b)). We observe a small negative dip in the TTR signals near the time zero of pump laser excitation and a fast raise to the maximum TTR amplitude in about 0.8 ps. The two peaks that have opposite signs in the TTR signals represent the electronic (negative TTR signal dip) and the lattice thermalization (positive TTR signal raise) within the two temperature model (see equations 2.2 and 2.6). What is seen in these data is that the initially hot electrons

(negative TTR signal dip) thermalize with the lattice (positive TTR signal raise) on a timescale of 0.8 ps.

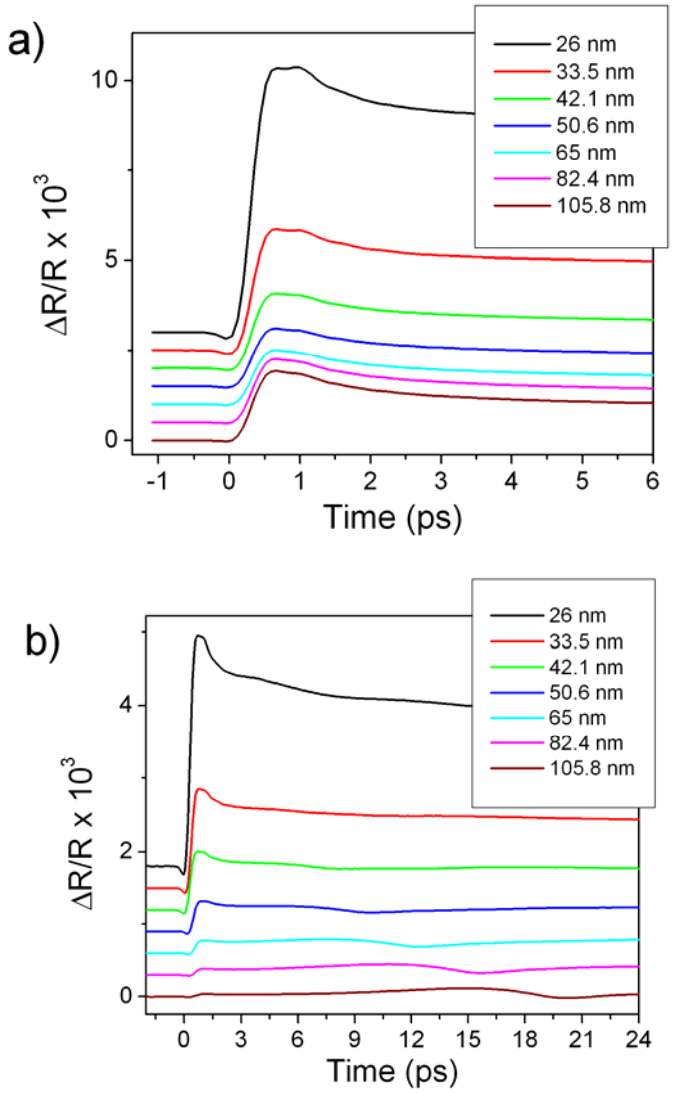

Figure 3.7 Transient reflectivity recorded on the same (a) and opposite b) side of the film with respect to the pump excitation, showing the short timescales of electronic and lattice excitation in epitaxial Fe films on MgO (100). Small negative dip at 0 ps is of electronic origin, and the large maximum at ~ 0.8 ps is the peak lattice temperature.

This behavior is already known from the studies in a thin Fe film (8 nm) deposited also on MgO (100) substrate and reported recently [3.47]. The novelty of our experiment is

that we can perform the opposite side probing of the propagation of thermal excitations as will be discussed in the following.

In Figure 3.8, we show the thickness dependency of the extinction depth for the electronic excitation (negative TTR signal dip). It is seen that the thickness dependency of the corresponding TTR amplitudes follows and exponential decay with a characteristic decay length of δ=22.3 nm. δ value is very close to the measured optical penetration depth at the pump laser wavelength reported in [3.25, 3.26]. This result shows directly that the non-equilibrium electronic excitation does not travel deep inside the Fe film, but is rather quickly thermalized with the lattice and does not propagate much during the short timescale of the experiment (< 0.8 ps). This result is in agreement to the analysis from [3.47].

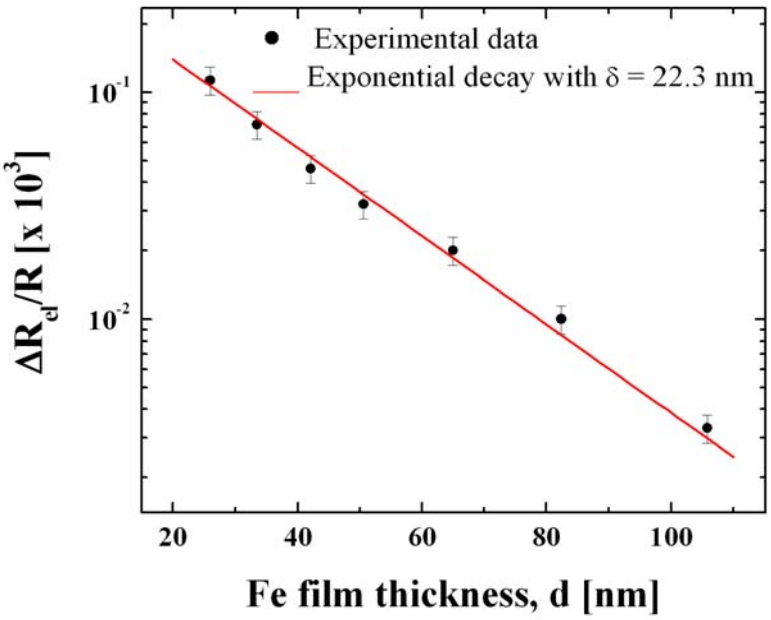

Figure 3.8 The attenuation of the electronic contribution to transient reflectivity (negative dip near 0 ps from Figure 3.7 b). The solid red line is a fit using an exponential decay.

In Figure 3.9, we show the probing of the uniaxial coherent strain pulses [3.29] that can be used to measure the film thickness based on the simple relationship: $\tau v = d$, where τ is the strain pulse arrival time, v is the longitudinal speed of sound along the

<001> direction of Fe, and *d* is the film thickness. We note the bipolar shape of the strain pulses that resemble nicely the calculations of the Thomsen's model [3.29] (see also equation (2.16)).

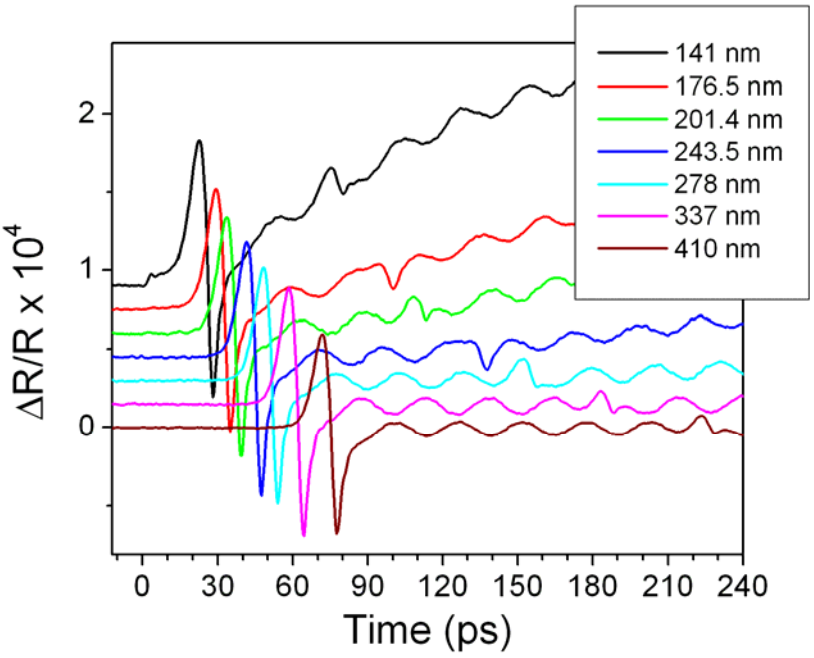

Figure 3.9 Transient reflectivity recorded on the opposite side of the film from the pump excitation showing the propagation of coherent strain pulses. The thickness dependence of the strain pulses arrival times is used for determining the Fe film thickness.

The coherent strain pulses will be further used in the experimental work of this thesis for estimating the film thickness. As it will be shown in Section 4.3, the dispersion relations of coherent spin waves return values in very good agreement with literature data for the exchange stiffness parameter in Fe, based on the values of the film thickness determination from the coherent strain pulses. Therefore, the film thickness determination from the data presented in Figure 3.9 is self-consistent with the other properties (such as magnetic) of the films under investigation.

Finally, in the Figures 3.10 and 3.11 are represented the diffusive heat transport and the corresponding travel times, τ, across thicker Fe films. The thermal diffusivity peak is marked with arrows in Figure 3.10 and 0.98 of its amplitude provides τ. The data

show simple scaling with the expected Fourier heat flow (see Sections 2.1 and 2.2), and can be used to estimate the thermal diffusivity of the Fe films (see Figure 3.11).

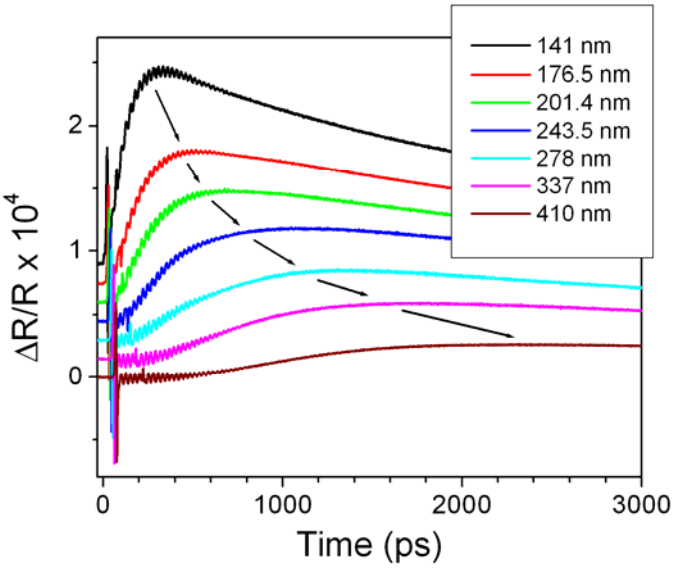

Figure 3.10 Heat diffusion in Fe/MgO(100) films probed in transient reflectivity on the opposite side of the film with respect to pump excitation. The arrow marks the evolution of the maximum temperature peak that corresponds to the time needed to reach the temperature uniformity across the film thickness.

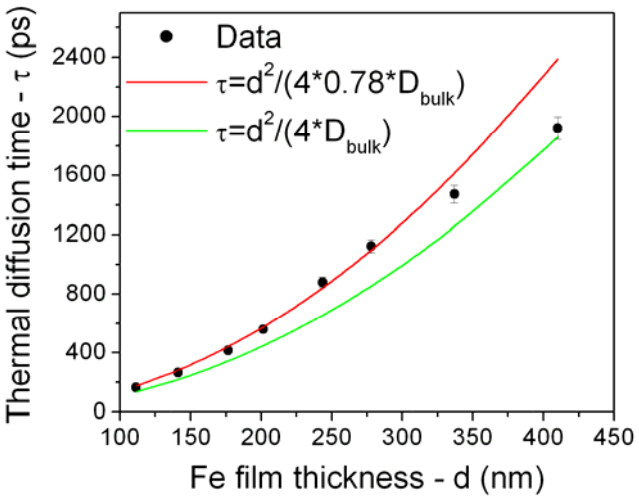

Figure 3.11 The heat diffusion arrival times (black dots) resulted from the transient reflectivity amplitudes (0.98% of the peak from Fig 3.10) as a function of Fe/MgO (100) film thickness. Red and green solid lines show the estimated times as seen in the inset. The dependence of the arrival time, τ, on the film thickness, d, knowing the thermal diffusivity of Fe, D_{bulk}, is also shown.

It was found that thinner films have an apparently reduced thermal diffusivity coefficient (0.78 of the known bulk value of 0.226 cm^2/s), whereas thicker films recover the bulk thermal diffusivity value.

3.7 Synchrotron Picosecond X-ray Diffraction: Direct Probe of Laser-Induced Lattice Dynamics in Ferromagnetic Thin Films

The availability of pulsed X-ray sources with ~ 100 ps in duration at national synchrotron facilities have paved the way for the development of time-resolved X-ray diffraction (TR-XRD) techniques for studies of lattice dynamics excited with femtosecond optical pulses in semiconductors [3.48-51]. These techniques provide access to *quantitative* studies of laser-induced lattice excitations in materials. Recently, the femtosecond optical pump combined with TR-XRD probing was used for studies of thermal transport in semiconductor films and multilayers [3.52-53]. Our aim is to extend the use of these techniques to the case of epitaxial Fe films for studies of thermal transport and of the coupling between magnetic and lattice excitations.

In this section, we provide a short description of an experimental arrangement used for TR-XRD probing of femtosecond laser-induced thermo-elastic transients in epitaxial Fe films. The experiments were carried out at the MHATT-XOR sector 7 beamline at the Advanced Photon Source. The main components of the experimental TR-XRD setup were previously described in [3.52-53]. Several adjustments were made to facilitate the measurement of epitaxial Fe films, including the use of a focused laser spot size of ~ 1.2 mm and theta-two-theta (θ-2θ) standard geometry for probing of the out-of-plane symmetric Bragg reflection [3.54]. In some of the measurements, an external magnetic field of a few hundred Oe, was applied parallel to the sample surface and at variable angle with respect to the in-plane crystallographic directions of the Fe films. The application of the magnetic field was made using a pair of permanent magnets that were placed on an automated rotation stage. This rotation stage allowed the rotation of the magnetic field direction around the perpendicular direction to the sample surface without perturbing the sample alignment.

In our initial measurements, a Au(4nm)/Fe(100nm)/Ge(110) sample was used, similar to the one already described in Section 3.3. The laser induced shift of the θ-2θ curve corresponding to a 200 ps X-ray pulse delay time and maximum amplitude of strain of ~ 0.14% is shown in Fig. 3.12.

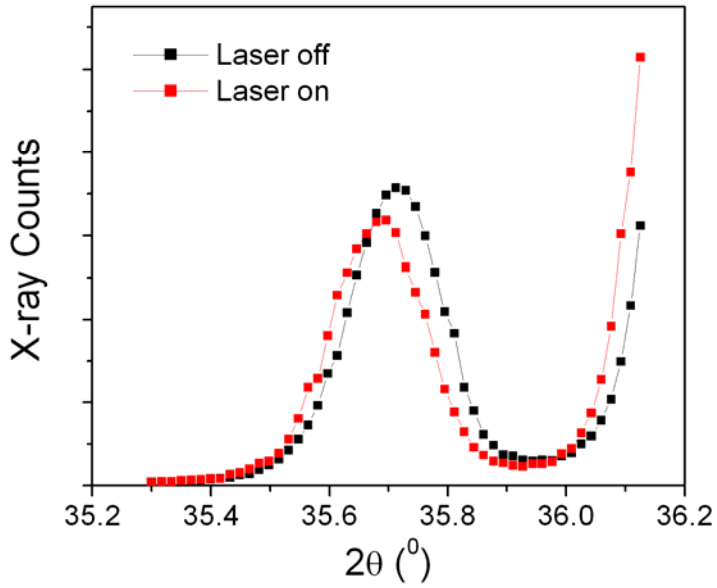

Figure 3.12 X-ray diffraction intensities for Au(4nm)/Fe(100nm)/Ge(110) at 100 ps after pump laser excitation with (red) and without (black) laser excitation.

The transient lattice cooling in Fe is monitored as a function of time delay following the initial laser excitation with the laser turned on (LTO), while the corresponding reference θ-2θ curves versus delay time with laser switched off (LSO) were also recorded. The laser-induced θ-2θ shifts can then be obtained from the difference between LTO and LSO as a function of time delay. Fig. 3.13 shows an example of a TR-XRD intensity map of the measured diffracted intensity versus the 2θ angle and time delay. After the onset of laser excitation, the Bragg peak is shifted abruptly to lower 2θ angles on the timescale of the X-ray pulse duration, followed by a gradual relaxation on the ns timescale. This trend is qualitatively similar to the all-optical TTR measurements described in Section 3.3, one exception being the reduced temporal resolution (~ 150 ps) for the case of TR-XRD measurements.

The quantitative determination of laser-induced thermo-elastic strains is problematic in the Au(4nm)/Fe(100nm)/Ge(110) sample due to the angular (θ) overlap between the (110) reflection of Fe and the tail of the Ge (220) substrate peak (see the asymmetry of the θ-2θ curves in Fig. 3.12).

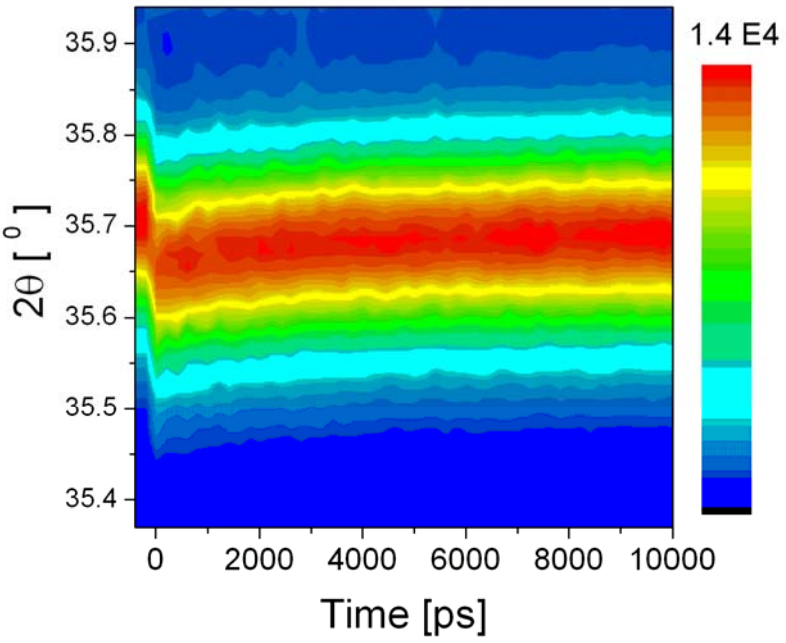

Figure 3.13 X-ray diffraction intensity map as a function of time delay after laser excitation for Au(4nm)/Fe(100nm)/Ge(110) sample.

To circumvent this, and to evaluate the laser-induced thermo-elastic strain, the LTO and LSO patterns have to be compared to determine the diffraction line displacement. The line displacement was determined by minimizing the sum of squared differences between LTO and the shifted LSO pattern:

$$\sum_{l}\left[I_{off}\left(\theta_i\right)-\alpha\, I_{on}\left(\theta_i+\Delta\theta_i\left(\varepsilon_l,\beta\right)\right)\right]^2 \rightarrow \min \tag{3.6}$$

The intensities (I_{on}, I_{off}) were calculated by using a B-spline interpolation from the original discrete patterns. Each individual shift was calculated by taking into account the overall displacement of the line due to the lattice strain, ε_l, as well as a scaling coefficient, β, which accounts for the non-uniform-strain induced peak broadening:

$$\Delta\theta_i = -\varepsilon_l \times \tan\left(\theta_{peak}\right)+\left(\beta-1\right)\times\left(\theta_i-\theta_{peak}\right) \tag{3.7}$$

Finally, the adjustable parameter α accounted for the change in peak intensity due to the Debye-Waller factor. The overall error in the strain evaluation was estimated by applying the same procedure for different patterns measured with LSO. The standard deviation of the apparent strain values obtained by this method corresponds to about 2×10^{-5}, which can be considered as a good estimation for the random strain error. After extracting the time dependence of the strain relaxation using the procedure described above, we could compare the result of TR-XRD with TTR measurements and obtain a fit with the procedure described in Section 3.3 on the same sample. The result of comparison is shown in Fig. 3.14, where the TR-XRD and TTR curve overlap nicely after renormalizing the TTR signal with an arbitrary scale factor.

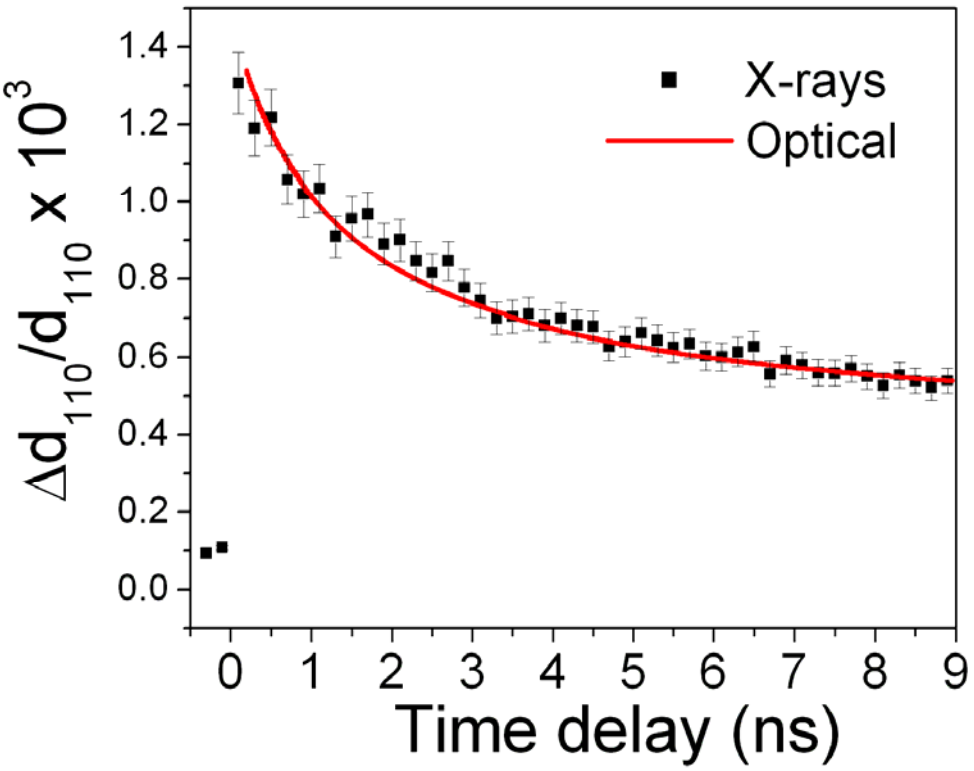

Figure 3.14 Laser-induced Bragg peak shift (black dots) versus time delay after laser excitation for Au(4nm)/Fe(100nm)/Ge(110) sample obtained from Fig. 3.13 and the procedure described in text. Red curve is the result of fit for TTR data on the same sample and is rescaled for comparison.

In consequence, this agreement provides support for the simple model of thermal transport at the Fe/Ge interface, described in sections 2.1 and 3.3. Unfortunately, an attempt to pursue a more systematic investigation of thermo-elastic relaxation in Fe/Ge samples, which extends to thinner Fe layers, did not succeed. The basic reason is that a high temperature post-deposition annealing is needed (~ 300-400 ^{0}C) to obtain narrow X-ray diffraction peaks of Fe for accurate TR-XRD studies, which is impeded by severe intermixing at the Fe/Ge interface at these high annealing temperatures.

To overcome the problems discussed in the above, another set of epitaxial Fe samples were grown on MgO (100) substrates, which feature an inert film-substrate interface; this could be annealed to higher temperatures (up to 400 ^{0}C). The Fe films deposited on MgO substrates grow according to the well-known Fe(100)<110> || MgO(100)<100> (45^o in-plane rotation) epitaxial relationship that minimizes the Fe-MgO lattice mismatch [3.55]. An important consequence of this epitaxial relationship is that the out-of-plane (200) Bragg reflection of Fe (used in TR-XRD studies) is well separated from all of the MgO substrate Bragg reflections in the θ-2θ scans. Figs. 3.14 a) and b) show the experimental data for the laser-induced transient Bragg peak shift recorded at a time delay of 100 ps after the laser excitation.

To test whether the TR-XRD measurements are a linear function of the excitation power in samples with different Fe film thickness, we have performed measurements of the laser power dependence of the Bragg peak shift at a fixed time delay of 100 ps after the laser excitation, where the shifts have maximum amplitudes. The experimental result of this power dependence is shown in Fig. 3.15, which confirms a linear relationship between the laser excitation power and the observed Bragg peak shifts.

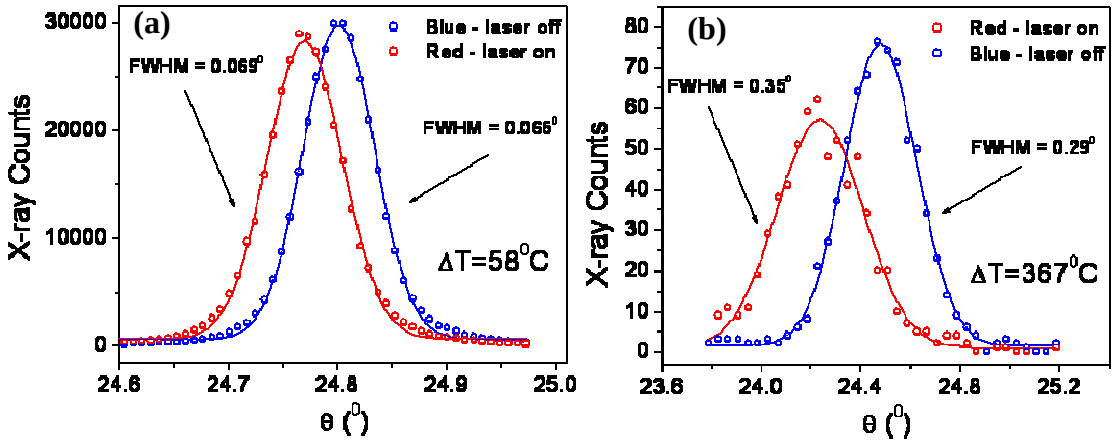

Figure 3.15 Laser-induced shifts for two thicknesses of epitaxial Fe: a) Au(4 nm)/Fe(101nm)/MgO(100), and b) Au(4 nm)/Fe(11nm)/MgO(100).

Moreover, we can compare the measured Bragg peak shifts with the expected shifts derived from Thomsen's model of thermo-elastic strain generation (see Ref. [3.29, 3.56]). Within the Thomsen's model, the laser-induced temperature raise for a film heated uniformly is given by (see Eqn. [11] from Ref. [3.56]):

$$\Delta T = \frac{(1-R)Q}{\pi w^2 C d} e^{-\frac{r^2}{w^2}} \tag{3.8}$$

where R is the sample reflectivity, Q is the incident laser pulse energy, C is the sample specific heat, d is the film thickness, r is the radial distance from the laser spot center on the sample, and w is the characteristic lateral spot size dimension. Moreover, if the lateral spot laser dimension is much larger than the sample thickness then the thermal expansion occurs out-of-plane only and the corresponding uniaxial thermo-elastic strain (or out-of-plane strain, ε) can be written as:

$$\varepsilon = \beta \Delta T \frac{1+\nu}{1-\nu} \tag{3.9}$$

where β is the linear thermal expansion coefficient and ν is the Poisson's ratio.

In our experiments on Au/Fe/MgO(100) films, w = 610 μm for the incident laser beam on the sample, 1-R=0.35 and the angle between the sample plane and laser beam direction is about 40^0. We take for example, the particular case of Fe film thickness,

d=105 nm (this includes the Au cap layer thickness in the total bilayer thickness for simplicity), from Fig. 3.15 at an excitation power of 524 mW and the laser excitation frequency of 5 kHz. We then estimate using Eqn. (3.8), assuming bulk values for the specific heat and Poisson ratio of Fe, that the laser-induced temperature change is: $\Delta T_{estimated}$ = 54 K. The measured laser-induced temperature change obtained from Eqn. (3.9) is: $\Delta T_{measured}$ = 50 K, which is in good agreement with the above estimation, validating the use Eqns. (3.8) and (3.9) in estimating the laser-induced ΔT.

Next, we show the experimental result of transient thermo-elastic relaxation as a function of Fe layer thickness in Fig. 3.16. We have used the same thermal transport model as in section 3.3 to fit the experimental data (also shown in Fig. 3.16). In the fitting procedure we have fixed the heat penetration depth at δ=25 nm, and the film thermal diffusivity at 0.18 cm^2/s, consistent with the data from Fig. 3.11. We then allowed the thermal boundary conductance, σ_k, and MgO substrate thermal diffusivity, D_s, to vary and searched for values that give the best match between the model and the experimental data.

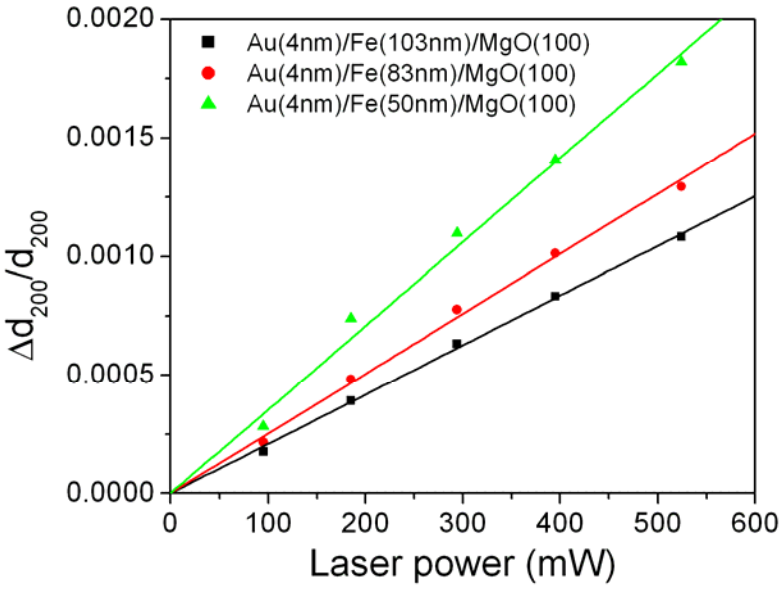

Figure 3.16 Laser power dependency of the Bragg peak shift (dots) for the samples shown in inset. Lines are linear fit to the data.

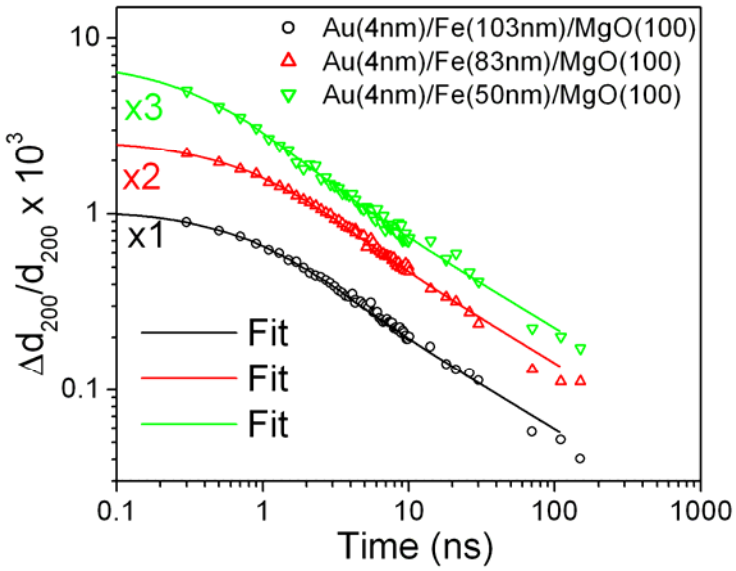

Figure 3.17 Experimental (dots) Bragg peak shits for the sample shown in inset. Lines are fits using the procedure described in text.

A good match to the data is obtained for Fe film thicknesses of 50, 83 and 101 nm, when σ_k is equal to 4.3×10^8, 3×10^8 and 3.6×10^8 W/m^{2}K, respectively. Simultaneously, for these same Fe film thicknesses, the values of D_s extracted from fitting the experimental data are equal to 0.12, 0.1 and 0.13 cm^2/s, respectively. We estimate an uncertainty of 20% in the determination of σ_k and D_s in these experiments, which show that the determination of D_s falls close to the bulk value of ~ 0.13 cm^2/s, whereas the variations of σ_k are scattered outside the estimated error. We believe, that the large variations of σ_k between different samples is related to local details of the mechanical polishing of the substrate, which could not removed before Fe film deposition.

More studies which include MgO surface characterization prior to Fe film deposition will be needed in the future to elucidate this behavior. On the other hand, additional studies of TTR on the same samples which have looked at different regions along the sample surface, have revealed variations in the thermal cooling rate in qualitative support to the TR-XRD findings. What is already clear from the combined TR-XRD and TTR studies so far is that the former technique provides improved sensitivity for measurements of

thermal transport and can simultaneously determine σ_k and D_s, which was not possible from TTR alone since that provided only an estimate for σ_k. Moreover, with these studies we can confirm that that the simple model from section 3.3 can account for thermal relaxation up to 100 ns after excitation, whereas good estimates for laser-induced strain amplitudes are obtained from Eqns. (3.8) and (3.9).

REFERENCES FOR CHAPTER 3

3.1 R. A. Lukaszew, Z. Zhang, V. Stoica and R. Clarke, AIP Conf. Proc. 696, 629 (2003).

3.2 R. A. Lukaszew. Z. Zhang, C. Cionca, V. Stoica and R. Clarke, J. Vac. Sci. Technol. A 21, 1524 (2003).

3.3 R. A. Lukaszew, Z. Zhang, V. Stoica and R. Clarke, Appl. Surf. Science 219/1-2, 74-79 (2003).

3.4 R. A. Lukaszew, B. McNaughton, V. Stoica and R. Clarke, MRS Proceedings 696, N3.29, (2002).

3.5 B. Perrin, "Investigation of short-time heat transfer effects by an optical pump-probe method," in Microscale and Nanoscale Heat Transfer, Topics in Applied Physics, S. Voltz, ed. (Springer, Berlin, 2007), Vol. 107, pp. 333–359.

3.6 P. A. Elzinga, F. E. Lytle, Y. Jiang, G. B. King, and N. M. Laurendeau, ″Pump probe spectroscopy by asynchronous optical-sampling,″ Appl. Spectrosc. 41, 2-4 (1987).

3.7 G. A. Antonelli, B. Perrin, B. C. Daly, and D. G. Cahill, ″Characterization of mechanical and thermal properties using ultrafast optical metrology,″ MRS Bull. 31, 607-613 (2006).

3.8 R. Merlin, ″Generating coherent THz phonons with light pulses,″ Solid-State Commun. 102, 207-220 (1997).

3.9 W. S. Capinski and H. J. Maris, ″Improved Apparatus for Picosecond Pump-and-Probe Optical Measurements,″ Rev. Sci. Instrum. 67, 2720-2726 (1996).

3.10 E. Lill, S. Schneider, and F. Dorr, ″Rapid optical sampling of relaxation-phenomena employing two time-correlated picosecond pulse trains,″ Appl. Phys. 14, 399-401 (1977).

3.11 W. T. Barnes, Jr., ″Modulated gain spectroscopy, ″ Ph.D. Dissertation, Purdue University, West Lafayette, Indiana (1980).

3.12 A. F. Bartels, F. Hudert, C. Janke, T. Dekorsy, and K. Kohler, ″Femtosecond time-resolved optical pump-probe spectroscopy at kilohertz-scan-rates over nanosecond-time-delays without mechanical delay line,″ Appl. Phys. Lett. 88, 041117 (2006).

3.13 http://www.menlosystems.com

3.14 S. Adachi, S. Takeyama, and Y. Takagi, ″Dual wavelength optical sampling technique for ultrafast transient bleaching spectroscopy,″ Opt. Commun. 117, 71-77 (1995).

3.15 J. S. Lannin, J. M. Calleja, and M. Cardona, ″Second-order Raman scattering in the group-Vb semimetals: Bi, Sb, and As,″ Phys. Rev. B 12, 585-593 (1975).

3.16 G. A. Garrett, T. F. Albrecht, J. F. Whitaker, and R. Merlin, "Coherent THz phonons driven by light pulses and the Sb problem: What is the mechanism?," Phys. Rev. Lett. 77, 3661 (1996).

3.17 R.J. Stevens, A.N. Smith, and P.M. Norris, "Signal analysis and characterization of experimental setup for the transient thermoreflectance technique," Rev. Sci. Instrum. 77, 084901 (2006).

3.18 K. Postava, H. Jaffres, A. Schuhl, F. Nguyen Van Dau, M. Goiran, and A. R. Fert, ″Linear and quadratic magneto-optical measurements of the spin reorientation in epitaxial Fe films on MgO,″ J. Magn. Magn. Mater. 172, 199-208 (1997).

3.19 J. Zak, E. R. Moog, C. Liu, and S. D. Bader, "Magneto-optics of multilayers with arbitrary magnetization directions," Phys. Rev. B 43, 6423 (1991).

3.20 G. C. Cho, W. Kütt, and H. Kurz, ″Subpicosecond time-resolved coherent-phonon oscillations in GaAs,″ Phys. Rev. Lett. 65, 764-766 (1990).

3.21 M. I. Kaganov, I. M. Lifshitz, and L. V. Tanatarov, ″Relaxation between electrons and the crystalline lattice,″ Sov. Phys. JETP 4, 173-180 (1957).

3.22 R.J. Stevens, A.N. Smith, and P.M. Norris, ″Measurement of thermal boundary conductance of a series of metal-dielectric interfaces by the transient thermoreflectance technique,″ J. Heat Transfer 127, 315-322 (2005).

3.23 The heat diffusion model (equations 2-7 from [15]) can be applied if the time constant of heat diffusion in film (τ_f) and interface time constant (τ_i) follows $\tau_f/\tau_i = d\,\sigma_k / k_f < 1$ (equation 10 from [15]), where d is the film thickness. If $\sigma_k \sim 108$ to 109 W/m2K and k_f is from few tens to few hundreds W/Km then d should be < 100 nm, which verifies that d for our samples (70 nm) satisfies this criterion.

3.24 E. G. Gamaly, A. V. Rode, and B. Luther-Davies, "Ultrafast ablation with high-pulse-rate lasers. Part I: Theoretical considerations," J. Appl. Phys. 85, 4213 (1999).

3.25 C. A. Paddock and G. L. Eesley, ″Transient thermoreflectance from thin metal-films.″ J. Appl. Phys. 60, 285-290 (1986).

3.26 P. B. Johnson and R. W. Christy, "Optical constants of transition metals: Ti, V, Cr, Mn, Fe, Co, Ni, and Pd," Phys. Rev. B 9, 5056-5070 (1974).

3.27 M. A. Ordal, R. J. Bell, R. W. Alexander, L. L. Long, and M. R. Querry, "Optical properties of fourteen metals in the infrared and far infrared: Al, Co, Cu, Au, Fe, Pb, Mo, Ni, Pd, Pt, Ag, Ti, V, and W," Appl. Opt. 24, 4493-4499 (1985).

3.28 R. J. Stoner, and H. J. Maris, ″Kapitza conductance and heat-flow beween solids at temperatures from 50 to 300 K,″ Phys. Rev. B 48, 16373-16387 (1993).

3.29 C. Thomsen, H. T. Grahn, H. J. Maris, and J. Tauc, ″Surface generation and detection of phonons by picosecond light-pulses,″ Phys. Rev. B 34, 4129-4138 (1986).

3.30 J. K. Miller, J. Qi, Y. Xu, Y.-J. Cho, X. Liu, J. K. Furdyna, I. Perakis, T. V. Shahbazyan, and N. Tolk, ″Near-bandgap wavelength dependence of long-lived traveling coherent longitudinal acoustic phonons in GaSb-GaAs heterostructures,″ Phys. Rev. B 74, 113313 (2006).

3.31 D. E. Aspnes and A. A. Studna, ″Dielectric functions and optical parameters of Si, Ge, GaP, GaAs, GaSb, InP, InAs, and InSb from 1.5 to 6.0 eV,″ Phys. Rev. B 27, 985-1009 (1983).

3.32 H. J. McSkimin, ″Measurement of elastic constants at low temperatures by means of ultrasonic waves - data for silicon and germanium single crystals, and for fused silica,″ J. Appl. Phys. 24, 988-997 (1953).

3.33 G. Ju, A. V. Nurmikko, R. F. C. Farrow, R. F. Marks, M. J. Carey, and B. A. Gurney, ″Ultrafast time resolved photoinduced magnetization rotation in a ferromagnetic/antiferromagnetic exchange coupled system,″ Phys. Rev. Lett. 82, 3705-3708 (1999).

3.34 M. van Kampen, C. Jozsa, J. T. Kohlhepp, P. LeClair, L. Lagae, W. J. M.de Jonge, and B. Koopmans, ″All-optical probe of coherent spin waves,″ Phys. Rev. Lett. 88, 227201 (2002).

3.35 V. A. Stoica, R. Merlin, R. A. Lukaszew, and R. Clarke, "Time-resolved spin dynamics studies of ferromagnetic thin films grown by molecular beam epitaxy," presented at APS March Meeting, Los Angeles, CA, USA, 21-25 March 2005.

3.36 F. Schreiber, J. Pflaum, Z. Frait, Th. Muhge, and J. Pelzl, ″Gilbert damping and g-factor in FexCo1-x alloy films,″ Solid-State Commun. 93, 965-968 (1995).

3.37 M. Farle, ″Ferromagnetic resonance of ultrathin metallic layers,″ Rep. Prog. Phys. 61, 755-826 (1998).

3.38 S. S. Kalarickal, P. Krivosik, M. Z. Wu, C. E. Patton, M. L. Schneider, P. Kabos, T. J. Silva, J. P. Nibarger, ″Ferromagnetic resonance linewidth in metallic thin films: Comparison of measurement methods,″ J. Appl. Phys. 99, 093909 (2006).

3.39 J. J. Krebs, F. J. Rachford, P. Lubitz, and G. A. Prinz, ″Ferromagnetic resonance studies of very thin epitaxial single-crystals of iron,″ J. Appl. Phys. 53, 8058-8060 (1982).

3.40 J. R. Sandercock and W. Wettling, ″Light scattering from thermal magnons in iron and nickel,″ IEEE Trans. Magn. 14, 442-444 (1978).

3.41 R. W. Damon and J. R. Eshbach, ″Magnetostatic modes of a ferromagnetic slab,″ J. Phys. Chem. Solids 19, 308-320 (1961).

3.42 M. Madami, S. Tacchi, G. Carlotti, G. Gubbiotti, and R. L. Stamps, ″In situ Brillouin scattering study of the thickness dependence of magnetic anisotropy in uncovered and Cu-covered Fe/GaAs(100) ultrathin films,″ Phys. Rev. B 69, 144408 (2004).

3.43 H. Puszkarski, ″Theory of surface states in spin wave resonance,″ Prog. Surf. Sci. 9, 191-247 (1979).

3.44 G. S. Krinchik and V. A. Artem'ev, ″Magneto-optical properties of Ni, Co and Fe in ultraviolet visible and infrared parts of spectrum,″ Sov. Phys. JETP 26, 1080-1085 (1968).

3.45 A. Barman, S. Wang, J. Maas, A. R. Hawkins, S. Kwon, J. Bokor, A. Liddle, H. Schmidt, ″Size dependent damping in picosecond dynamics of single nanomagnets,″ Appl. Phys. Lett. 90, 202504 (2007).

3.46 P. Grünberg, R. Schreiber, Y. Pang, M. B. Brodsky, and H. Sowers, ″Layered Magnetic Structures: Evidence for Antiferromagnetic Coupling of Fe Layers across Cr Interlayers,″ Phys. Rev. Lett. 57, 2442-2445 (1986).

3.47 E. Carpene, E. Mancini, C. Dallera, M. Brenna, E. Puppin, and S. de Silvestri, Phys. Rev. B 78, 174422 (2008).

3.48 A. M. Lindenberg, I. Kang, S. L. Johnson, T. Missalla, P. A. Heimann, Z. Chang, J. Larsson, P. H. Bucksbaum, H. C. Kapteyn, H. A. Padmore, R. W. Lee, J. S. Wark, and R. W. Falcone, Phys. Rev. Lett. 84, 111 (2000).

3.49 D. A. Reis, M. F. DeCamp, P. H. Bucksbaum, R. Clarke, E. Dufresne, M. Hertlein, R. Falcone, H. Kapteyn, M. Murnane, J. Larsson, Th. Missalla, and J. Wark, Phys. Rev. Lett. 86, 3072 (2001).

3.50 M. F. DeCamp, D. A. Reis, P. H. Bucksbaum, B. Adams, J. M. Caraher, R. Clarke, C. W. S. Conove, E. M. Dufresne, R. Merlin, V. Stoica, and J. K. Wahlstrand, Nature (London) 413, 825 (2001).

3.51 M. F. DeCamp, D. A. Reis, D. M. Fritz, P. H. Bucksbaum, E. M. Durfresne, and R. Clarke, J. Synchrotron Radiat. 12, 177 (2005).

3.52 M. Highland, B. C. Gundrum, Y. K. Koh, R. S. Averback, D. G. Cahill, V. C. Elarde, J. J. Coleman, D. A. Walko, and E. C. Landahl, Phys. Rev. B 76, 075337 (2007).

3.53 Y. M. Sheu, S. H. Lee, J. K. Wahlstrand, D. A. Walko, E. C. Landahl, D. A. Arms, M. Reason, R. S. Goldman, and D. A. Reis, PRB 78, 045317 (2008).

3.54 B. E. Warren, X-Ray Diffraction, New York: Dover (1990).

3.55 H. Fuke, A. Sawabe, and T. Mizoguchi, Japan. J. Appl. Phys. 32, L1137 (1993).

3.56 W. Singhsomroje and H. J. Maris, Phys. Rev. B 69, 174303 (2004).

CHAPTER 4

OPTICAL PULSE MAGNETOMETRY (OPM) USING FEMTOSECOND LASERS

At the nanoscale, and in the presence of surfaces and interfaces, the magnetic properties of ferromagnetic metals deviate strongly from the known behavior of their bulk constituents. An illustration of this situation is the intensely studied case of ferromagnetic epitaxial Fe films on semiconducting substrates such as GaAs [4.1]. Although these studies are spread over several decades, there is still a considerable amount of controversy relating to the complex nature of the interface arising from the strong chemical interaction between Fe and As [4.1]. Here we remove this complication by focusing on epitaxial films of Fe on Ge and MgO, chemically a much more inert system, while still retaining the interesting physics relating to the crystalline film-substrate interactions.

In this context, the aim of the work described in the present chapter is to develop ultrafast optical pump-probe methods for reliable measurements of the magnetic properties of thin films. Emphasis is placed on accessing the dynamics of the magnetization behavior so that unresolved issues, such as the role of the epitaxial magnetic interactions referred to above, can be addressed effectively. We refer to this approach as Optical Pulse Magnetometry (OPM).

Two major techniques for magnetometry, ferromagnetic resonance (FMR) and Brillouin light scattering (BLS), were already successfully applied for many decades. They are both performed in the frequency-domain, as contrasted with the time-domain approach (OPM) developed in the present work. Many authors already discussed the working principles of FMR and BLS and an abundant literature exists. For more detailed discussions see the comprehensive reviews in [4.2-4.4].

One of the most important findings of this dissertation work is our observation that detailed magnetic characterization can be pursued in the time-domain with the use of femtosecond lasers (see Chapter 3) via generation of gigahertz coherent spin waves. The underlying basis of this approach came about a decade ago, when the time-resolved magneto-optical Kerr effect (TR-MOKE) was used to observe the coherent spin dynamics excited by an ultrafast optical pulse in metallic films and nanostructures [4.5, 4.6]. This experimental capability was subsequently exploited by determining the magnetic anisotropy of epitaxial ferromagnetic Fe films [4.7, 4.8]. The data analysis relied on a formalism that was previously applied for explaining the FMR experiments [4.2] and largely ignored the details of the laser influence on the magnetic properties of the sample. This formalism was further developed here (see Section 2.3) to include the laser-induced modification of the magnetic anisotropy; this allows for a more realistic comparison between theory and experiment.

Recently, several authors, including our group, have reported experimental results on the time-resolved optical studies of coherent spin waves [4.9-4.15]. Subsequent experiments, reported here, demonstrate unequivocally that all-optical time domain techniques are capable of revealing new aspects of the physics that could not be accessed in frequency-domain techniques (FMR and BLS). Four novel results related to the coherent spin dynamics could be derived experimentally with the use of OPM. A detailed description of the experimental results is given in the sections that follow after the brief summary provided here.

In one experiment (see Section 4.1) we elucidate the direct versus indirect coupling of light to long-wavelength coherent spin waves. In a second experiment (see Section 4.2), it is shown that the time dependence of the laser-induced modification of the magnetic anisotropy can be determined quantitatively. A third experiment (see Section 4.3) provides evidence for the laser-driven electron-magnon interaction through studies of the laser modification of the exchange stiffness constant. A fourth experiment (see Section 4.4) uses time-frequency analysis to resolve the fine details of the propagating coherent spin waves in cross-plane geometry. Such experimental demonstrations make OPM a really useful method for advancing the field beyond just an incremental progress over the past studies.

4.1 Evaluating the Direct Coupling between Optical Excitation and Coherent Spin Wave Dynamics

There are two ways in which the laser can generate coherent spin-wave dynamics: a direct interaction which involves coupling to the photon field; and second, an indirect interaction mediated by electrons and/or phonons. In this section we provide some results of experiments which can determine the applicability of these two mechanisms in a given situation. One example is the case of coherent spin-wave generation. Here we show that one must include indirect coupling of the light through electron or phonon excitations in the description of the coherent spin wave dynamics.

In order to study the generation mechanism of coherent spin wave dynamics we prepared a sample in which an epitaxial Fe layer with uniform thickness (20 nm) is grown at room temperature using molecular beam epitaxy (MBE) deposition on single crystalline (001) MgO substrate. The film is further annealed at 350 ^{0}C for a few minutes to obtain a smooth Fe surface. After reducing the substrate temperature to ~ 100 ^{0}C, an additional epitaxial Au layer is grown on top of the Fe layer, controlling its thickness between 3 and 200 nm across a lateral wedge.

The experimental geometry of the optical pump-probe experiment is described in Section 3.3, where the pump beam irradiates either the Au surface or the Fe/MgO interface, while the probe beam detects the film temperature change and the coherent spin dynamics at the Fe/MgO interface. The aim is to distinguish the direct optical excitation process from the indirect (thermal) transport by spatially separating the regions in which these two processes can occur.

The principle of separating the optical field from the thermal excitations is based on the short optical penetration depth in Au of δ_{Au} ~ 12 nm. When the Au thickness is much smaller than δ_{Au}, the Fe layer can be excited optically, whereas when the Au thickness is much larger than δ_{Au}, the pump beam cannot excite the Fe layer optically, being completely absorbed near the Au surface. On the other hand, in the latter case, the

optical absorption creates a hot electron gas in the Au layer that propagates in the bulk and at large distances compared to δ_{Au}. The hot electron gas drifts throughout the Au layer with some attenuation and is transmitted inside the Fe layer where the thermal excitation of the coherent spin waves occurs. The efficiency of coherent spin wave excitation is then compared as function of the Au layer thickness for assessing the role of the direct optical excitation of the Fe layer.

In order to assess the strength of the thermal excitation at the Fe/MgO interface, the transient thermoreflectance (TTR) is used as described in Section 3.2 to measure the peak of the temperature change of the Fe layer as a function of the Au cap layer thickness (see Figure 4.1).

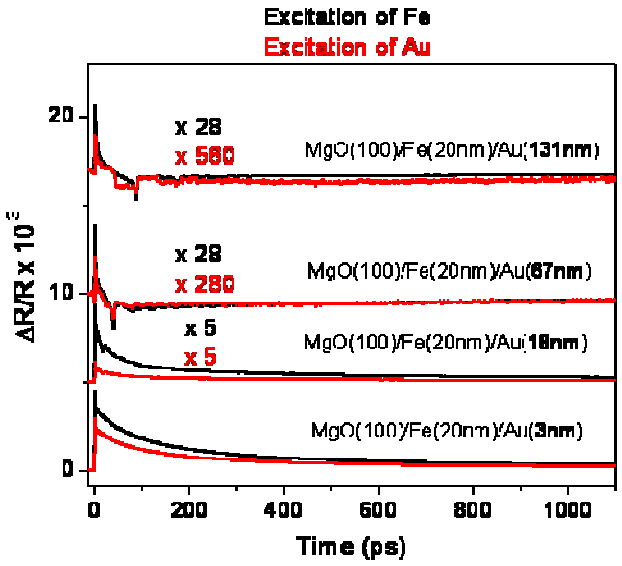

Figure 4.1 TTR spectra with pump at the Fe/MgO interface (black) and Au surface (red). Detection (probe) is performed at the Fe/MgO interface. The upper curves were scaled and displaced vertically for better visibility.

The sample is placed in an external magnetic field of ~ 500 Oe applied at a few degrees from the in-plane <110> Fe axis. The magnetic field has a negligible effect on the TTR signal. The pump and probe fluencies are fixed at 3 mJ/cm^2 and 0.4 mJ/ cm^2, respectively in all measurements. The corresponding maximum temperature change of the Fe layer is estimated to be 100 ^{0}C for the case of the Fe(20 nm)/Au(3 nm) sample, and much smaller for the samples with thick Au layers. This maximum transient

temperature estimation uses the procedure described in Section 3.2. Figure 4.2 shows a comparison of experimental data obtained with the pump beam both from the Fe/MgO side and from the Au surface side of the bilayer. For the case of Fe/MgO interface excitation (the black curves in Figure 4.1), it is seen that the maximum strength of TTR signal recorded at a time delay of ~ 1 ps decreases strongly and saturates at lower values for thicker Au layers. This is due to leaking of hot electrons from the Fe layer into the Au layer.

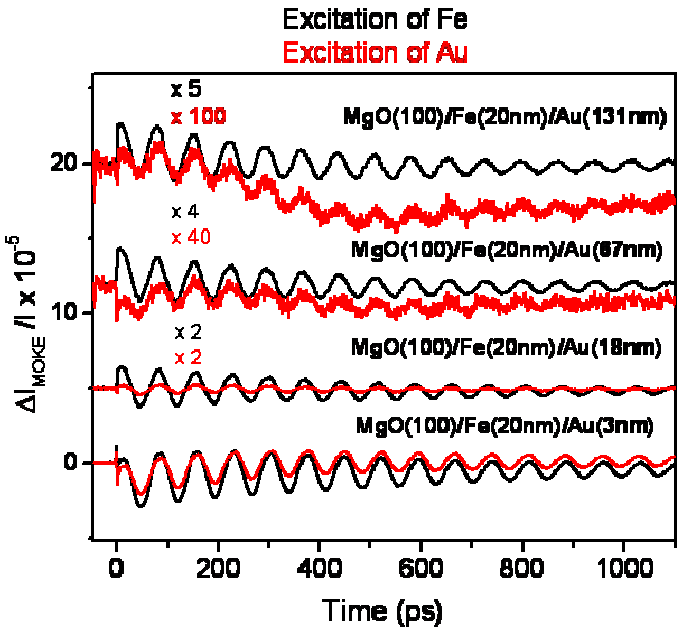

Figure 4.2 TR-MOKE spectra with pump at the Fe/MgO interface (black) and Au surface (red). Detection (probe) is performed at the Fe/MgO interface. The upper curves were scaled and displaced vertically for better visibility.

Here the Au-layer has a role of a heat sink for the hot electrons, meaning that when more electrons escape into the Au-layer then the maximum transient temperature in Fe is lower. This process is nonlinear and occurs on sub-ps timescale before the hot electron thermalization with the lattice (due to electron-phonon coupling) is completed at a time delay of ~ 1 ps. The red curves from Figure 4.1 show the TTR signal recorded in Fe layer when the bi-layer structure is excited via the optical irradiation of Au surface.

A similar trend is observed in the case of direct Fe excitation at the Fe/MgO interface. The TTR signal is strongly dependent on the Au thickness, although one important difference is the continuous decrease of the TTR signal with the increase of the Au layer. This means that not all the electrons excited in Au can be transferred to the Fe layer as the Au thickness is progressively increased. However, the electrons that arrive in the Fe layer deposit their energy to the lattice and thereby raise the Fe temperature. The quantitative description of the hot electron dynamics in Fe, Au and at the Fe/Au interface including bulk and interface contributions and subsequent thermalization with the lattice is a complex problem. While being interested only in distinguishing the efficiency of the coherent spin wave generation via an optical or thermal mechanism, the above difficulties can be eliminated through the following normalization procedure. The TTR signal (maximum transient reflectivity change) with pump excitation at the Au surface can be divided by the associated TTR signal when pump excitation occurs at the Fe/Au interface. This procedure eliminates the unknown details of the non-equilibrium processes and subsequent relaxation by measuring the relative efficiency of the thermal excitation of the Fe layer when the excitation is performed differently (direct or through the Au layer). The main result of the Au thickness variation is to suppress the direct optical excitation of the buried Fe layer when the Au layer is thick (this the case of 67 nm and 131 nm Au layers from Figure 4.1).

An important observation inferred from the set of data presented in Figure 4.1 is that when the Au layer thickness is increased from 3 nm to 131 nm, the corresponding TTR signal decreases by less than 3 orders of magnitude, whereas the optical penetration through the Au layer decreases by 5 orders of magnitude. This is evidence that at least for the 131 nm Au layer sample, and perhaps also for the 67 nm Au sample, we observe only the effects of the thermal excitation. Thus only the hot electrons from Au participate in the excitation process of Fe when the Au layer is thick. This means that the electrons from the Au layer are mediating the transfer of energy between the absorbed photons and the Fe layer. This process takes place via the hot electron propagation from Au and into the Fe layer where the electrons eventually thermalize with the Fe lattice. Thus we can definitively exclude the direct optical excitation mechanism of the Fe layer in this case.

Now we address the behavior of the spin wave dynamics by means of time-resolved MOKE (TR-MOKE) techniques (see Section 3.2). In Figure 4.2, the TR-MOKE data are shown which were collected in the same sample locations as those from Figure 4.1 with only the detector geometry being changed for recording the TR-MOKE signal. This signal is proportional to the magnetization vector rotation around the direction of the effective magnetic field (see Section 3.3). The coherent oscillations present in all experimental curves can be safely attributed to coherent spin dynamics due to their strong amplitude and frequency dependence on the magnetic field orientation and strength. To facilitate the comparison between Fe/Au bi-layers with different thicknesses, the magnetic field geometry is preserved for all samples. Similar to Figure 4.1, in Figure 4.2, the black curves are taken with the pump excitation at the Fe/MgO interface, and the red curves correspond to the pump excitation at the Au surface. The same trend in the variation of amplitude of the TR-MOKE oscillations as a function of the Au cap layer thickness is seen in the data from Figure 4.2 as in the case of the associated TRR amplitudes from Figure 4.1. Next, we follow the same procedure of data normalization as for the TRR curves. The ratio of the TR-MOKE coherent oscillation amplitudes with the pump on the Au surface side are divided by the TR-MOKE coherent oscillation amplitudes when pump excitation occurs at the Fe/Au interface. Then the resulting normalized amplitudes corresponding to TRR and TR-MOKE curves are plotted against each other, as shown in Figure 4.3.

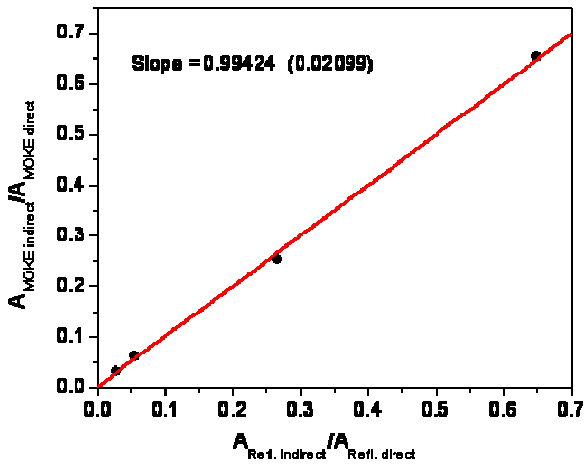

Figure 4.3 Cross correlation plot of TTR and TR-MOKE amplitudes obtained from Figs. 4.1-4.2.

In the linear fit to the experimental data from Figure 4.3, both the intercept and the slope were adjusted to their optimum values, although within the experimental uncertainty a line fit with a slope of 1 (one) and an intercept of 0 (zero) also fit the data very well. This means that the TTR and TR-MOKE amplitudes are highly correlated. On the other hand, it was already discussed in the above that the use of Au thick layers prevents the direct optical excitation of the Fe layer as opposed to the case of the thin Au layers. This provides an experimental proof that the direct coupling of optical excitation with the dynamics of coherent spin waves is very small or nonexistent and such a possibility can safely be ignored. It is rather the propagation of hot electrons from the Au layer and into the Fe layer that fully determines the coherent spin wave amplitudes. The coherent spin excitation is therefore the result of the heat deposition in the Fe layer.

In some other examples of optical excitation leading to magnetization changes the conclusions are not so clear cut. For instance, the earliest TR-MOKE studies using the femtosecond optical irradiation of Ni, ultrafast demagnetization (UD) was seen to occur on the fs timescale [4.17]. A multitude of microscopic mechanisms were used to explain these observations, which generated considerable controversies relating to their exact origin [4.18-4.25] the actual mechanism behind experimental observations is yet to be unambiguously determined. We will return later to the nature of UD in the context of optically induced switching (see Chapter 5).

The main conclusion of this section is that an electron or phonon coupling channel is essential for the generation of coherent spin waves, while their direct coupling to photons was excluded. However, the individual roles of electron and phonon excitations could not be separated in this experiment, which is a major objective for the work presented in the next Sections of this Chapter.

4.2 Determining the Laser-induced Changes of the Magnetic Anisotropy

A single-laser setup was used for our initial measurements of the magnetic anisotropy in epitaxial Fe samples deposited on (001) and (110) Ge substrates. While this

setup's capability has significant limitations compared to the dual-laser ASOPS technique (see Section 3.2), it does provide accurate measurements of the coherent spin wave frequencies over the first few hundreds of picoseconds after pump excitation. Subsequently, these frequencies are used to determine the time-averaged pump laser dependence of the magnetic anisotropy on a representative Fe/Ge (110) epitaxial sample. Further measurements on the same sample are carried out using the more sensitive ASOPS technique, which allowed us to resolve the temporal variation of the magnetic anisotropy.

An epitaxial Fe film with a thickness of 16.5 nm was grown on a single crystalline Ge (110) substrate using MBE deposition. An Au overlayer (4 nm) was deposited on top of the Fe film to assure the protection against oxidation under the ambient exposure. The Fe film deposition was performed at room temperature in order to minimize the interfacial Fe-Ge intermixing that takes place at larger temperatures [4.25].

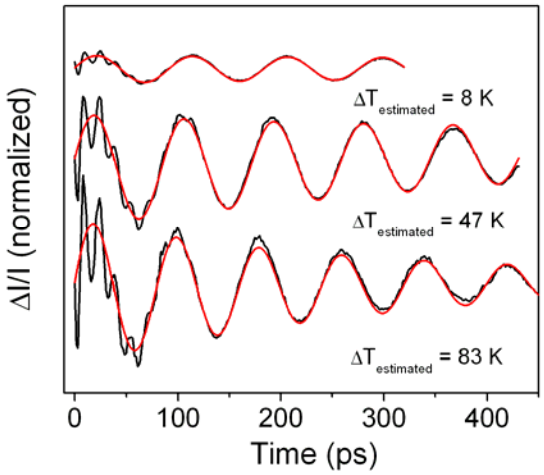

Figure 4.4 Experimental TR-MOKE spectra (black) and fits (red) at several laser-induced transient temperatures for Au(4nm)/ Fe(16.5nm)/ MgO(100) sample. The magnetic field of 1200 Oe was applied in-plane of the sample and at 22^0 from the <100> easy axis. The fast oscillations at t < 50ps, unaccounted in the fit, corresponds to a strain wave detected in the substrate (see Section 3.4).

Some experimental data obtained on this sample were already shown in Section 3.5 in order to estimate the magnitude of Gilbert damping. To reveal different aspects of

the spin wave behavior, additional coherent magnetization switching (CMS) studies on this sample will also be shown in Section 5.2.

Figure 4.4 shows an example of typical experimental data and curve fits for the coherent spin oscillations as function of the pump laser fluence for the case when the external magnetic field has a value of 1200 Oe and is applied at 22^0 from the in-plane magnetic easy axis of the sample or the <001> axis of the film. The experimental data fit well a damped cosine function with adjustable amplitude, frequency, phase, and exponential decay. Next, we plot the frequency determined by this approach as a function of the magnetic field direction and pump laser fluence in Figure 4.5. The associated fitting of the experimental data is an elaborate process and uses the formalism from Section 2.4. We briefly review the main ingredients of this formalism in the following.

First, we express the magnetic anisotropy energy in a coordinate system appropriate for the (110) orientation (see Section 2.3). The magnetic energy includes contributions from the magnetocrystalline, magnetoelastic, Zeeman and dipolar energies, which are dependent on the sample properties, pump laser excitation strength and experimental geometry. We neglect the exchange energy contribution to the magnetic energy by assuming that the magnetization dynamics is uniform and the spin precession occurs through a small angle around the direction of the instantaneous equilibrium direction. This is a reasonable assumption when the pump laser heats the Fe film almost uniformly, and when the sample thickness (20.5 nm, including the Au cap layer) is slightly smaller than that of the pump laser extinction depth of about 22 nm. Since the coherent spin dynamics was shown to depend on the laser heating (see Section 4.1) then applying uniform heating within the sample depth is expected to excite the magnetization dynamics uniformly. On the other hand, a nonuniform laser heating was found to play a clear role only in thicker samples, as will be shown in Section 4.3, where the contribution of the exchange energy is considered explicitly in accounting for the experimental observations.

In a further step, the dynamical Landau-Lifshitz (LL) equation of motion, Eq. 2.47, for the magnetization vector is linearized by neglecting the damping and expanding

the total magnetic energy in polar coordinates as a function of small spin displacements around equilibrium position of H_{eff} (see section 2.4). Time-dependent solutions to LL equation have the form: $e^{-i\omega t}$ and determine the dispersion relation for the spin precession frequency, ω, for the Fe/Ge(110) sample (see eqns. 2.58 and 2.60). These equations can be compared with the experimental data provided the equilibrium angle of the magnetization is simultaneously obtained from eqns. 2.53 and 2.54. The comparison with the experimental data is completed by finding a numerical solution for the above equations, and matching the solution to the experimental data by adjusting the following parameters: ϕ - the equilibrium angle of magnetization for a particular direction of the external magnetic field, H, K_1 – the magnetocrystalline anisotropy constant, K_u – the uniaxial anisotropy constant, and M_{eff} - the magnitude of the magnetization. We use the bulk magnetoelastic coefficients in calculation of magnetic anisotropy (B_1=-3.43 MJ/m^3 and B_2= 7.83 MJ/m^3 [4.26], while the thermal strain, ε_T, is estimated from the value of the absorbed laser fluency, film thickness and the known bulk values of specific heat and thermal expansion in Eqs. 2.8a and 2.39.

In our experiments, ***H*** is applied parallel to the sample plane in order to determine the variation of magnetization precession frequencies as function of the ***H*** direction. In this configuration, the measurement is sensitive to the values of K_1 and K_u, but only weakly sensitive to the value of M_{eff}. Consequently, we see that adjusting freely the value of M_{eff} in our model, in order to match the experimental data, results in a large variation of K_1 and K_u. To avoid this difficulty rising uncertainties in the parameter determination we apply a procedure that is described in the following. Based on the estimation of transient temperature increase (ΔT_{est}) due to the laser excitation and the known temperature variation of M_s for bulk Fe [4.27], we expect a variation of M_s of about 2.5 % at the maximum laser fluency. In experiments we find that M_{eff} values within at most 10% of the bulk value of M_s of Fe, we then assume that M_{eff} varies as M_s with temperature. With this procedure we are left with only two adjustable parameters, K_1 and K_u, while ϕ is found from Eq. (2.54). As shown in Figure 4.5, the resulting fits are a good match to the experimental data. The values of K_1 and K_u represented in Figure 4.6 show a linear scaling with the laser fluency, as well as, with the estimated laser-induced transient temperatures (these temperatures are indicated in the inset of Figure 4.5).

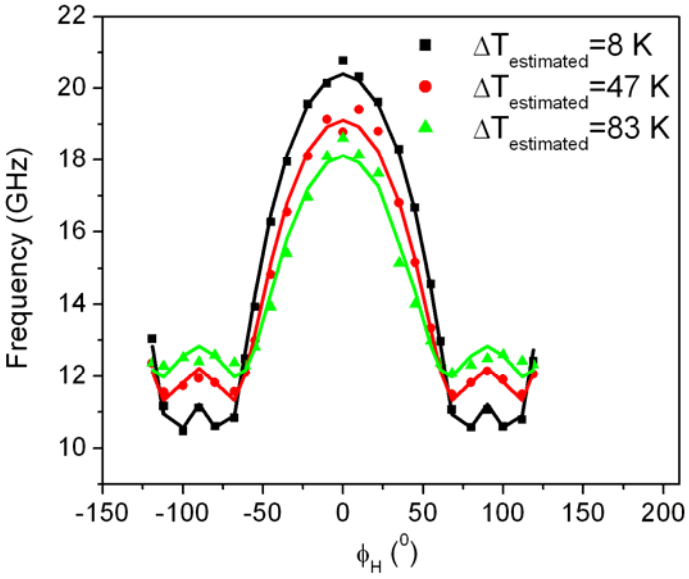

Figure 4.5 Frequency versus the in-plane angle of the magnetic field at three different laser powers (12 mW, 33 mW, and 58 mW) measured on a multilayer sample of Au (4 nm)/Fe (16.5 nm)/Ge (110). Symbols are the experimental data for the pump and probe at normal incidence, and the solid lines are the fitting based on the model discussed in the text. The estimated values for the laser-induced transient temperatures, $\Delta T_{estimated}$, are shown in inset.

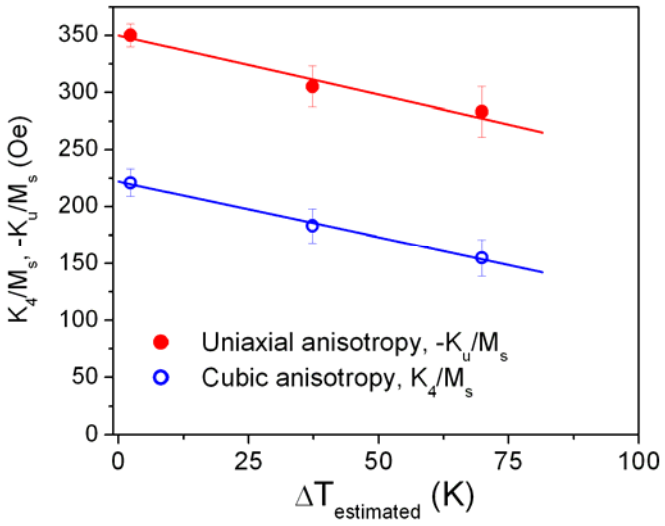

Figure 4.6 Variations of the magnetic anisotropy contributions with the laser-induced transient temperature increase. The symbols are extracted from the calculated data in Figure 4.4 (see text), and the solid lines represent the linear fitting for the two cases, uniaxial and cubic anisotropies.

The resulted variation of K_1 and K_u with ΔT_{est} is not well understood, and in the case of epitaxial thin films may include different contributions [4.1]. Elucidating the origin of these contributions is outside the scope of this thesis and will need to be pursued further. On the other hand, in Section 5.2, we will show that even if the origin of the temperature dependency of K_1 and K_u is not known, its determination is very useful for modeling and understanding the dynamical details of the coherent magnetization switching process of this structure.

4.3 Probing of the Laser-induced Magnon Mass Renormalization

In the previous section we have neglected the exchange energy (see eq. 2.65), which is a valid assumption for studies on films thinner than the pump laser optical absorption depth, δ. In such cases the spin dynamics can be treated in the macrospin approximation (see 2.4), which means that all spins are parallel within the sample volume. On the other hand, for the case of thicker films, the laser-induced thermal excitation can be inhomogenous within the depth of the film. This may lead to nonuniform spin wave dynamics characterized by a nonzero wavevector, which needs to include the effects of exchange interaction. We recall that the spin wave or magnon (a quantized spin wave) is the elementary wavelike excitation in the ferromagnet and is analogous to phonons vibrations in the crystal lattice [4.28]. However, in contrast to phonons that have linear dispersion, the dispersion relation for magnons is quadratic ($\omega \sim k^2$). The constant of proportionality between the square of the wavevector, k, and the magnon energy is the spin wave stiffness constant, D, which is equal to $2JSa^2$ in the Heisenberg model of ferromagnetism [4.28], where J is the exchange integral, S is the spin number and a is the lattice constant. Moreover, J depends on the Curie temperature, T_C, and the coordination number, z, within the Heisenberg model, i. e., $J = 3k_B T_C/2zS(S+1)$, which means that J depends on the crystalline lattice symmetry. Furthermore, the ratio $k_B T_C/zJ$ has a specific value for a certain crystal structure, and for the case of sc (simple-cubic), BCC (body-centered cubic) and FCC (face-centered cubic) and S=1/2 these values are: 0.28, 0.325, and 0.346, respectively [4.28]. This means that

within the Heisenberg model, which is a localized model of ferromagnetism, one could test experimentally the variation of the exchange constant with the crystalline symmetry. Such an experiment was reported for Cobalt thin films with FCC, BCC, and hexagonal-closed packed (HCP) structures [4.29], where no variation of D with the crystal symmetry was detected. Thus, the reduction of nearest neighbor number of atoms in the metallic ferromagnet does not seem to be reflected in the change of its D value. This result suggests that the D value is not easily derivable from the Heisenberg model for the case of ferromagnetic metals, which may be related to their itinerant properties within the band models of ferromagnetism [4.30-4.32]. In fact, the temperature dependence of D can be used to distinguish the localized model from the band model of ferromagnetism, since $\Delta D(T)/D_0 \sim T^{5/2}$ within the localized model and $\Delta D(T)/D_0 \sim T^2$ within the band model (referred to also as magnon-mass renormalization [4.33]. Both temperature dependences of D were observed in Fe [4.34], spin wave resonance in iron]. At room temperature, the quadratic temperature dependence of D strongly dominates in Fe, which means that the band model of ferromagnetism is more suitable to explain its properties. The magnon-mass renormalization in all transition metals ferromagnets (Ni, Fe, and Co) using the measurements of the magneto-resistance as a function of temperature was reported by Raquet et al. [4.35] have reported on the magnon-mass. These studies provide a link between the strength of electron-magnon scattering and the magnon-mass renormalization. Thus, the measurements of the temperature dependence of D can be used to elucidate the role of electron-magnon interaction in ferromagnetic metals. One open question in ultrafast optical pump-probe studies is the competition between different mechanisms used to explain the ultrafast demagnetization (UD) effect occurring in non-equilibrium, on the femtosecond timescale, in transition metal ferromagnets [4.36]. For the case of Fe, it was identified that electron-magnon interaction is responsible for the UD, whereas for the case of Co and Ni, the UD is interpreted very differently [4.24]. One way to address this discrepancy is to look at the behavior of D versus laser excitation, since we already pointed out above that D can be used to infer the strength of electron-magnon scattering. An idealized situation would be to probe the evolution of D during the UD demagnetization effect, although no experimental technique is presently capable to address such measurements. On the other hand, the coherent spin wave

studies provided access to the measurements of *D* on the picosecond timescale in Ni to find a value of *D* in rough agreement with prior known data [4.37]. Similar studies were also reported for Fe, although a very small D-value as compared to its accepted values was obtained [4.38]. In-detail investigations of the coherent spin waves able to determine *D* in epitaxial Fe films are shown in the following, with a focus on separating the thermal contribution induced by the pump laser excitation.

Epitaxial Fe samples with different thicknesses were grown by MBE deposition on a (100) MgO substrate. The deposition is performed at room temperature, and is followed by post-deposition annealing at 400 ^{0}C for a few minutes. We concluded that the annealing temperature and time were important in improving the structural quality of the films, including smooth surfaces. On the top of the epitaxial layer we have deposited both Au and Ag protective layers to ensure the sample stability under ambient exposure. By comparing the experimental results on both protected and unprotected layers, and under short exposure to air, the influence of the cap-layer was found to be negligible.

The experimental arrangement uses the ASOPS setup that was already shown Figure 3.1 and described in Section 3.2. One exception is that the pump and probe beams are directed perpendicular to the sample surface, where they are focused and overlapped. An external magnetic field of 650 Oe is applied parallel to the sample surface and its in-plane direction is varied during measurements. The experimental TR-MOKE traces are shown in Figure 4.7 for fixed experimental configuration and variable laser excitation strength, which were converted into average film temperatures, ΔT_{ave}, over the first 2 ns after the pump excitation. We have estimated these values by computing first the peak temperatures from the absorbed laser fluency, the film thickness, and the bulk values of the specific heat and thermal expansion from Eqs. 2.08 a) and 2.39. We then used TTR measurements (see Section 3.3) to obtain the average sample temperature estimates. A different aspect of spin dynamics is seen in Figure 4.7 on Au (4 nm)/Fe (37nm)/MgO(100) sample, compared to studies in thinner films (see Section 4.2). The observed coherent oscillations have a more complex structure due to a mixture between two coherent spin wave modes. To describe this type of spin dynamics, we use a superposition of two exponentially decaying cosine functions.

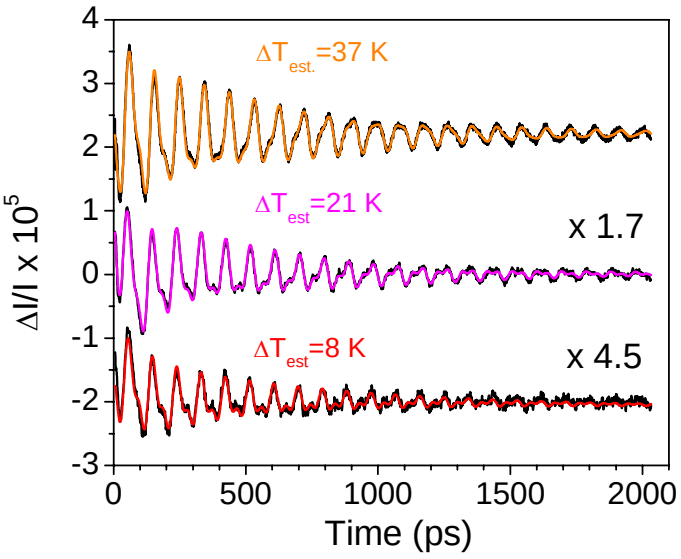

Figure 4.7 Experimental spectra (black) and fits as described in text (color) for the Au(4 nm)/Fe(37nm)/MgO(100) sample. The magnetic field of 650 Oe was applied in-plane of the sample and at 14^0 from the <110> hard axis. The lower curves are scalled for better visibility. The inset shows estimations for the laser-induced changes in sample temperature. These temperature values represent an average over the first 2 ns after pump excitation.

In this way, the behavior in the experimental data can be reproduced very well (see the fits from Figure 4.7). In reality, as we discus in the following, one mode (referred as mod1) has its wavevector, k ~ 0, while the second one (referred as mod2) has a nonzero k and we must consider the propagation effects. For simplicity, we ignore this in the analysis of the data obtained on the Au (4 nm)/Fe (37nm)/MgO(100) sample, but we will return to this point later (see Section 4.4). We proceed next with the measurements of the magnetic anisotropy similar to Section 4.1, but adapting the analysis procedure to (100) oriented films (see Sections 2.3 and 2.4), and including the effects of the exchange interaction based on the spin wave dispersion relation from Eq. 2.70. The results of this analysis as a function of the pump laser excitation strength (converted in average transient temperatures as described above) is shown in Figures 4.8 and 4.9, where we consider that the mode-1 has k=0 and mode-2 has $k=\pi/d$, where d is the film thickness. We see that within the experimental uncertainty, mod1 is not affected much by the pump laser-induced ΔT_{ave}, whereas mod2 visibly depends on ΔT_{ave}.

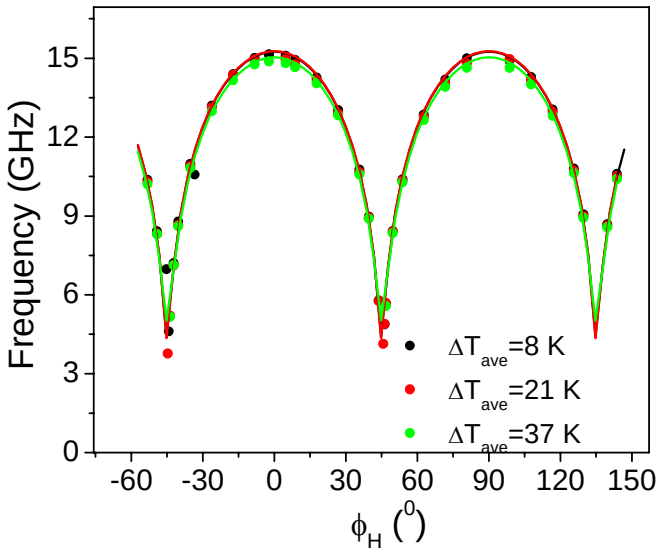

Figure 4.8 Laser-induced frequency shifts of the k=0 mode versus the in-plane magnetic field angle in Au(4 nm)/Fe(37 nm)/MgO(100) sample. The symbols are the experimental data and the solid lines are calculated as described in text. The inset shows estimations for the laser-induced changes in sample temperature. These temperature values represent an average over the first 2 ns after pump excitation.

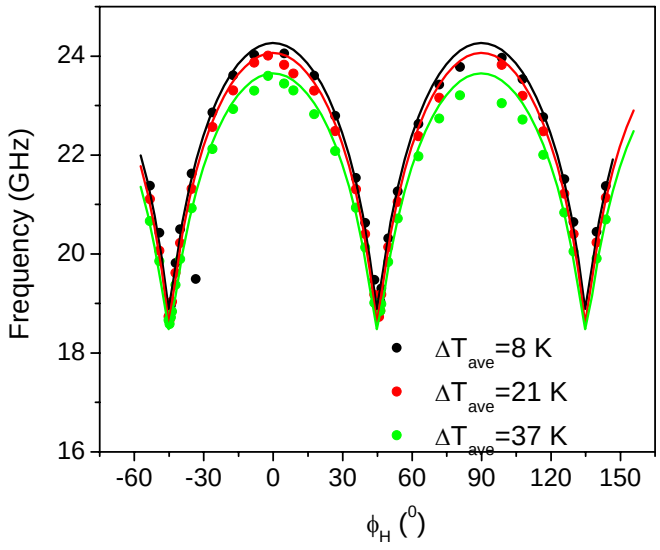

Figure 4.9 Laser-induced frequency shifts of the k=0.085 nm^{-1} mode versus the in-plane magnetic field angle in Au(4 nm)/Fe(37 nm)/MgO(100) sample. The symbols are the experimental data and the solid lines are calculated as described in text. The inset shows estimations for the laser-induced changes in sample temperature. These temperature values represent an average over the first 2 ns after pump excitation.

Moreover, we obtain a good match to the experimental data by using K_1 – cubic magnetostrytalline anisotropy within less 5% of its bulk value, $M_{eff} = M_s$ (bulk), and find that only the value of exchange stiffness parameter, D, changes appreciably with ΔT_{ave}, indicating a laser-induced magnon mass renormalization effect. Moreover, we find that the extrapolated value of D at $\Delta T_{ave} = 0$ is $D_{RT} = 27.6$ eV nm^{-2}, which is in excellent agreement with neutron scattering measurements of D in Fe. Additionally the maximum shift (at ΔT_{ave}=37 K) of D is with 7.2% lower than D_{RT}. This is the first detection of magnon-mass renormalization induced with optical pulses in ferromagnetic metals. Moreover, based on the recent temperature dependency of magnetoresistivity measurements of Raquet [4.35] we would have expected D_{RT} to shift with 7.6% for ΔT_{ave}=37 K. Considering the experimental uncertainties, the agreement with Raquet's electron-magnon scattering model and experimental results is excellent [4.35], which evidence that electron-magnon scattering plays an important role in laser-driven spin dynamics in Fe. Moreover, this result reveals indirectly that the electron-magnon scattering may be important at the earliest femtosecond timescales coinciding with UD and with its current interpretation for the case of Fe film [4.15].

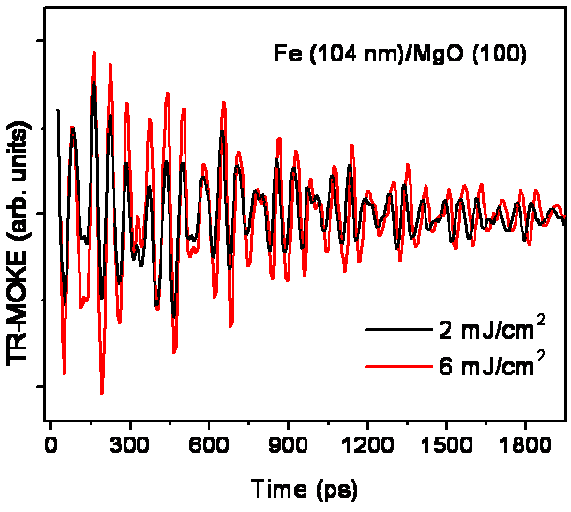

Figure 4.10 Laser fluence dependency of the TR-MOKE spectra for the multilayer sample of Au(4 nm)/Fe(104nm)/MgO(100).

We have verified the consistency of our findings on in studies of Fe films with variable thickness. Within the limits of our detection sensitivity, we can see the effects of magnon-mass renormalization for films of about 100 nm and smaller. The reason is that only at these thickness values, the laser-induced ΔT_{ave} is large enough to induce a detectable change of D corresponding to our maximum laser fluency. To provide an example of such studies, we show the data obtained on a Fe film with 104 nm thickness in Figure 4.10. It is easy to see that the dynamics of the coherent spin wave oscillations detected for this sample has a dependency on the laser fluency. We show the corresponding Fast-Fourier-Transforms (FFT) in Figure 4.11, where six coherent spin wave modes are detected, and their k values correspond to eqn. 2.69 ($k_n=n\pi/d$). It is visible in Figure 4.11 that the mode frequency for larger k (which implies larger frequency) is shifted more strongly under laser excitation.

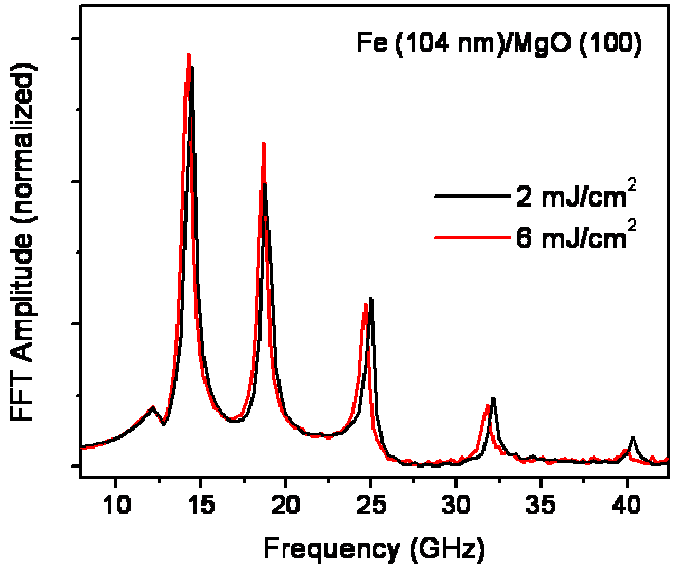

Figure 4.11 The FFT transforms of the spectra from Figure 4.9 as measured on a epitaxial Fe layer with the thickness of 104 nm on (100) MgO substrate.

In Figure 4.12 we plot the data extracted from Figure 4.11 as a function of k along with fits that allow only the variation of D. The fits are very good at all frequencies and provide roughly our sensitivity in measurements of the laser influence on D. We estimate

that the sensitivity is better than 2% in measuring the relative changes of D.

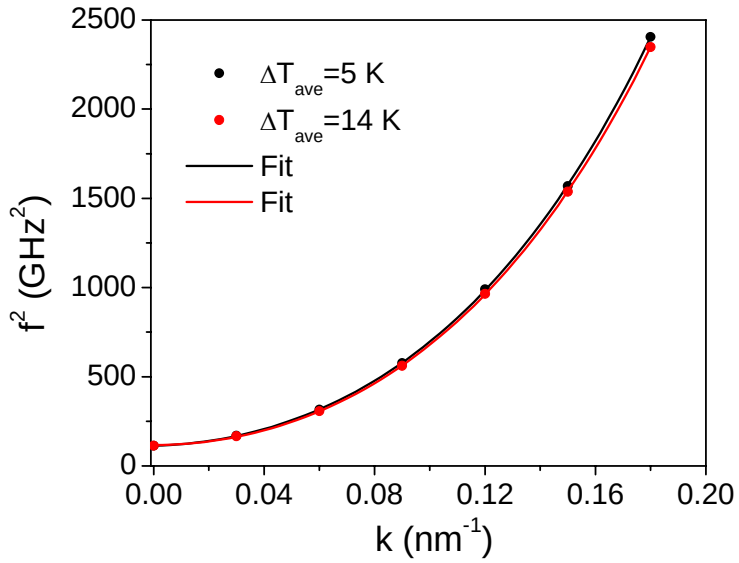

Figure 4.12 The relationship between the mode-frequency and the wavevector, k. The fitting procedure for the experimental data is described in the text. The inset shows estimations for the laser-induced changes in sample temperature. These temperature values represent an average over the first 2 ns after pump excitation.

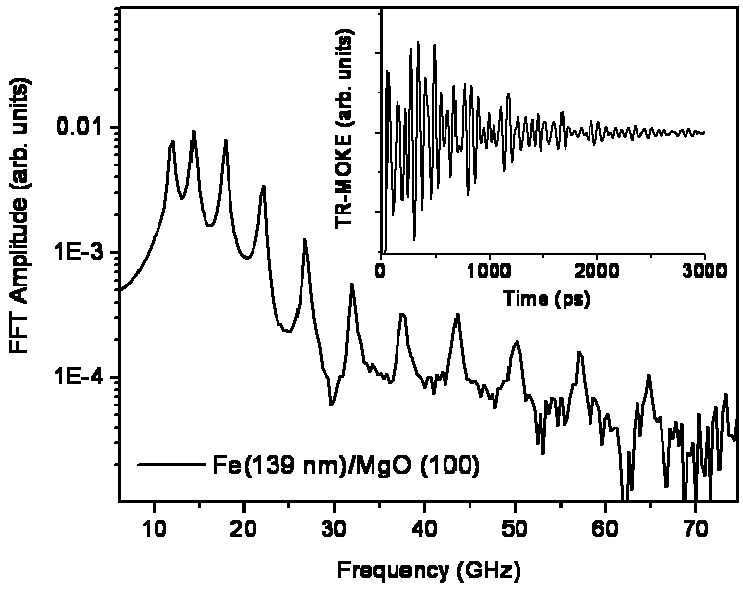

Figure 4.13 The TR-MOKE trace for Fe(139nm)/MgO(100) sample (inset) and the corresponding FFT transform of the spectrum from the inset.

We now show another example that illustrates the sensitivity of OPM technique developed throughout the work of this thesis. In Figure 4.13, we show that for a thicker Fe sample (139 nm) we can detect a very large number of coherent spin waves modes (11 modes in this case) in the same experimental geometry as in the experiments just described. This example demonstrates that the sensitivity of OPM is similar to standing spin wave resonance (SSWR) measurements that were already used for decades for studies of spin waves [4.34]. However, a few important differences need to be emphasized: OPM can study the physics of the coherent spin waves, as opposed to SSWR, and, moreover, it provides the flexibility of choosing any configuration for the magnetic field geometry in contrast to the case of a large magnetic field, applied only out of plane, in SSWR experiments.

4.4 Time-frequency Analysis of Coherent Spin Wave Propagation

So far, in the previous sections of this Chapter, we have shown that OPM studies of coherent spin wave dynamics can reveal the most important details of laser interaction with the metallic ferromagnet. This interaction is mediated by thermal excitation of electrons and phonons to eventually generate coherent spin waves in Fe epitaxial films via the change of the magnetocrystaline anisotropy and exchange stiffness parameter. What is sill missing from these studies is to isolate the effect of inhomogeneous laser excitation within the sample depth and resolve the details of the spin wave propagation and relaxation. Experimental probing of the propagating aspect of coherent spin wave dynamics is thus needed and can become instrumental for further understanding of the complex nature of ferromagnetic interaction in metallic materials. In the following, we will show that a coherent spin wave packet that is excited at the surface of Fe, subsequently propagates in the direction perpendicular to the sample surface and can be monitored during its deep penetration into the bulk of the material. In these studies we needed to use thicker Fe films, which have their thickness, d, appreciably larger than the optical penetration depth of the pump and probe lasers. This condition ensures the observation of coherent spin wave propagation with the required spatial resolution.

An epitaxial Fe sample wedge is grown by MBE deposition on a (100) MgO substrate. The wedge sample thickness was adjusted during the sample deposition between 140 and 2400 nm and across the length of the 12 mm substrate. Part of the sample was covered with 3 nm of Ag to protect it from oxidation, although only the unprotected region of the Fe wedge was used to perform the measurements that will be shown below. Within the area of this unprotected Fe wedge, no measurable deterioration of the sample properties could be detected after several weeks of exposure to ambient, during the duration of the optical pump-probe measurements. Due to the optical transparency of the MgO substrate at the pump and probe wavelengths (1580 nm and 780 nm, respectively), this sample is useful for the pump-probe measurements made on opposite sides of the film (pump incident on one side and probe pulse incident on the other). This experimental scheme was already used in Section 4.1, being helpful in observing the propagation of spin-dependent excitations, and it was further compared with the pump-probe measurements undertaken on the same side of the film.

The measurements are performed using the ASOPS technique (see Chapter 3) using an external magnetic field of 500-1000 Oe applied at 10^0 from the in-plane magnetic hard axis or the <110> crystallographic direction of Fe. A few experimental curves are shown in Figure 4.14 corresponding to different thicknesses of Fe film and preserving the rest of the experimental geometry the same. We recognize two contributions in oscillatory magnetic dynamics. One component at $t < 500$ ps does not seems to depend on thickness. A second wave packet is delayed to longer times with the increase of the film thickness and contains higher frequencies than the former. The thickness independent component has its frequency close to the magnetostatic Kittel mode ($k \sim 0$). Moreover, this mode appears to be localized at the interface since its amplitude does not depend on thickness (see Figure 4.15) even when we simultaneously change the magnetic field strength and the sample arrangement (from beams focused at normal incidence to beams focused on the sample at oblique incidence). The thickness dependent component is related to the propagation of a spin wave packet (SWP). As a general observation, in a similar way as the coherent acoustic phonons, the laser pump excites SWP, which propagates across the film and can be detected at the interface with the substrate. The packet includes a rather wide range of frequencies and wavevectors.

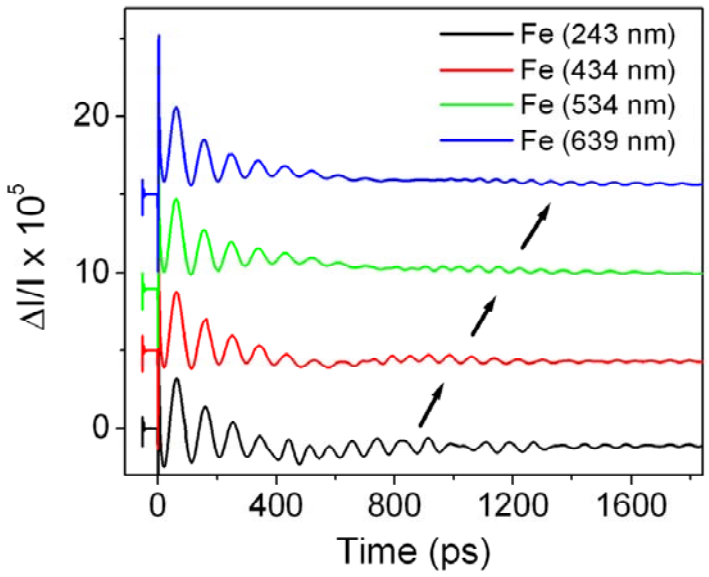

Figure 4.14 The TR-MOKE traces measured at the Fe/MgO interface for different film thicknesses, using the same sample geometry and the same pump laser fluence (6 mJ/cm^2).

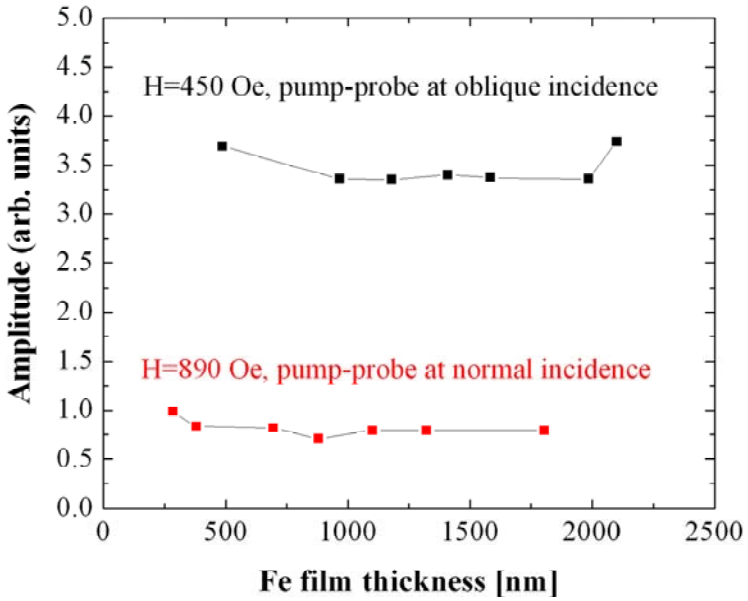

Figure 4.15 Amplitude of the thickness independent component for different measurement geometries. The magnetic field value and pump laser fluence (6 mJ/cm^2) were kept the same during the measurements.

To analyze the dynamics of the SWP we must separate the role of continuous versus discrete contributions of this SWP. This task can be accomplished, for example,

by modeling the spin wave dynamics directly in time domain [4.39]. We prefer to use a different approach, since in our case, applying an approach similar to Liu et al. [4.39] will result in making certain assumptions about the SWP excitation that may or may not be justified in the current experimental situation. On the other hand, a major focus of this thesis is to develop new techniques for identifying the mechanism behind the excitation of coherent spin wave dynamics, rather than assume it is known in a model.

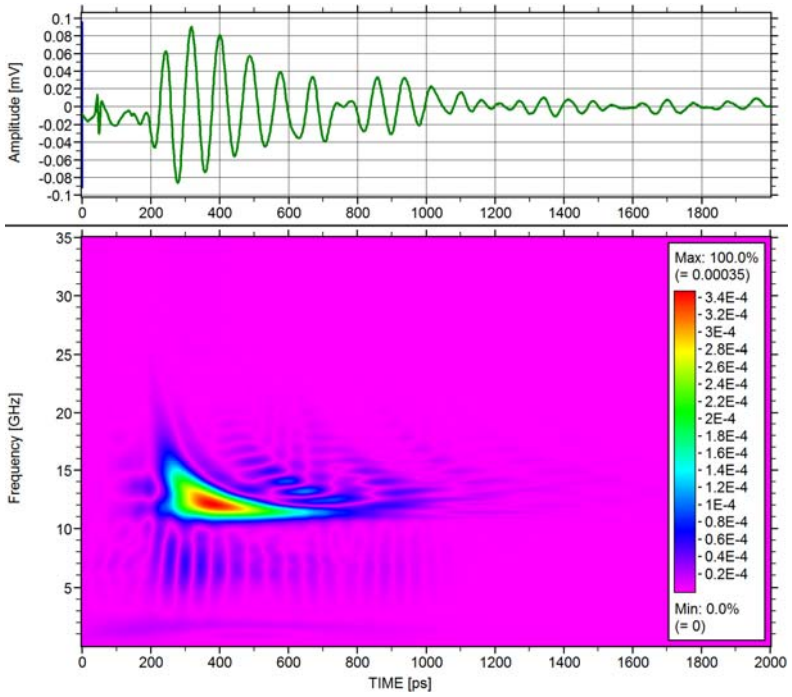

Figure 4.16 Choi-Williams transform of the MOKE signal detected at the Fe/MgO interface for a film thickness of 258 nm.

A very practical way to analyze intricate signals is to construct their corresponding time-frequency distributions [4.40], and, therefore, to obtain the time dependence of the frequency spectrum of any waveforms. We use here the Choi-Williams transform [4.41], usually applied in acoustics [4.42]. The Choi-Williams wavelet transforms of the MOKE signal detected at the Fe/MgO interface are shown in Figure 4.16-4.18. In a time-frequency representation, the arrival time at the interface, as well as the amplitude of the signal, can be observed for each frequency value.

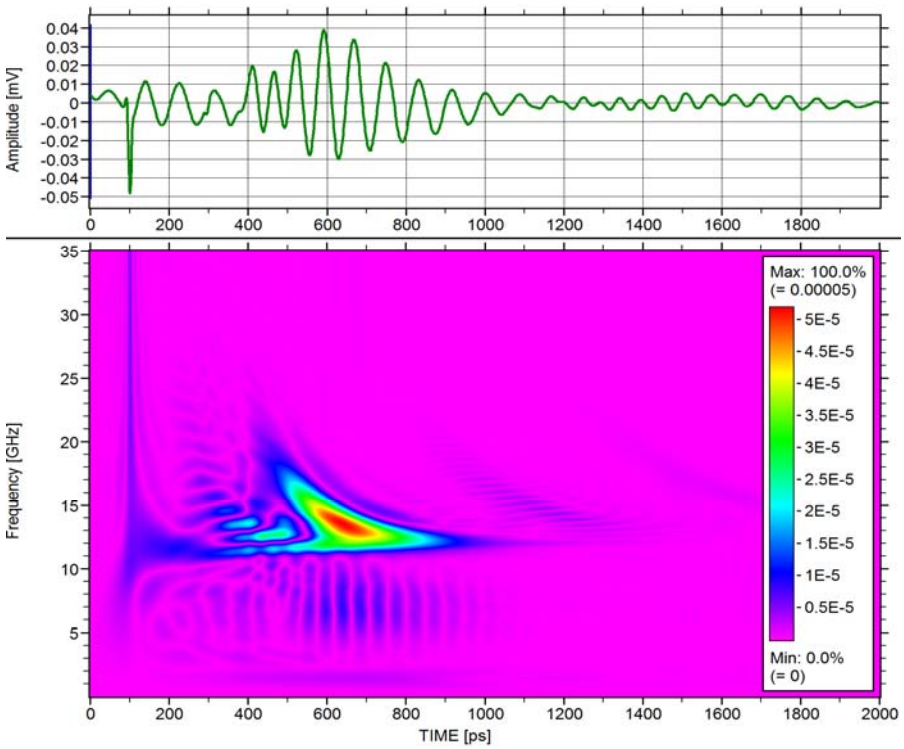

Figure 4.17 Choi-Williams transform of the MOKE signal detected at the Fe/MgO interface for a film thickness of 531 nm.

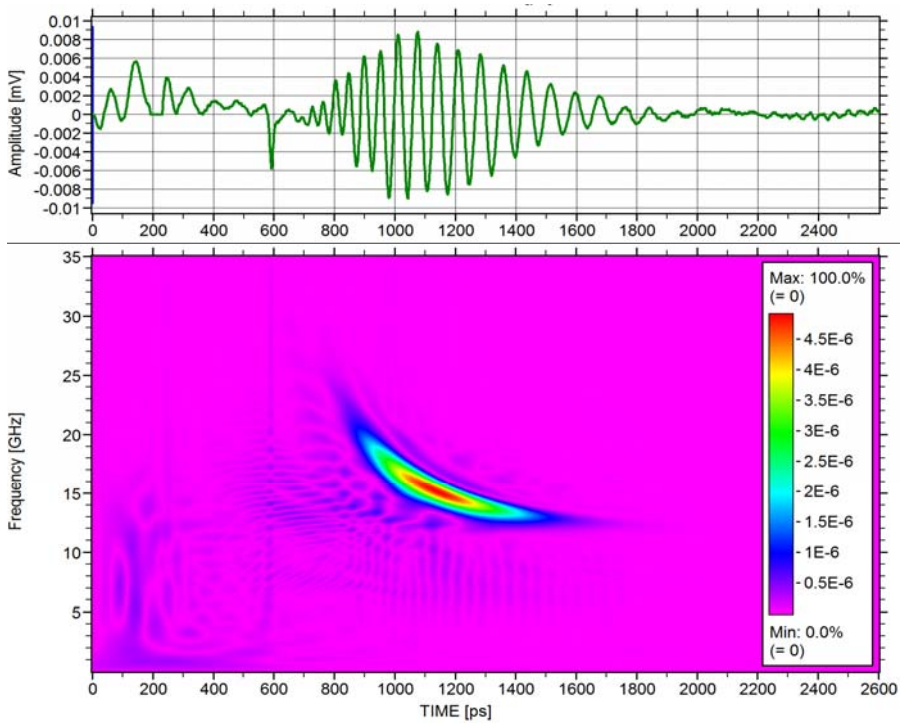

Figure 4.18 Choi-Williams transform of the MOKE signal detected at the Fe/MgO interface for a film thickness of 1057 nm.

Figure 4.19 shows the amplitudes of coherent spin waves as a function of Fe film thickness at selected frequencies. The amplitudes are decaying exponentially as a function of film thickness.

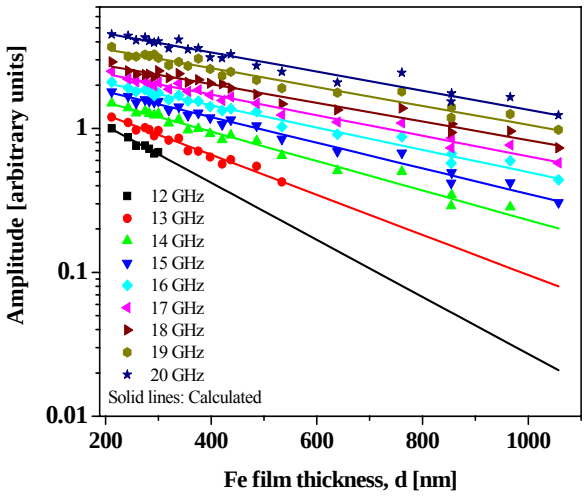

Figure 4.19 Decaying amplitudes of the coherent spin waves as a function of Fe film thickness at selected frequencies: experimental (symbols) and calculated (solid lines from exponential fitting). The pump and probe are applied on different sides of the films.

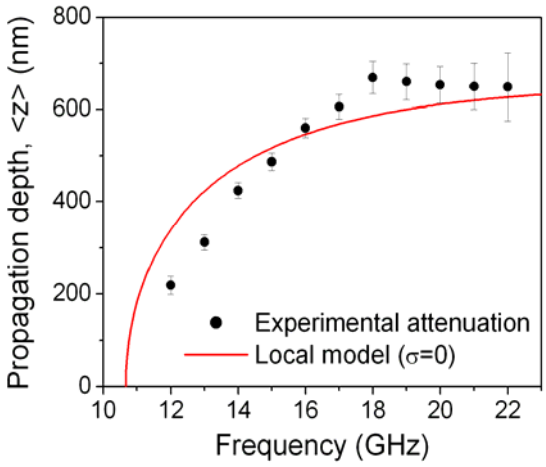

Figure 4.20 Attenuation length as function of spin wave frequency obtained from fits of data from Fig. 4.19 (dots and estimated error margins). The red line is the best fit obtained with a model that ignores the finite film conduction. An effective Gilbert damping, $\alpha = 0.11$, is obtained from the fit.

If considering that each spin wave decays during propagation in a semi-infinite body, then the Eqn. 2.81 can be used to calculate the attenuation length. The frequency dependence of attenuation length is presented in Figure 4.20. The general trend is similar for both experimental and theoretical data, but there is a clear difference for lower frequency values. This could be the effect of metallic conductivity, which introduces an additional skin effect for the propagating magnetic waves, as we briefly mentioned in Section 2.4.

The arrival time at the interface, that is in fact the spin wave propagation time, can be used to determine the group velocity. Figure 4.21 shows that the propagation time dependency of film thickness is quite linear and can be used to estimate the group velocity for individual frequencies. The experimental results are presented in Fig. 4.22 and compared with the theoretical expectation based on magnetic parameters of Fe.

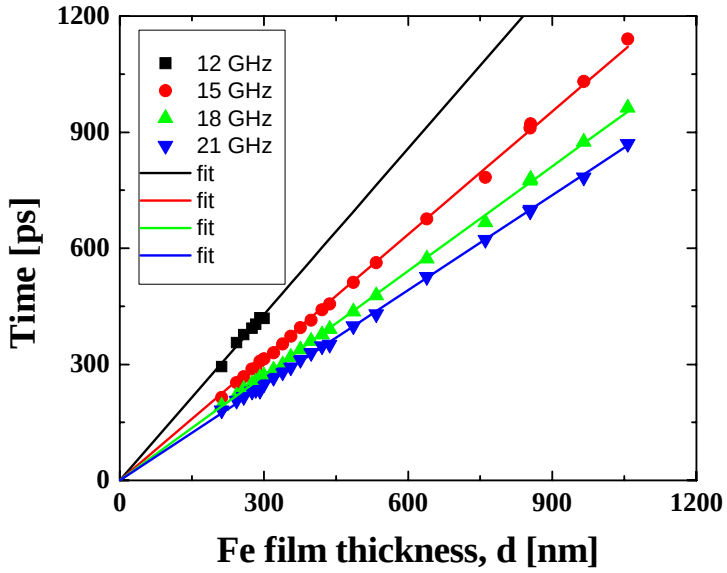

Figure 4.21 The experimental data (symbols) and calculated (solid lines) representing the propagation time between the Fe film boundaries as a function of film thickness. From these data were determined the coherent spin wave group velocities for a few selected frequencies (see Figure 4.22).

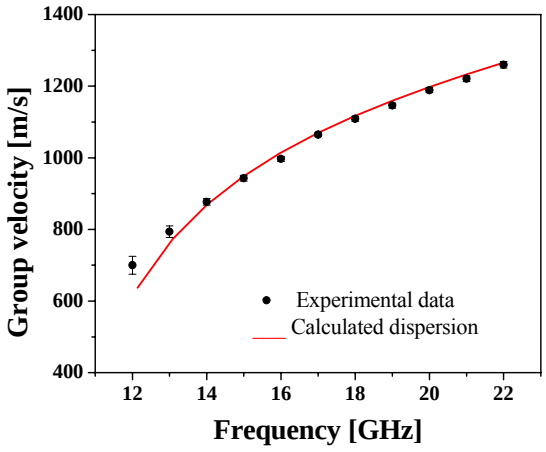

Figure 4.22 Spin waves group velocities (symbols with error margins), deduced from the data in Figure 4.21, as a function of the frequency. The red line is the calculated dispersion relation from the known Fe magnetic properties. The magnetic field of about 400 Oe was oriented at 10^0 away from the in-plane <110> hard axis.

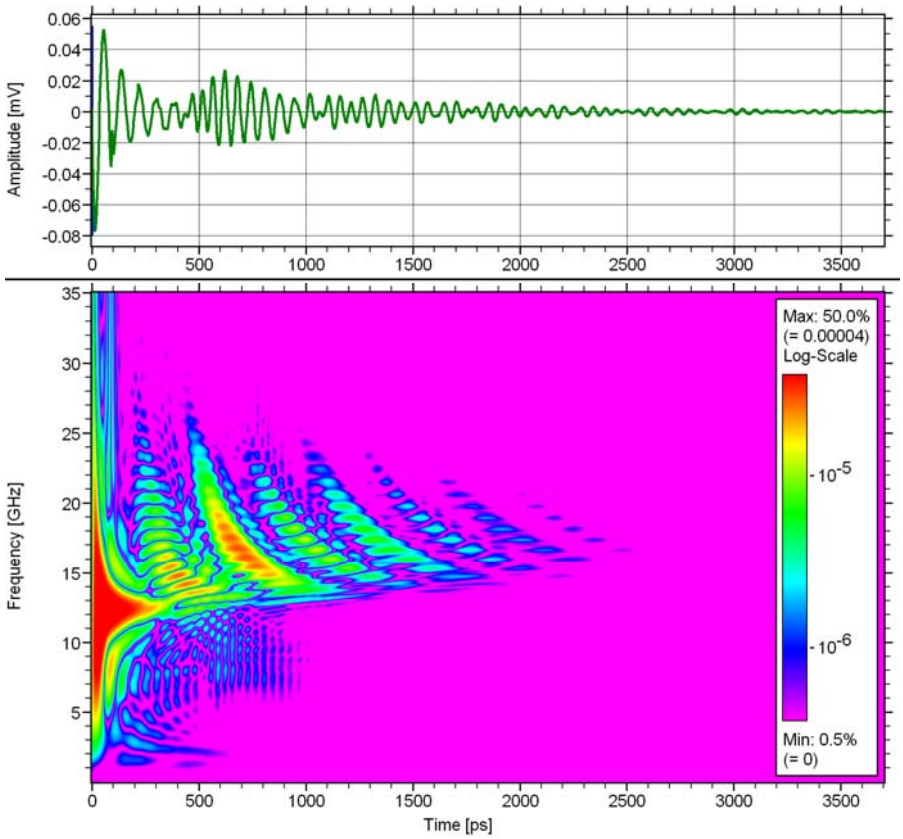

Figure 4.23 Choi-Williams transform of the MOKE signal detected at the film surface for a film thickness of 330 nm.

As SWP does not show any discrete structure, it was necessary to probe MOKE on the film surface in order to observe the formation of standing spin waves (SSW). An example of Choi-Williams transform corresponding to a 330 nm thick Fe film is presented in Figure 4.23. This time, a discrete structure of the signal is clearly visible, meaning that the standing spin waves are formed by selective reflection at the interface. Moreover, we can follow the echoes resulting from multiple reflections at surface and interface. By analyzing the time locations of these echoes for individual modes (Figure 4.24), it is possible to determine the group velocity of SSW (Figure 4.25). By comparing the experimental data with the theoretical prediction we found an outstanding match (see Figure 4.25). It is also possible to estimate the attenuation length from the change in amplitude of SSW due to multiple travels across the film. The results for two different

thicknesses are presented in Figure 4.26. In this case, the experimental results are also in fair match with the theoretical prediction.

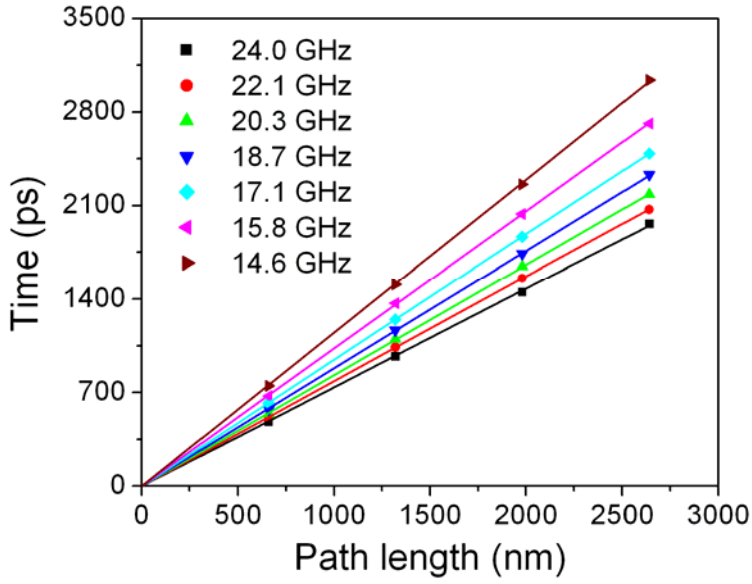

Figure 4.24 Experimental data (symbols) and calculated (solid lines) representing the propagation time of standing spin waves as a function of flight path length through the film. From these data were determined the standing spin wave group velocities up to the seventh order (see Figure 4.25).

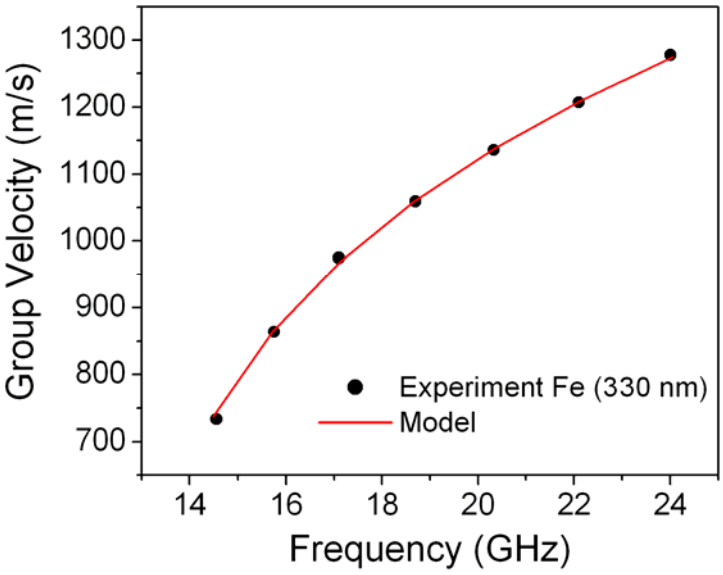

Figure 4.25 Group velocities of standing spin waves up to the seventh order as a function of the frequency for a Fe layer of 330 nm: (a) experimental data (symbols) deduced from Figure 4.21, and (b) theoretical calculation (red line) from the dispersion relation in Eqn. (2.70).

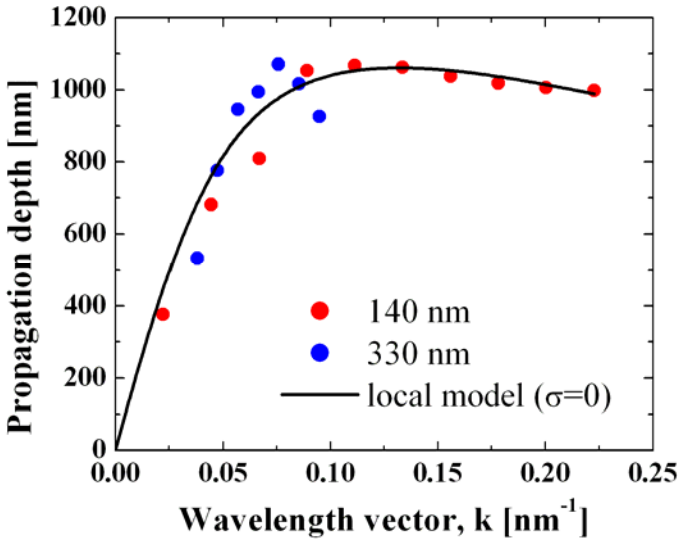

Figure 4.26 Attenuation lengths as function of standing spin wave frequency (dots) for two values of film thickness. The black line is the best fit obtained from Eq. (2.81). An effective Gilbert damping, $\alpha = 0.05$, is obtained from the fit.

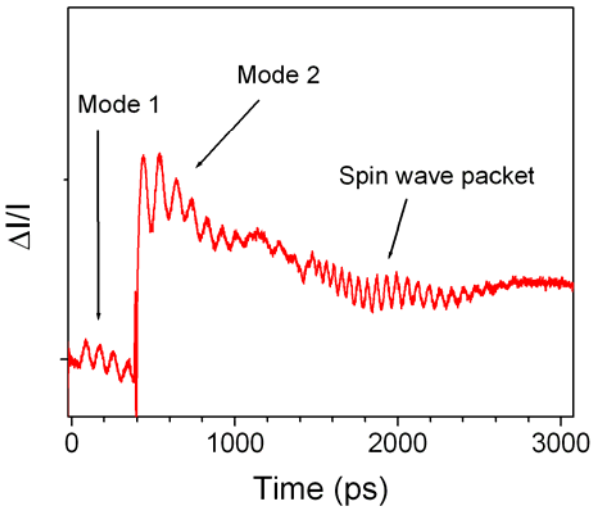

Figure 4.27 The TR-MOKE trace measured at the Fe/MgO interface for a film with a 2133 nm thickness. The pump and probe beams are applied on different sides of the film.

All the data reported in the previous paragraphs are referring to experiments done on film thicknesses over 100 nm, but below 1 μm. To show what can be seen at the Fe/MgO interface for a film thickness of 1 μm or more, we feature Figure 4.27. There are three characteristic time frames displaying the magnetic dynamics specifics. In the

first frame, below 400 ps, we can recognize the fundamental magnetostatic mode. The sharp discontinuity at 400 ps corresponds with the arrival of acoustic (Thomsen) shock wave at the interface. It seems that this elastic wave excites dynamically the magnetostatic mode by magnetoelestic coupling. Thus, the amplitude of the fundamental mode is increased in the next timeframe, but decays relatively fast (up to 1200 ps). Last coming is the SWP, as we previously observed in thinner films. Here we concentrate on the fundamental mode (mode 1 in Figure 4.27) observed before the arrival of elastic wave (with the speed of sound). Firstly, it is not clear how this mode was generated at the interface much faster than the speed of sound. Secondly, we can estimate the attenuation length by comparing the wave amplitude for different film thicknesses (see Figure 4.28).

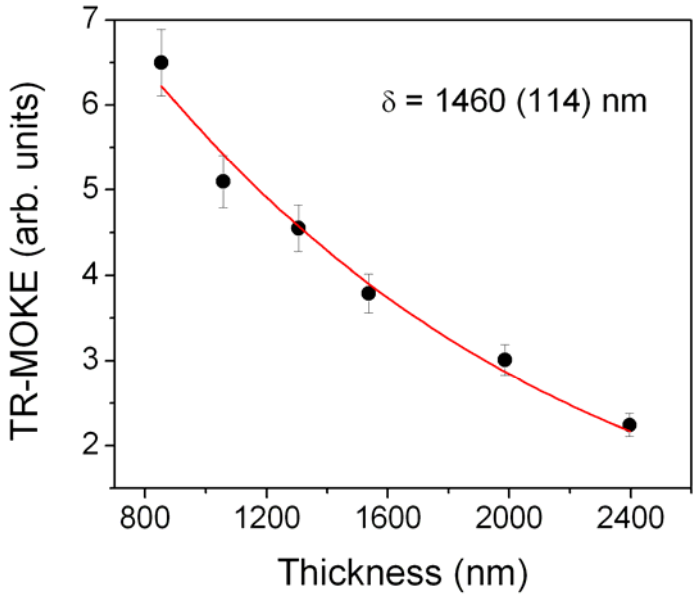

Figure 4.28 Decaying amplitudes (dots) of the mode 1 from Figure 4.27 as a function of film thickness. The line is an exponential decay with a decay length, δ, with the value shown in inset.

The obtained value of about 1.5 μm corresponds to the skin depth for nonmagnetic metals. An electromagnetic mechanism may be responsible for generating this mode, but much more experimental efforts are needed to clarify this point.

REFERENCES FOR CHAPTER 4

4.1 G. Wastlbauer and J. A. C. Bland, "Structural and magnetic properties of ultrathin epitaxial Fe films on GaAs (001) and related semiconductor substrates," Advances in Physics 54 (2), 137-219 (2005).

4.2 M. Farle, "Ferromagnetic resonance of ultrathin metallic layers," Reports on Progress in Physics 61, 755 (1998)

4.3 B. Heinrich and J. F. Cochran, "Ultrathin metallic magnetic films: magnetic anisotropies and exchange interactions," Advances in Physics 42 (5), 523-639 (1993).

4.4 B. Heinrich, "Radio Frequency Techniques," Ultrathin Magnetic Structures II, 195-296 (2005).

4.5 G. Ju, A. V. Nurmikko, R. F. C. Farrow, R. F. Marks, M. J. Carey, and B. A. Gurney, "Ultrafast time resolved photoinduced magnetization rotation in a ferromagnetic/antiferromagnetic exchange coupled system," Physical review letters 82 (18), 3705-3708 (1999).

4.6 M. van Kampen, C. Jozsa, J. T. Kohlhepp, P. LeClair, L. Lagae, W. J. M.de Jonge, and B. Koopmans, ″All-optical probe of coherent spin waves,″ Phys. Rev. Lett. 88, 227201 (2002).

4.7 V. A. Stoica, R. Merlin, R. A. Lukaszew, and R. Clarke, "Time-resolved spin dynamics studies of ferromagnetic thin films grown by molecular beam epitaxy," Bulletin of the American Physical Society (2005).

4.8 H. B. Zhao, D. Talbayev, G. Lüpke, A. T. Hanbicki, C. H. Li, and B. T. Jonker, "Ultrafast interface magnetization dynamics in Fe/ AlGaAs (001) heterostructure," Applied Physics Letters 91, 052111 (2007).

4.9 S. Mizukami, E. P. Sajitha, D. Watanabe, F. Wu, T. Miyazaki, H. Naganuma, M. Oogane, and Y. Ando, "Gilbert damping in perpendicularly magnetized Pt/Co/Pt films investigated by all-optical pump-probe technique," Applied Physics Letters 96, 152502 (2010).

4.10 J. Walowski, G. Müller, M. Djordjevic, M. Münzenberg, M. Kläui, C. A. F. Vaz, and J. A. C. Bland, "Energy equilibration processes of electrons, magnons, and phonons at the femtosecond time scale," Physical review letters 101 (23), 237401 (2008).

4.11 V. A. Stoica, Yu-M. Sheu, D. A. Reis, and R. Clarke, "Wideband detection of transient solid-state dynamics using ultrafast fiber lasers and asynchronous optical sampling," Opt. Express 16, 2322-2335 (2008); V.A Stoica, R. Clarke, "Method and system for measuring at least one property including a magnetic property of a material using pulsed laser sources", United States Patent Application 20090212769, Application Number: 12/315906, Publication Date: 08/27/2009.

4.12 H. B. Zhao, D. Talbayev, Y. Fan, G. Lüpke, A. T. Hanbicki, C. H. Li, and B. T. Jonker, "Photoinduced spin waves in Fe/AlGaAs (001) heterostructure," Physica Status Solidi (c) 5 (8), 2627-2631 (2008).

4.13 S. Mizukami, H. Abe, D. Watanabe, M. Oogane, Y. Ando, and T. Miyazaki, "Gilbert Damping for Various Ni80Fe20 Thin Films Investigated Using All-Optical Pump–Probe Detection and Ferromagnetic Resonance," Applied Physics Express 1 (12), 1301 (2008).

4.14 Y. H. Ren, C. Wu, Y. Gong, C. Pettiford, and N. X. Sun, "Ultrafast optical study of spin wave resonance and relaxation in a CoFe/PtMn/CoFe trilayer film," Journal of Applied Physics 105, 07D304 (2009).

4.15 E. Carpene, E. Mancini, D. Dazzi, C. Dallera, E. Puppin, and S. De Silvestri, "Ultrafast three-dimensional magnetization precession and magnetic anisotropy of a photoexcited thin film of iron," Physical review B. Condensed matter and materials physics 81 (6) (2010).

4.16 F. Dalla Longa, J. T. Kohlhepp, W. J. M. de Jonge, and B. Koopmans, "Resolving the genuine laser-induced ultrafast dynamics of exchange interaction in ferromagnet/ antiferromagnet bilayers," Physical Review B 81 (9), 94435.

4.17 J. Y. Bigot, T. A. Pham, and T. Barisien, "Femtosecond time resolved molecular dynamics of a polydiacetylene backbone," Chemical Physics Letters 259 (5-6), 469-474 (1996).

4.18 G. P. Zhang and W. Hübner, "Laser-induced ultrafast demagnetization in ferromagnetic metals," Physical review letters 85 (14), 3025-3028 (2000).

4.19 B. Koopmans, M. Van Kampen, J. T. Kohlhepp, and W. J. M. De Jonge, "Ultrafast magneto-optics in nickel: magnetism or optics?" Physical review letters 85 (4), 844-847 (2000).

4.20 J. Y. Bigot, L. Guidoni, E. Beaurepaire, and P. N. Saeta, "Femtosecond spectrotemporal magneto-optics," Physical review letters 93 (7), 77401 (2004).

4.21 I. Radu, G. Woltersdorf, M. Kiessling, A. Melnikov, U. Bovensiepen, J. U. Thiele, and C. H. Back, "Laser-induced magnetization dynamics of lanthanide-doped permalloy thin films," Physical review letters 102 (11), 117201 (2009).

4.22 B. Koopmans, J. J. M. Ruigrok, F. D. Longa, and W. J. M. de Jonge, "Unifying ultrafast magnetization dynamics," Physical review letters 95 (26), 267207 (2005).

4.23 B. Koopmans, G. Malinowski, F. Dalla Longa, D. Steiauf, M. Fähnle, T. Roth, M. Cinchetti, and M. Aeschlimann, "Explaining the paradoxical diversity of ultrafast laser-induced demagnetization," Nature Materials 9 (3), 259-265 (2009).

4.24 J. Y. Bigot, M. Vomir, and E. Beaurepaire, "Coherent ultrafast magnetism induced by femtosecond laser pulses," Nature Physics (2009).

4.25 P. Ma and PR Norton, “Growth of ultrathin Fe films on Ge(100): Structure and magnetic properties,” Phys. Rev. B 56, 9881 (1997.

4.26 D. Sander, "The correlation between mechanical stress and magnetic anisotropy in ultrathin films," Reports on Progress in Physics 62, 809 (1999).

4.27 S.D. Hanham, A.S. Arrott, and B. Heinrich, J. Appl. Phys. 52, 1941 (1981).

4.28 C. Kittel, Introduction to solid state physics (Wiley New York, 1996).

4.29 X. Liu, M. M. Steiner, R. Sooryakumar, G. A. Prinz, R. F. C. Farrow, and G. Harp, "Exchange stiffness, magnetization, and spin waves in cubic and hexagonal phases of cobalt," Physical Review B 53 (18), 12166-12172 (1996).

4.30 T. Izuyama, "Collective Excitations of Electrons in Degenerate Bands. I---Spin Waves in Stoner's Model of Ferromagnetism," Progress of Theoretical Physics 23, 969-983 (1960).

4.31 T. Izuyama, D. J. Kim, and R. Kubo, "Band theoretical interpretation of neutron diffraction phenomena in ferromagnetic metals," Journal of the Physical Society of Japan 18, 1025-1042 (1963).

4.32 Izuyama and R. Kubo, J. Appl. Phys. 35, 1074 (1964).

4.33 M. W. Stringfellow, J. Phys. C 2, 950 (1968).

4.34 T. G. Phillips, "Spin wave resonance in iron," Proceedings of the Royal Society of London. Series A, Mathematical and Physical Sciences 292 (1429), 224-239 (1966).

4.35 B. Raquet, M. Viret, E. Sondergard, O. Cespedes, and R. Mamy, "Electron-magnon scattering and magnetic resistivity in 3d ferromagnets," Physical Review B 66 (2), 24433 (2002).

4.36 E. Beaurepaire, J. C. Merle, A. Daunois, and J. Y. Bigot, "Ultrafast spin dynamics in ferromagnetic nickel," Physical review letters 76 (22), 4250-4253 (1996).

4.37 Van Kampen, and Koopmans Phys. Rev. Lett, (2002).

4.38 H. B. Zhao, D. Talbayev, G. Lüpke, A. T. Hanbicki, C. H. Li, and B. T. Jonker, "Ultrafast interface magnetization dynamics in Fe/ AlGaAs (001) heterostructure," Applied Physics Letters 91, 052111 (2007).

4.39 Z. Liu, F. Giesen, X. Zhu, R. D. Sydora, and M. R. Freeman, "Spin Wave Dynamics and the Determination of Intrinsic Damping in Locally Excited Permalloy Thin Films," Physical review letters 98 (8), 87201 (2007).

4.40 L. Cohen, ″Time-frequency analysis,″ Prentice Hall PTR. (1995).

4.41 H.I. Choi and W. J. Williams "Imprpoved time-frequency representation of multicomponent signals using exponential kernels." IEEE Transactions on Acoustics, Speech, and Signal Processing 37(6): 862-871 (1989).

4.42 http://www.vallen.de/wavelet/

CHAPTER 5

COHERENT PRECESSIONAL MAGNETIZATION SWITCHING TRIGGERED BY OPTICAL PULSES

There are three primary ways through which the magnetization of a metallic ferromagnet can be manipulated with ultrafast lasers: (a) via an optical (non-thermal) mechanism influencing the spin dynamics (for example inverse Faraday rotation [5.1], (b) via longitudinal spin excitations (for example a Stoner excitation [1.1]), and (c) via transverse spin excitations (spin waves). It is of interest to achieve control of the magnetization via any of such mechanisms in order to improve the basic understanding of the ultrafast spin dynamics and to search for an efficient solution that can lead to magnetization switching. Moreover, except in case (a), which implies coherent interaction by definition, the processes in (b) and (c) can occur either coherently or incoherently.

We already discussed the results of an experiment related to (a) in Section 4.1, and in the case of Fe/MgO (100) samples we do not find evidence for such a process. Furthermore, it is difficult to determine the relative contributions coming from (b) and (c) in experiments and in this thesis we have focused on studies of coherent spin waves. In these studies we demonstrate that optical manipulation of long-wavelength spin waves provides the needed access to coherent magnetization switching.

In Section 5.1, we give a brief literature overview of femtosecond-scale time-dependence of magnetism in metals, which was seen to occur via an ultrafast demagnetization (UD) process. In Section 5.2, we demonstrate, for the first time, the use of femtosecond optical excitation for control of a coherent spin reorientation transition, which enables precessional magnetization switching on the picosecond timescale.

5.1 Ultrafast Demagnetization Experiments in Transition Metal Ferromagnets: A Brief Literature Review

A detailed discussion of the spin dynamics in ferromagnetic metals, induced with femtosecond optical pulses, needs take into account the timescales of excitation and relaxation starting immediately after the optical pulse irradiation of the material. Secondly, it is important to distinguish the incoherent and coherent aspects of the spin dynamics in the experimental observations. Accordingly, the discussion starts on the femtosecond timescale, where the intriguing experimental observation of the ultrafast demagnetization (UD) of Ni was made in the pioneering work of Beaurepaire and coworkers [5.2]. This effect consists in a sudden decrease of the MOKE contrast on a femtosecond timescale comparable with the optical pulse duration (~ 60 fs in the original experiment) followed by relatively slower relaxation on the ps timescale.

One interpretation of the experimental results relies on a three-temperature model (TTM), which included hot (suprathermal) electrons and spins, as well as their thermalization with the lattice. The main result of the TTM model [5.2] is that hot electrons and their interaction with spins seemed to produce a sudden rise of the spin temperature in a time as short as the optical pulse duration, while a common spin-electron temperature was subsequently reached in ~ 2 ps. Another puzzling result from this analysis is a very fast spin-lattice relaxation time, $\tau_{S\text{-}L}$, of ~ 6 ps. This result is in stark contrast to prior theoretical estimations (~ 100 ns) for spin-lattice relaxation time in ferromagnetic metals [5.3] and experimental studies using spin-polarized photoemission (~ 30 ps) [5.4-5.6]. Clearly a better understanding of the ultrafast demagnetization process is needed, especially regarding the quantitative estimation of $\tau_{S\text{-}L}$ [1.1].

One recent example which emphasizes the implications of the above discrepancy refers to a theoretical interpretation [5.7] given for the recently discovered Spin Seebeck effect in ferromagnetic transition metals [5.8]. An important parameter in this interpretation is the magnitude of $\tau_{S\text{-}L,}$ which was taken to be ~ 10^{-7} s, following the very early theoretical estimates [5.3]. This $\tau_{S\text{-}L}$ is about 5 orders of magnitude longer the one inferred from Beaurepaire's experiments! One possible source of confusion is the possibility that different band configurations for the electrons, featuring different types of

behavior during spin-lattice relaxation, are observed in different experiments. These differences will need to be better identified in the future.

Another implication of the UD experiments is to help in elucidating the fundamental limits of the ultrafast magnetic recording applications. Here again, $\tau_{S\text{-}L}$ has an important role since it limits the speed at which the switching of the magnetization can relax to a new stable state. It is hoped that optically-induced magnetization switching (i.e. the reversal of the magnetization vector to the opposite direction via a π rotation) can be realized at the femtosecond timescale, no observations of switching have been reported on these ultrafast timescales in metallic ferromagnets; only the well known existence of the ultrafast demagnetization effect. The difference is that the demagnetization proceeds via spin disorder up to the total quenching of the magnetization, whereas the switching of the magnetization to the opposite direction needs to preserve the magnetic ordering to be relevant for ultrafast magnetic recording applications.

It appears that one exception was reported in the literature, which occurred for the case of metallic CoFeGd *ferrimagnetic* alloy [5.9]. ″Ferrimagnetic″ here refers to a spin configuration with zero net magnetization, but with ordered groups of aligned spins separated by groups of anti-aligned spins. Femtosecond magnetic switching via an inverse Faraday effect [5.10] seems to have been invalidated in this material by later observations that the magnetic switching is actually completed on a timescale of tens of picoseconds in these ferrimagnetic metallic alloys [5.11] at least two orders of magnitude slower than the original claim. Thus, as evidenced so far in experiments, only the standard demagnetization occurs on the femtosecond timescale for both ferrimagnetic and ferromagnetic metallic elements and alloys.

In the following, by limiting the discussion to metallic *ferromagnets*, it is important to note that different authors have provided contrasting interpretations concerning the microsopic origin of ultrafast demagnetization when analyzing similar experimental results. Chronologically and shortly after Beaurepaire's report, it was confirmed that the UD process exits and is also present at the Ni surface [5.12]. However, we should note here that, in that study, the spin thermalization was found to

coincide with the electron gas thermalization on a timescale of 280 fs rather than 2 ps, as stated in Ref. 5.2. No insight on the microscopic origin of UD could yet be inferred.

A first attempt at a microscopic interpretation came after presenting experimental results obtained with time-resolved spin polarized photoemission which showed two timescales of demagnetization in ultrathin Ni films of ~ 1 ps and ~ 500 ps, attributed to Stoner excitations and magnon-phonon scattering, respectively [5.13]. Consequently, the spin-lattice relaxation was pushed to longer timescales (from 6 ps in [5.2] to 500 ps in [5.13]). Following this work, the ability of magneto-optical measurements in providing the femtosecond spin dynamics quantitatively was challenged by Koopmans et al. [5.14]. This was based on evidence that the measured magneto-optical rotation and ellipticity have different relaxation times and subsequently arguing that femtosecond spin dynamics is not genuine. Koopmans et al. proposed instead that spin relaxation rather occurs on the timescale of electron-phonon thermalization and the cause behind it is a highly efficient spin-lattice interaction [5.14]. In contrast, magneto-optical studies of UD in ferromagnetic $CoPt_3$ samples have shown that the technique is applicable on the fs timescale [5.15, 5.16]. The first theoretical investigation of UD was reported by Zhang and Hubner [5.17] who showed that UD is a cooperative effect of the external laser field and the internal spin-orbit coupling, thus suggesting the important role of photons as the driving force behind the experimental observations. However, experimental results obtained by time-resolved photoemission spectroscopy on Ni did not support Zhang and Hubner's proposal [5.18]. It was inferred instead that the energy transfer between electronic and spin excitations is mediated by spin-orbit coupling to induce the observed dynamics on ~300 fs and ~3 ps timescales. These are related to spin excitations such as Stoner pairs and magnons, respectively.

An attempt to probe a fs spin reorientation processes was reported in [5.19], where the magnetization vector-resolved probe of the spin dynamics is used to argue in favor of an ultrafast modification of the magnetic anisotropy in Co samples. A theoretical attempt to unify the prior experimental observations was given by Koopmans et al. [5.20], who advocated an Elliott-Yafet-type spin-flip mediated electron scattering mechanism in the presence of phonons to explain the UD. An experimental attempt to unify the microscopic and macroscopic view of femtomagnetism via studies in Co was

undertaken by Cinchetti [5.21], which supported the Elliott-Yafet-type scattering process introduced previously by Koopmans [5.20]. On the other hand, other studies provide quantitative evidence for the opposite, e.g., Refs. 5.22 and 5.23. A careful consideration of the above-mentioned competing mechanisms for interpreting the ultrafast demagnetization experiments is beyond the scope of this thesis. What is clear after the discussion given here is that despite the efforts to "unify" some common aspects [5.20 and 5.21], there is still a sharp disagreement between different research groups in most recent publications [5.24 and 5.25]. Thus, it becomes evident that measuring the ultrafast demagnetization alone and associate fittings of the experimental curves, is not the way to solve the "puzzle". Moreover, the presently available experimental results appear to be incomplete, which fact can only generate further speculation.

A possible way out of this dilemma would be to carefully choose a combination of several complementary techniques to provide a more complete picture of the real processes that are involved in experimental observations. Such studies have started to appear recently via time-resolved X-ray magnetic circular dichroism [5.26 and 5.27]. Our work is also designed to shed light on this question.

For the case of Fe, the effect of UD is on the order of a few percent at the highest laser fluences which were used to perform the experiments shown in this thesis. On the other hand, much larger signals than the UD signal could be detected that are related to ps coherent spin dynamics following the UD. It is seen that by neglecting the demagnetization signal in modeling the ps coherent spin dynamics, one can explain the experimental results very well thus providing indirect evidence that the neglect of incoherent UD effect in the case of Fe is justified. This can be qualitatively understood by taking into account that the maximum temperature of the Fe samples following laser excitation does not exceed half of the Curie temperature of Fe (T_c = 1040 K). Near the Curie point, where the demagnetization effects are becoming very important and nonlinear with the temperature change, their contribution to UD is more significant for the case of the most studied case (Ni) due to its lower Curie point (T_c = 630 K).

5.2 Coherent Precessional Magnetization Switching Triggered by Femtosecond Optical Pulses

This Section presents experimental results regarding the optical manipulation of coherent spin dynamics in ferromagnetic transition metals. Upon using a specially designed epitaxial sample that features uniaxial magnetic anisotropy, it is demonstrated that laser excitation can be used to control the coherent spin dynamics at large amplitudes. The experimental data and simulations demonstrate a reversible first-order spin reorientation transition (SRT), which is obtained with the use of laser-induced modification of the magnetocrystalline anisotropy.

The occurrence of SRT in ultrathin film ferromagnetic structures is already well established, providing an effective means of magnetization direction control at the nanoscale. Numerous studies during the last few decades [for recent reviews, see Refs. [5.28 and 5.29], and more recent ones [5.30 and 5.31] have evidenced that SRTs are dependent on variables such as the layer thickness, the temperature, and the stress state induced into the film by its interaction with the substrate. Such studies typically look at the quasi-static equilibrium states of the SRT, whereas its dynamical pathways have been elusive. Presently, it is of high interest to pursue studies of SRTs on the ultrafast timescale and learn about their dynamics. One important reason is the rapid development of spin electronics, which is only possible by establishing energy-efficient magnetic writing techniques [5.32]. Experimental access to the ultrafast SRT mechanism will lead to a deeper understanding of the physics of spin reorientation, which can be further exploited in ultrafast magnetic switching applications, thus bearing on issues of both fundamental and practical importance.

Femtosecond optical pump-probe techniques are a possible way to induce SRTs and study their dynamics. This approach was already successful for studying the non-equilibrium phase transformations of structural and magnetic origin in metals and semiconductors on sub-ps timescales [5.33]. In the case of transition metal ferromagnets, the electron-phonon equilibrium is restored quickly (~ 1 ps), recently evidenced in direct measurements of lattice temperature rise in Ni [5.34]. Additionally, by using a time-resolved magneto-optical Kerr effect (TR-MOKE) probe, laser-induced coherent magnetization oscillations could be detected in the ferromagnetic transition metals (Ni,

Fe, and Co), stimulated by thermally induced change of the magnetic anisotropy energy (MAE) [5.19, 5.35-5.37]. This effect opens the way for time-resolved optical studies of SRT and is exploited here.

At the present, the investigation of ultrafast SRT dynamics is marked by several significant challenges. Firstly, it is important to establish if ultrafast laser-induced SRT can compete with the use of pulsed magnetic fields [5.38-5.40], or spin polarized electrical currents [5.41] in magnetic precessional switching (MPS) applications. Secondly, determining the timescales for excitation and decoherence is essential for elucidating the phase-coherent mechanism of SRT and separating it from incoherent effects such as ultrafast demagnetization [5.2]. Furthermore, the nature of the slow relaxation mechanism of the SRT needs to be clarified [5.42].

A suitable configuration for TR-MOKE studies of SRT is an epitaxial (110) Fe film with in-plane magnetization. Such samples are characterized by a well defined lattice orientation favoring magnetoelastic coupling (see Section 2.3) with laser-induced thermo-elastic expansion. This permits us to explore the role of intrinsic sources of MAE, i.e., magnetocrystalline anisotropy and magnetoelastic coupling, by inducing the SRT. Therefore, the time-dependent thermal modification of MAE may induce a change in effective magnetic field direction that exerts a transient torque on the magnetization. The use of a high quality epitaxial film is very advantageous here, in sharp contrast to the use of polycrystalline layers, where the grain misalignment leads to large dispersion of the internal magnetic fields, which in turn causes a strong out-of-phase spin dynamics. This is due to large directional dispersion of the effective internal field in the presence of grain misalignment.

The basic idea of our experiment is to take advantage effectively of the laser modification of MAE to initiate precessional switching. For the case of the Fe/Ge (110) sample (see Section 4.2), magnetized within the film plane, this is accomplished in the presence of an external magnetic field, H, used for intensifying the laser effect. The magnetic free energy in a (110) oriented single crystal thin film was thoroughly analyzed in the theoretical section 2.3 of this thesis. By combining Eqs. 2.30, 2.33, 2.45 and 2.46, the in-plane angle dependence of magnetic free energy can be expressed as:

$$F^{(110)} = \frac{K_1(T)}{4}\sin^2\phi\left(4-3\sin^2\phi\right)+\left[K_u(T)-\kappa\varepsilon_T\right]\cos^2\phi - HM\cos\left(\phi-\phi_H\right) \qquad (5.1)$$

where ϕ is the in-plane magnetization angle measured from the <001> easy axis, T is the temperature, ϕ_H is the in-plane angle between the applied field $\boldsymbol{H}$ and the <001> direction, K_1 is the cubic magnetocrystalline anisotropy, K_u is a growth-induced uniaxial anisotropy, $\varepsilon_T = \alpha_T\,\Delta T$ is the laser-induced thermal strain, and M_0 is the amplitude of the saturation magnetization vector. κ is a magnetoelastic coefficient for the (110) plane (see section 2.3 for notations):

$$\kappa = \left(B_1 - B_2\right)\frac{1+\mathrm{K}^{(110)}}{2} = \left(B_1 - B_2\right)\frac{C_{11}+2C_{12}}{C_{11}+C_{12}+2C_{44}} \qquad (5.2)$$

$K_1(T)$ and $K_u(T)$ for the Fe film has been determined from the frequency of Kittel's uniform mode of precession using the presently developed formalism (see Section 2.3 and 2.4), together with the variation of these frequencies versus ϕ_H in pump-probe experiments. The procedure and the results are reported in Section 4.2 of this thesis.

The orientation of the effective field, $\vec{H}_{eff}$, which determines the equilibrium magnetization direction, ϕ_H, is obtained by canceling the first order derivatives of $F^{(110)}$, with respect to both polar coordinates ϕ and θ. These conditions reduce to the Eq. 2.56, as the magnetization at equilibrium should be always in plane ($\theta=\pi/2$). When $\boldsymbol{H}$ is applied near the <1 $\bar{1}$ 0> direction ($\phi_H \sim \pi/2$) and has a non-saturating value, inspection of Eq. (2.56) reveals that a laser modification of $F^{(110)}$ can suddenly tip the magnetization equilibrium from <001> onto the <1 $\bar{1}$ 0> axis. The resulting $\vec{H}_{eff}(t)$ can be introduced in the Landau-Lifshitz (LL) Eq. (2.47), as the initial orientation of the magnetization lies close to the <001> direction ($\phi \sim 0$), and a large transient field torque acts on the magnetization inducing a precession movement. We used Runge-Kutta method for solving numerically the LL equation, with the assumption of large precession movements. For simplicity, we have not included in Eq. (2.56) the temperature dependence of the magnetization modulus, $M(T)$, which was observed to contribute only a few percent relative to the spin reorientation effects described here.

For cases when $\Delta M(T)$ reaches higher levels, other alternate approaches to the LL formalism were proposed in [5.19, 5.43-5.45] that include demagnetization effects. Considering the maximum laser-induced temperature rise from our experiments, $\Delta T \approx 100\ ^0$C, and varying the strength of the magnetic field applied near <1 $\bar{1}$ 0> axis, there are two limiting cases for the pump-laser effect on MAE. The first case is illustrated in Figure 5.1(a) where the magnetic energy potential minimum (or the direction of $\vec{H}_{eff}$) is shifted continuously from ϕ=23^0 to ϕ=30^0 upon the temperature raise when H=400 Oe. Increasing H to 500 Oe leads to a different situation (see Figure 5.1.b), where at ΔT=58^0 C, $\vec{H}_{eff}$ suffers a large-angle jump of 55^0.

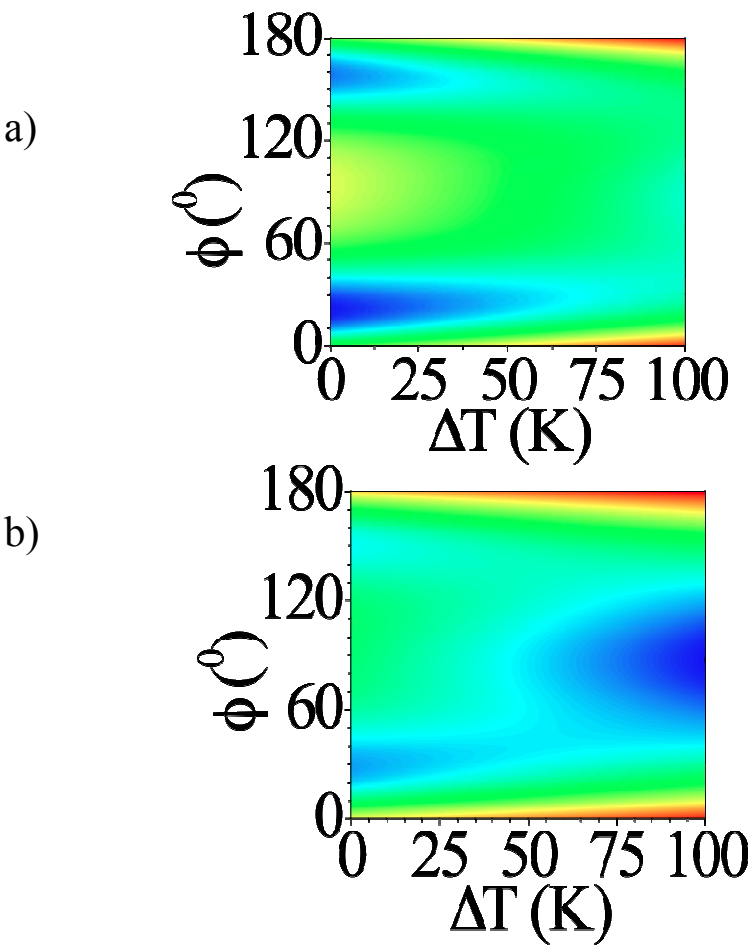

Figure 5.1 Magnetic energy anisotropy as a function of the temperature rise, ΔT, for two different magnetic fields: (a) 300 Oe, and (b) 500 Oe.

In qualitative agreement with these cases, our TR-MOKE measurements of the magnetization components evidence strikingly different behavior for different H values. When the H value is low (400 Oe), and $\vec{H}_{eff}$ is only slightly shifted from initial state of equilibrium, the MOKE signal amplitude is moderate and the magnetization precession is long-lived (Figure 5.2). The magnetization components were separated using the procedure described in Chapter 3.3 and the stable $\pi/2$ phase shift observed between the transversal and polar component proves the separation consistency. However, some degree of mixing between the magnetic signal of the film and the intense acoustic phonon signal from the substrate can be observed below 200 ps. This parasite component was excluded in the following by using a high frequency filter.

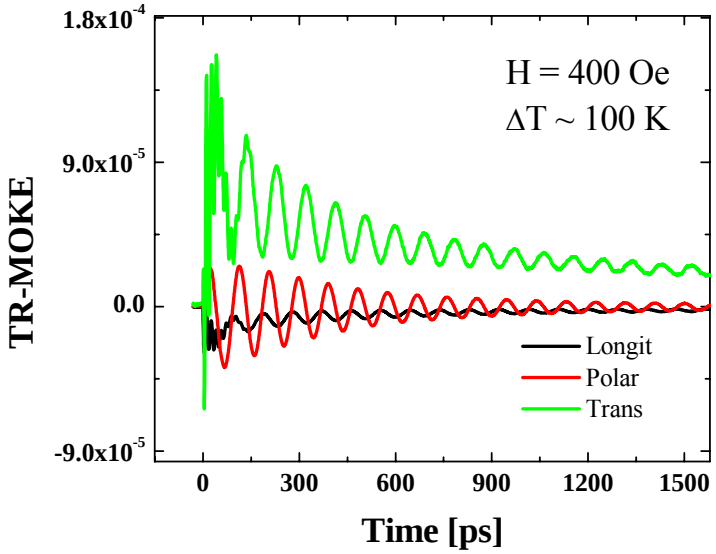

Figure 5.2 Dynamics of the magnetization components below threshold for switching for the transversal (green line) in-plane hard axis, polar (red line) out-of-plane hard axis, and longitudinal (black line) in-plane easy axis.

As opposed to the previous case, when the applied magnetic field reaches 550 Oe and the temperature rise is large enough to cause a discontinuous jump of $\vec{H}_{eff}$, the MOKE signal shows a dramatic increase and unusual time dependence (see Figure 5.3). A few distinctive characteristics are evident in these results: a) the amplitudes of the

transverse (M_t) and longitudinal (M_l) components of the magnetization quickly reach large levels;

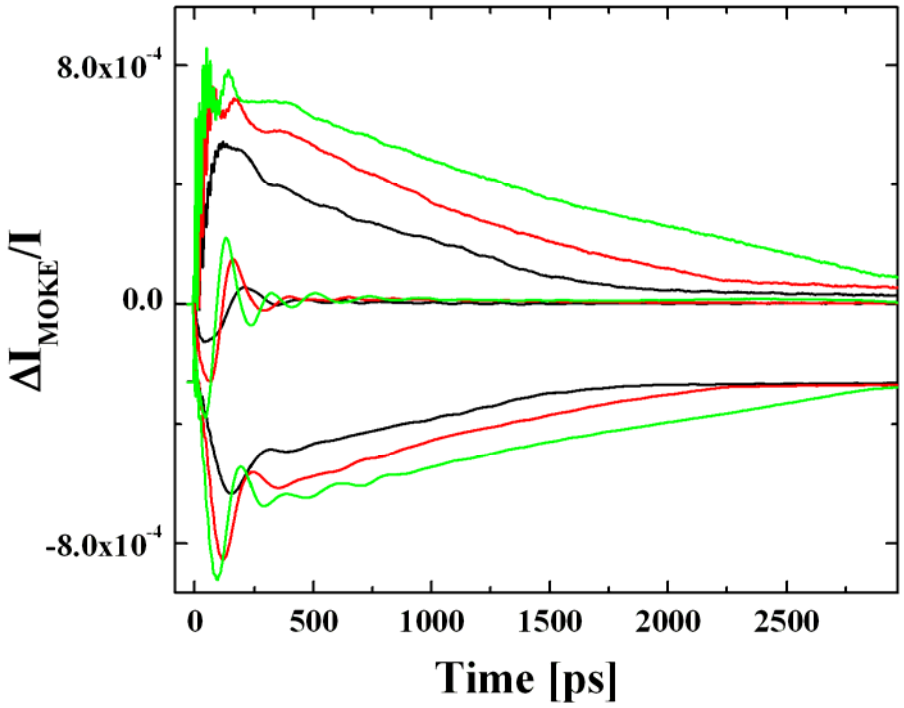

Figure 5.3 Dynamics of the magnetization components in switching regime at H = 550 Oe for three laser power levels, corresponding to temperature rises of 45 K (black line), 77 K (red line), and 100 K (green line). The upper curves refer to the transversal component, the middle to the polar, and the lower curves refer to the longitudinal components.

b) the precession relaxes faster than in the case of small amplitude precession (see Figure 5.2) due to an apparent increase of damping; and c) a quasilinear relaxation of the M_t and M_l components follows, which suddenly changes slope at about 1 ns, seen in the data (see Figure 5.3) as a "relaxation kink" (RK). In order to explain these observations, we propose that a first order SRT has occurred during the experiments presented in Figure 5.3, and the phenomenology of this process can be described as a three-stage process:

(I) Due to the pump laser heating, the lattice temperature rises within ~1 ps and triggers a sudden reorientation of $\vec{H}_{eff}$ close to hard axis direction in a region where the threshold temperature is exceeded. This induces s single-domain precession of the

magnetization across the spatial temperature profile generated by the pump laser, with the domain extending its limits to the region where $\vec{H}_{eff}$ is reoriented.

(II) After the large reorientation of the magnetization, which corresponds to the maximum MOKE amplitude (at ~100 ps), the magnetization continues its precession around the new $\vec{H}_{eff}$ orientation as long as the temperature exceeds the temperature threshold necessary for returning to initial sate. However, due to the enhanced damping, the magnetization soon reaches the equilibrium state in the magnetic domain excited by the pump pulse.

(III) The boundaries of the domain created in temporal region I gradually shrink toward the epicenter of the laser-excited region by following the temperature relaxation. It can be considered that the spatial distribution of temperature around the laser beam center is Gaussian and the time decay is exponential:

$$T(r,t) = T_0 + \Delta T\ e^{-(r/r_0)^2}\ e^{-t/\tau} \tag{5.3}$$

If we consider a threshold temperature T_s, the area of the region with local temperature exceeding T_s will undergo a linear shrinking in time:

$$\pi r_c^2(t) = \pi r_0^2\left(\ln\frac{\Delta T_{\max}}{T_s - T_0} - \frac{t}{\tau}\right) \tag{5.4}$$

As the magnetization orientation inside the excited area is dramatically different than that in the surrounding area, the probe laser will record an average value showing the same linear dependence. This process will end abruptly when the temperature in the center will reach the threshold value:

$$t_{RK} = \tau\ \ln\frac{\Delta T_{\max}}{T_s - T_0} \tag{5.5}$$

It is at this moment when the RK is observed.

In order to provide quantitative support for the just-described switching mechanism, we calculate next the phase diagram of the SRT in Figure 5.4 by using the experimentally determined MAE. It can be seen that the selection of specific values of H and ΔT determines whether switching occurs or not. Moreover, the warming and cooling cycles exhibit thermal hysteresis during the SRT when $\phi_H > 85^0$ (Figure 5.4 inset). Consequently, the first-order character of SRT is clearly revealed, based on the

discontinuous jump of $\vec{H}_{eff}$ as well as the presence of accompanying thermal hysteresis [5.46]. Since in our experiment the temperature is time dependent [5.37] we can use this fact to plot the temporal variation of $\vec{H}_{eff}$ orientation (see Figure 5.5) and, respectively, the instantaneous precession frequency, v, as in Figure 5.6.

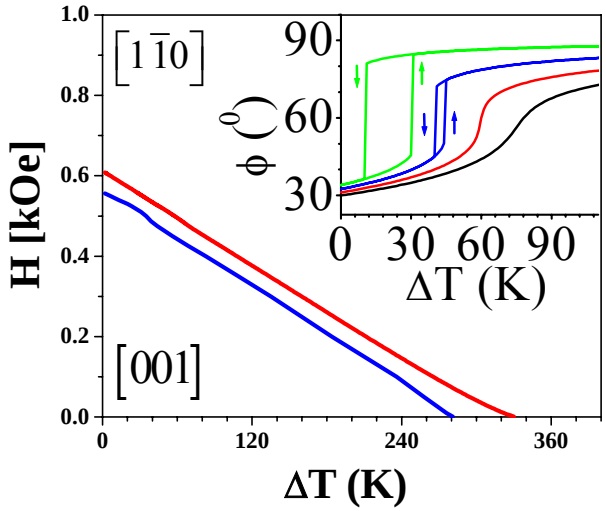

Figure 5.4 Phase diagram for reversible switching (switch above in red line and return below in blue line). The inset shows the effect of inclining applied magnetic field (H = 500 Oe) relative to the hard axis direction: green – 2^0, blue – 4^0, and black – 5^0.

It can be seen in Figure 5.5 that the angular positions of the laser-shifted magnetic potential minima do not vary much with ΔT above the SRT threshold, which already provides some qualitative support for step I of the switching process. On the other hand, v exhibits a large dispersion versus ΔT across the lateral spatial profile of the pump excited region, which we relate to the observation of a fast decay of oscillations shown in Figure 5.3.

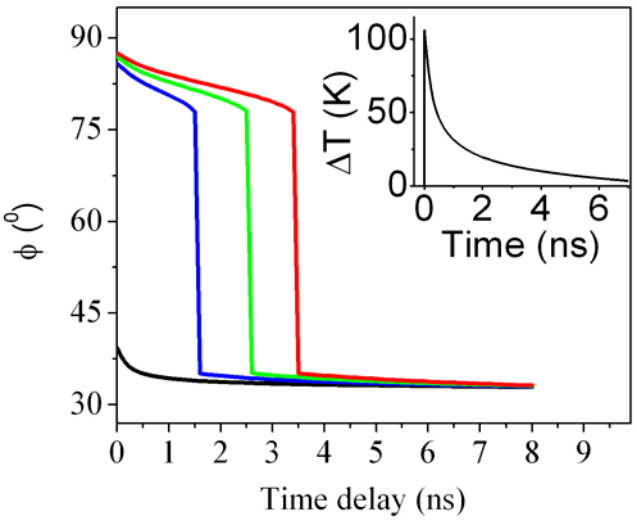

Figure 5.5 Temporal variation of the effective field direction, including the temperature relaxation (inset). The initial transient temperature rise was 25 K (black line), 50 K (blue line), 75 K (gren line), and 100 K (red line).

It is important to note that due to the Gaussian shape of the laser intensity profiles, our measurements probe the dephasing of the different oscillatory components averaged over the spatial convolution of the pump and probe beams, in addition to the normal decay related to α from LL Eq. (2.47). Interestingly, the abrupt jumps seen in Figures 5.5 and 5.6 can be used to compare with the experimental determination of RK.

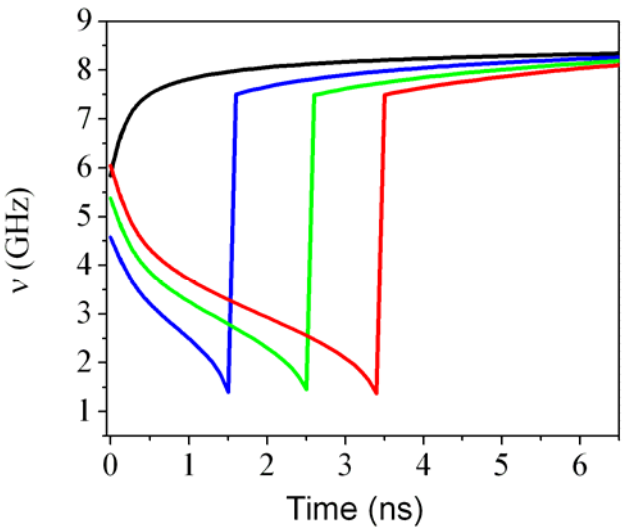

Figure 5.6 Temporal variation of the instantanenous frequency. The initial transient temperature rise was 25 K (black line), 50 K (blue line), 75 K (gren line), and 100 K (red line).

Based on the calculations shown in Figures 5.4-5.6, when ΔT exceeds the temperature threshold of SRT across the excited region, a saturation behavior is expected to occur. This is in agreement with our experimental observations corresponding to M_L and M_T traces for $\Delta T \geq 63\ ^0C$ from Figure 5.3. Furthermore, the speed of precessional switching, and the return to the initial state via RK, can be directly compared with the calculations. Excellent quantitative agreement is shown in Figures 5.7 and 5.8 for both switching speed and the temporal variation of RK as a function of laser excitation intensity. This demonstrates that the underlying assumptions of the proposed phenomenology are correct.

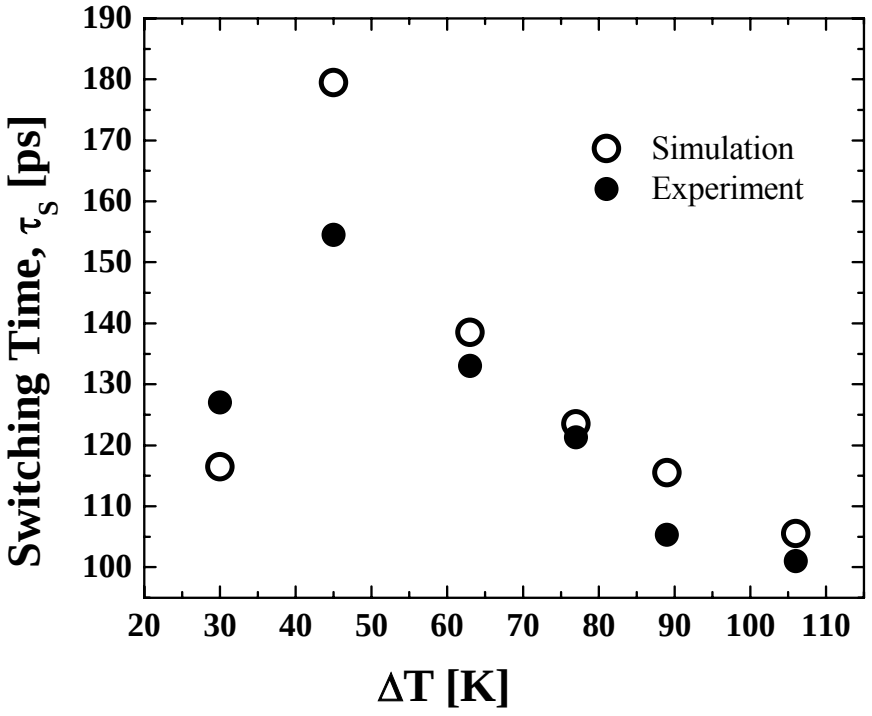

Figure 5.7 Experimental and calculated reorientation time.

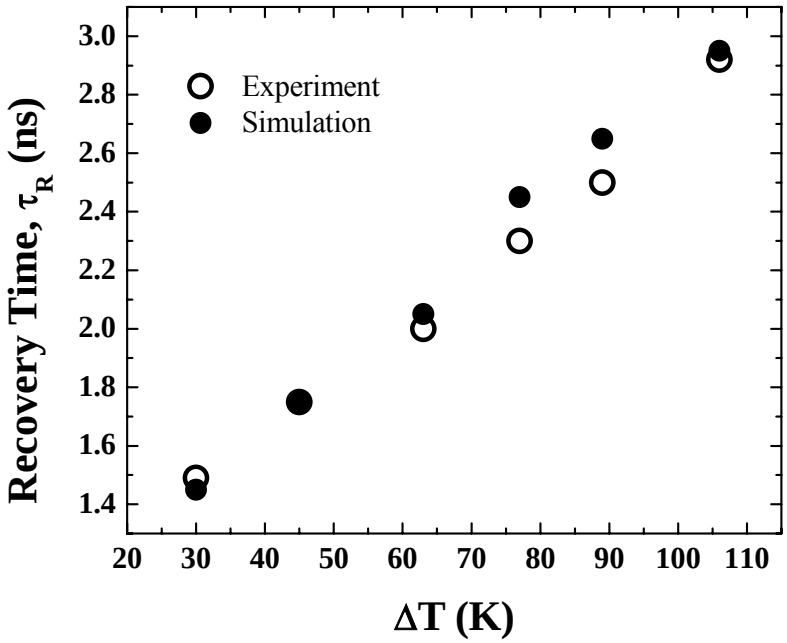

Figure 5.8 Experimental and calculated time of return to original state.

To make a further test of the proposed model, we show the experimentally determined magnetization trajectory in stage I and stage II by plotting the 3 orthogonal projections of this trajectory in Figure 5.9. The experimental results can be compared with calculations using LL Eqn. 2.47, which are shown in Figure 5.10. The details of the experimentally observed precessional SRT compare favorably with the simulated magnetization trajectories that reproduce the main details of the experiment.

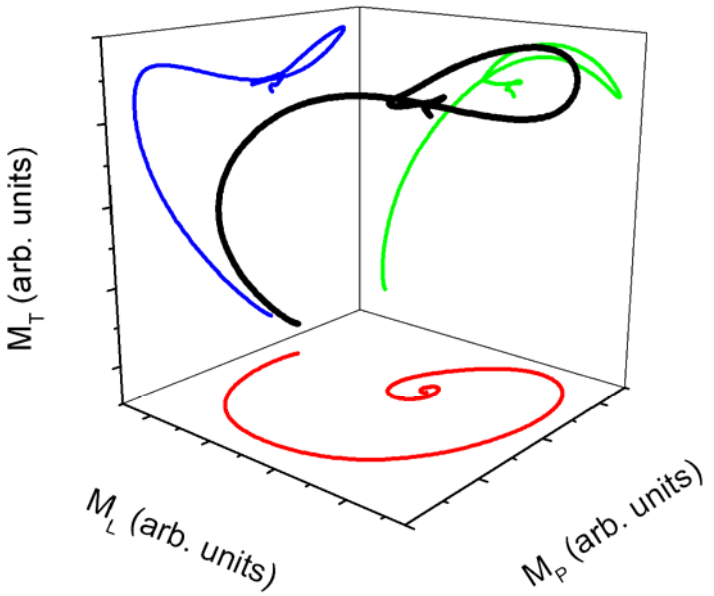

Figure 5.9 Experimental trajectory: switch to metastable state at $\Delta T = 89K$.

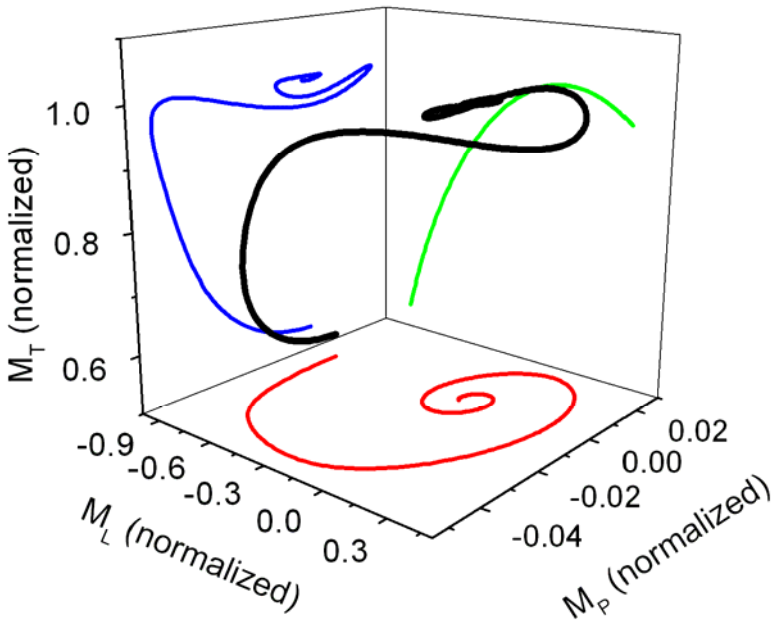

Figure 5.10 Theoretical trajectory: switch to metastable state at $\Delta T = 89K$.

Comparison is made with calculated trajectories only for the first few hundred of ps. During this temporal interval, an abrupt transition to the excited state takes place, followed by precession around the transient $\vec{H}_{eff}$ oriented along <1 $\bar{1}$ 0>. As in the plots of the three components shown in Figures 5.9 and 5.10 is lacking the time coordinate, we provide a time-scale for the measured and simulated results in a separate diagram (Figure 5.11). Once again, we notice a good match between the theoretical calculations and the experimental data during the stages I and II, up to about 300 ps.

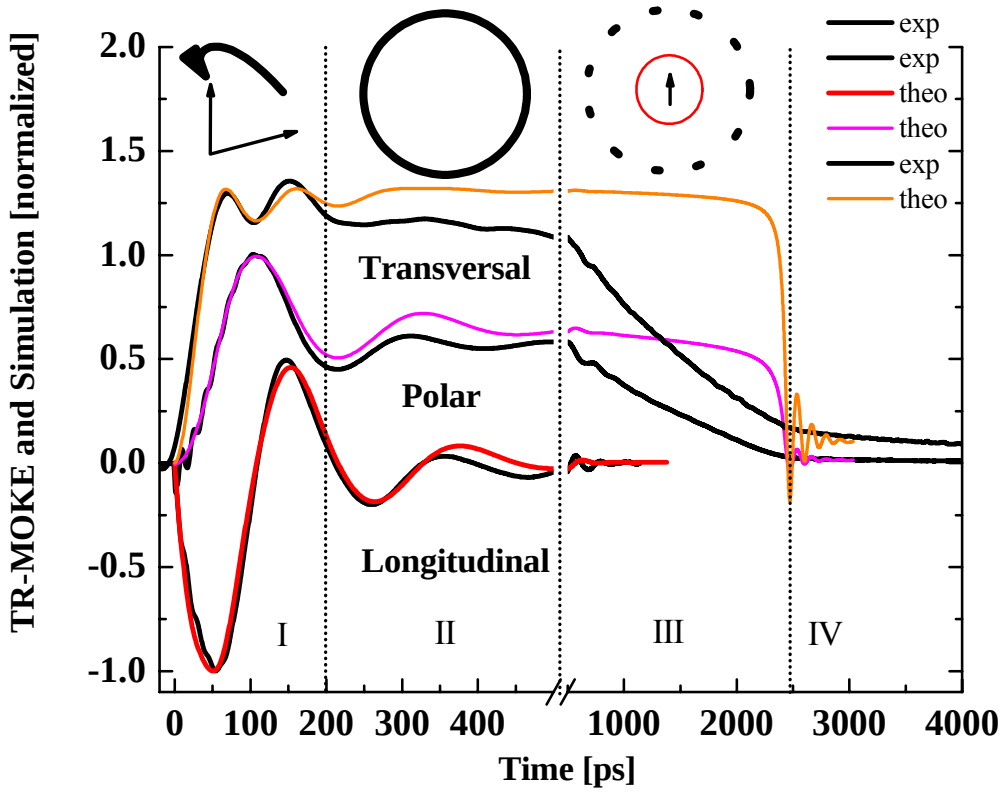

Figure 5.11 The temporal steps of the reversible transition for the sample Au(4nm)/Fe (16.5nm)/Ge (110).

In stage III, which corresponds to the ns scale, the theory predicts a precessional return to the initial state characteristic of macrospin dynamics. This refers to a single magnetic domain in the excited state and cannot be compared directly with experiment. This only provides a magnetization value averaged over the probe area. As was already

suggested in step III, the return to the initial state should take into account the shrinking of the excited area described by Eq. 5.4. However, the agreement between the model (see Eq. 5.5) and the experiment on the return to the initial state was already obtained in calculations of the time and temperature dependency of RK (Figure 5.8). The last stage, denoted as IV in Figure 5.11, represents the magnetization relaxation during the slow cooling from T_s, the threshold temperature, to T_0, the initial/final temperature.

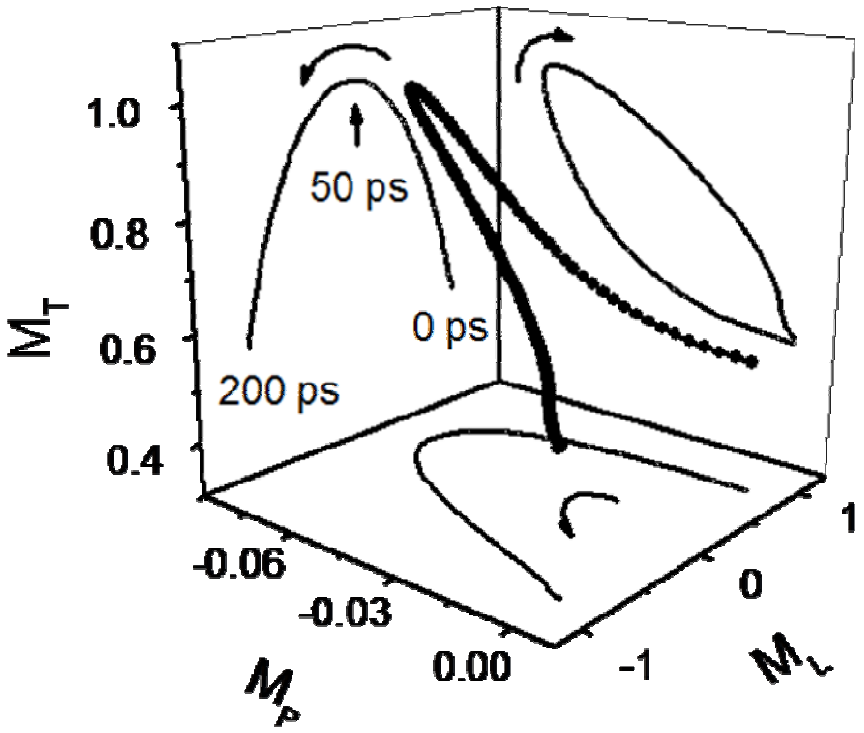

Figure 5.12 Ballistic irreversible switch simulation.

The possibility of irreversible precessional switching was revealed in LL calculations by the adjustment of H, ΔT and the lattice-cooling rate. An example is the so called ″ballistic″ reversal without ringing in the final state [5.39 and 5.40] obtained in the LL simulations (Figure 5.12). The observation of this irreversible process is not yet possible with our pump-probe stroboscopic technique that probes only the reversible phenomena [5.47], and further experimental development of this technique is necessary. Additionally, selecting the material and tailoring the sample shape using the nano-technologies will be very influential for customizing MAE in order to achieve the laser-driven switching, without the application of any external magnetic field.

REFERENCES FOR CHAPTER 5

5.1 M. I. Kurkin, N. B. Bakulina, and R. V. Pisarev, Phys. Rev. B 78, 134430 (2008).

5.2 E. Beaurepaire et al., Phys. Rev. Lett. 76, 4250 (1996).

5.3 E. Abrahams and C. Kittel, Phys. Rev. 88, 1200 (1952).

5.4 A. Vaterlaus et al., J. Appl. Phys. 67, 5661 (1990).

5.5 A. Vaterlaus, T. Beutler, and F. Meier, Phys. Rev. Lett. 67, 3314 (1991)

5.6 A. Vaterlaus et al., Phys. Rev. B 46, 5280 (1992).

5.7 J. Xiao et al., Theory of magnon-driven spin Seebeck effect, PRB 81, 214418, (2010).

5.8 K. Uchida, S. Takahashi, K. Harii, J. Ieda, W. Koshibae, K. Ando, S. Maekawa, and E. Saitoh, Nature (London) 455, 778 (2008).

5.9 C. D. Stanciu, F. Hansteen, A. V. Kimel, A. Kirilyuk, A. Tsukamoto, A. Itoh, and Th. Rasing, Phys. Rev. Lett. 99, 047601 (2007).

5.10 M. I. Kurkin, N. B. Bakulina, and R. V. Pisarev, Phys. Rev. B 78, 134430 (2008).

5.11 K. Vahaplar, A. M. Kalashnikova, A. V. Kimel, D. Hinzke, U. Nowak, R. Chantrell, A. Tsukamoto, A. Itoh, A. Kirilyuk, and Th. Rasing, Phys. Rev. Lett. 103, 117201 (2009).

5.12 J. Hohlfeld, E. Matthias, R. Knorren, and K. H. Bennemann, Phys. Rev. Lett. 78, 4861 (1997).

5.13 A. Scholl, L. Baumgarten, R. Jacquemin, and W. Eberhardt, Phys. Rev. Lett. 79, 5146 (1997).

5.14 B. Koopmans, M. van Kampen, J. T. Kohlhepp, and W. J. M. de Jonge, Phys. Rev. Lett. 85, 844 (2000)].

5.15 L.Guidoni et al., Phys. Rev. Lett. 89, 017401 (2002);

5.16 J.Y.Bigot et al, Phys. Rev. Lett. 93, 077401 (2004)

5.17 G. P. Zhang and W. Hübner, Phys. Rev. Lett. 85, 3025 (2000).

5.18 H.-S. Rhie, H. A. Dürr, and W. Eberhardt, Phys. Rev. Lett. 90, 247201 (2003).

5.19 M. Vomir, L. H. F. Andrade, L. Guidoni, E. Beaurepaire, and J.-Y. Bigot, Phys. Rev. Lett. 94, 237601 (2005).

5.20 B. Koopmans, J. J. M. Ruigrok, F. Dalla Longa, and W. J. M. de Jonge, Phys. Rev. Lett. 95, 267207 (2005).

5.21 M. Cinchetti, M. Sánchez Albaneda, D. Hoffmann, T. Roth, J.-P. Wüstenberg, M. Krausss, O. Andreyev, H. C. Schneider, M. Bauer, and M. Aeschlimann, Phys. Rev. Lett. 97, 177201 (2006).

5.22 J. Walowski, G. Müller, M. Djordjevic, M. Münzenberg, M. Kläui, C. A. F. Vaz, and J. A. C. Bland, Phys. Rev. Lett. 101, 237401 (2008).

5.23 I. Radu, G. Woltersdorf, M. Kiessling, A. Melnikov, U. Bovensiepen, J.-U. Thiele, and C. H. Back, Phys. Rev. Lett. 102, 117201 (2009).

5.24 B. Koopmans, G. Malinowski, F. Dalla Longa, D. Steiauf, M. Fähnle, T. Roth, M. Cinchetti, and M. Aeschlimann, Nature Mater. 9, 259 (2010)

5.25 J.-Y. Bigot, M. Vomir, and E. Beaurepaire, Nat. Phys. 5, 515 (2009).

5.26 C. Stamm C, N. Pontius, T. Kachel, M. Wietstruk, H. A. Durr, Phys. Rev. B 81, 104425 (2010).

5.27 C. Boeglin et al., Nature 465, 458, (2010).

5.28 P. J. Jensen and K. H. Bennemann, Surf. Sci. Rep. 61, 129 (2006).

5.29 C. A. Vaz, J. A. Bland, and G. Lauhoff, Rep. Prog. Phys. 71, 056501 (2008).

5.30 F. Matsui et al., Phys. Rev. Lett. 100, 207201 (2008)

5.31 R. Frömter et al., Phys. Rev. Lett. 100, 207202 (2008].

5.32 C. Chappert, A. Fert, and F. N. Van Dau, Nature Mater. 6, 813 (2007).

5.33 K. H. Bennemann, Ann. Phys. (Berlin) 18, 480 (2009).

5.34 X. Wang et al., Appl. Phys. Lett. 92, 121918 (2008).

5.35 M. van Kampen et al., Phys. Rev. Lett. 88, 227201 (2002).

5.36 H. B. Zhao et al., Appl. Phys. Lett. 86, 152512 (2005).

5.37 V. A. Stoica et al., CLEO/QELS Conference Proceedings, 1-9, 3333 (2008).

5.38 C. H. Back et al., Phys. Rev. Lett. 81, 3251 (1998).

5.39 T. Gerrits et al., Nature (London) 418, 509 (2002).

5.40 H. W. Schumacher et al., Phys. Rev. Lett. 90, 017204 (2003).

5.41 D. C. Ralph and M. D. Stiles, J. Magn. Magn. Mater. 320, 1190 (2008).

5.42 T. Eimüller et al., Appl. Phys. Lett. 91, 042508 (2007).

5.43 D. A. Garanin, Phys. Rev. B 55, 3050 (1997).

5.44 U. Atxitia et al., Appl. Phys. Lett. 91, 232507 (2007).

5.45 N. Kazantseva et al., Phys. Rev. B 77, 184428 (2008).

5.46 C. S. Arnold, D. P. Pappas, and A. P. Popov, Phys. Rev. Lett. 83, 3305 (1999).

5.47 V. A. Stoica et al., Opt. Express 16, 2322 (2008).

CHAPTER 6

CONCLUSIONS

Perhaps the most important accomplishment of this dissertation is the use of ultrafast optical techniques for the coherent excitation and dynamic manipulation of the magnetization of epitaxial thin films. These experiments revealed many interesting and previously unobserved details which have shed light on the mechanism of optical excitation of spin waves and the influence of magnetic anisotropy on the dynamic behavior. In order to carry out the work of this dissertation, we devised a novel apparatus to attain in practice two major goals motivating our research efforts: optical pulse magnetometry and optical control of the magnetization switching. Along this path, new aspects were learned in the study of coherent magnetization dynamics evolving in the presence of electronic and lattice excitations driven by femtosecond optical pulses. We were able to interpret some of the phenomena in terms of phenomenological models for the energetics of magnetization; some other observations are still not understood and need further exploration.

The instrumental development part of the work combined the use of femtosecond fiber-lasers and asynchronous optical sampling (ASOPS), to provide a superior alternative to traditional pump-probe techniques, for studies of long-lived excitations in opaque materials. This technique is demonstrated through measurements of heat transport, coherent optical and acoustic phonons, and coherent magnetization dynamics. To quantify the experimental observations, we wrote down a phenomenological theoretical formalism that improved our accounting of different types of excitations in ferromagnetic metallic films. This approach allowed us to study the correlations between the dynamics of different degrees of freedom in the ferromagnetic metals: electronic, spin and the lattice.

We first analyzed the data obtained on the heat transport across the film-substrate boundary. Then, we have detected coherent phonon oscillations, and found that oscillation frequencies of the optical and acoustic phonons match nicely the well known literature values. For the case of magnetization dynamics we reproduced results which are similar to those from the well developed ferromagnetic resonance (FMR) technique, we demonstrated that our new approach is able to go far beyond what FMRis capable. In particular, our technique can *manipulate* the magnetization *coherently*, and measure the resulting dynamics and relaxation *directly*, with *spatial resolution* limited only by the laser wavelength (780 nm for our probe beam). Moreover, the data acquisition of time-resolved spectra is performed at very fast rates (~ 1 ms for a single temporal scan). Next, we are able to probe the propagation of the thermal electronic and lattice excitations across thin and thick films of Fe.

From these measurements, we estimate that non-equilibrium electronic excitation does not travel much further than the pump optical penetration and is quickly thermalized with the lattice on a length scale of ~22.3 nm and on a timescale of ~ 0.8 ps. On the longer ps to ns timescales we distinguish the propagation of coherent phonons and heat flow through the Fe films. Thinner Fe films (< 300 nm) appear to exhibit slightly reduced thermal diffusivities (~ 0.176 cm^2/s) than the known bulk value (0.226 cm^2/s).

In a complementary approach to the all-optical ASOPS experiments, we have performed time-resolved X-ray scattering studies of lattice excitations and their coupling with magnetic excitations in epitaxial Fe films at the Advanced Photon Source. These studies combined femtosecond optical excitation with time-resolved X-ray diffraction (TR-XRD) probing heat transport in epitaxial Fe films deposited on Ge and MgO substrates with ~ 150 ps temporal resolution. From the TR-XRD measurements, which monitored the uniaxial thermo-elastic relaxation in Fe films on a timescale of ~ 100 ns, we distinguished local variations of the thermal boundary resistance between Fe and MgO and thermal diffusivity of the MgO substrates. Regardless of this difficulty, which needs to be addressed in further studies, our preliminary studies open new possibilities for future investigations of the spin-lattice interactions in ferromagnetic metals via the use of TR-XRD techniques. In particular, synchrotron X-ray facilities demonstrates great potential for exploring the relation between spin and lattice excitations (such as the

magneto-elastic coupling) on hundreds of ps timescale, while, on the other hand, the early stages of femtosecond excitation need to be inferred indirectly. These time resolution limitations are presently surpassed at the Linac Coherent Light Source, which provides the needed X-ray pulse brightness and femtosecond duration for elucidating the details of spin-lattice interaction on ultrafast timescale in ferromagnetic metals, and will be the key for future developments in this field of research.

Additional demonstrations of the ASOPS-based techniques in the study and control of coherent spin waves are given in Chapters 4 and 5. In one experiment aiming to elucidate the nature of optical interactions with the coherent spin waves in epitaxial Fe films, we could make a clear separation of the thermal character in the spin wave generation mechanism. This result is obtained via spatial separation of the region where coherent spin dynamics is operative, from the optical penetration depth of the laser performing the excitation. The experimental observations rule out the coherent coupling of optical excitation with the dynamics of coherent spin waves in epitaxial Fe films. Next, we determined the dependence of the thermal modification of the magnetic anisotropy by the optical excitation in epitaxial (110) Fe films; this is the orientation that is favorable for magnetoelastic coupling.

The phenomenological theory formalism, based on the Landau-Lifshitz equations and variants, provided a reliable tool for quantitative investigation in these experiments. By using thicker Fe films deposited on MgO (100) substrates, due to inhomogenous laser heating, the coherent spin wave excitation occurs nonuniformly and allows us to detect a large number of standing spin wave modes. In consequence, we could determine the exchange stiffness accurately (27.5 eV nm^{-2} in excellent agreement with literature values) from the dynamics of these coherent standing spin waves (CSSW). These studies enabled further determination of the laser excitation dependence of the exchange stiffness parameter, which was found to soften by about 7 % upon laser heating of a 36 nm Fe film by about 80 K. At the same time, we did not find a clear laser modification of the magnetic anisotropy as opposed to what was observed in our studies of thinner samples. These findings provide qualitative evidence that the film thickness and orientation are crucial for the observation of laser modification of magnetic anisotropy. Additionally, the temperature dependence of the exchange constant softening is in agreement with

literature data, evidencing that magnon-electron scattering is an important process in our observations.

We demonstrated the direct probing of coherent spin wave propagation, for the first time, across the film thickness. It is shown that time-frequency analysis is a useful technique for quantitative investigation of propagating properties of coherent spin waves (to determine velocities and attenuation). We find consistency with the dispersion relation in the determination of their group velocities for the case of coherent spin waves with wavevector, *k,* larger than 0.02 nm^{-1}. Based on these and similar experiments, we were able to provide the experimental determination of frequency dependency of the coherent spin wave attenuation length, which is not well understood at the present. Two characteristic length scales of attenuation were observed: (a) the attenuation of a non-equilibrium coherent spin wave packet propagating one trip across the film thickness, and (b) the attenuation after the creation of CSSW upon reflection at the film-substrate boundary. The attenuation measured for the case (b) of ~ 1 μm and smaller, depending on the *k* values, does not depend visibly on the film thickness, and is smaller than the one from the case (a) by a factor of 2.

We could estimate the effective value of Gilbert damping parameters corresponding to spin wave attenuation lengths from (a) and (b), as $\alpha = 0.011$ and $\alpha = 0.005$ (compared with the accepted bulk value of $\alpha \sim 0.002$), respectively. We point out, however, that this estimation does not account for the conductive losses during the spin wave propagation, and needs further development to account for this discrepancy. This opens new possibilities for studies of coherent spin wave propagation correlation with the conduction mechanisms in ferromagnetic metals. In a second intriguing observation, we find than the coherent spin waves with $k \sim 0$, excited near the surface of Fe can propagate very deeply and very quickly (significantly faster than sound) through micron size films. This result is unexpected in the light of their vanishing propagation speed and must include an electronic transport mechanism to explain the observations. The origin of such experimental observations will need to be clarified in the future work.

We also presented our experimental results regarding the optical manipulation of coherent spin dynamics. Using an Fe(110) epitaxial sample that exhibits uniaxial magnetic anisotropy, it is demonstrated that laser excitation can be used to induce spin

dynamics at large amplitudes. Our experimental data evidence a reversible first-order spin reorientation transition (SRT) that is triggered via a laser-induced change of magneto-crystalline anisotropy. As a result, for special conditions of laser irradiation and external magnetic field, the film undergoes a single domain magnetic precessional switching (MPS) to a metastable state in about 200 ps. The magnetic relaxation from the metastable to the base state involves a dual domain mechanism and happens on ns timescale. We provide a model to explain the experimental data and predict further applications of this technique. The details of the experimentally observed MPS compare favorably with the simulated magnetization trajectories that reproduce the main details of the experiment. We have also discussed the optical control of irreversible MPS, which cannot be observed with our experimental arrangement. Along these lines, further studies are necessary to achieve the conditions for switching between two stable states.

The current work suggests a variety of additional experiments and corresponding theoretical work for the interpretation of the results. In particular, the coherent control of magnetic dynamics with pulsed lasers will undoubtedly be a major direction for this field in the future.